



DISSERTATION

Effects of light on mixed conducting electrodes in high-temperature solid oxide electrochemical cells

ausgeführt zum Zwecke der Erlangung des akademischen Grades eines Doktors der
Naturwissenschaften unter der Leitung von

Univ.Prof. Dipl.-Phys. Dr.rer.nat. Jürgen Fleig

am Institut für Chemische Technologien und Analytik (E1 64/EC)
Fachbereich Elektrochemie
Arbeitsgruppe für Festkörperelektrochemie und Elektrokeramik

eingereicht an der Technischen Universität Wien
Fakultät für Technische Chemie

von

Gregor Walch, MSc
Matrikelnummer 0501147
Ernst-Melchior-Gasse 11/2/7, 1020 Wien

Wien, am 20.04.2016

Gregor Walch

Zu jedem komplexen Problem gibt es eine einfache und leicht verständliche, aber
falsche Lösung.
Harald Lesch [1]

Abstract

The effect of light on electrochemical processes is often investigated in cells using a liquid electrolyte. Work on solid state photoelectrochemical cells, however, is scarce. This study therefore combines the fields of photoelectrochemistry and solid state electrochemistry, focussing on the fundamentally interesting aspects of light-induced defect chemical changes.

From literature the response of the oxygen incorporation kinetics to the irradiation with UV light is known for the "model materials" SrTiO_3 and TiO_2 . These studies suggest that UV light accelerates the oxygen incorporation into the material after a sudden increase in the oxygen partial pressure of the surrounding atmosphere. In the present thesis these two oxides were investigated under constant atmosphere to check the effect of light on (more or less) equilibrated samples. The two materials were used as electrodes in high-temperature solid state photoelectrochemical cells that were exposed to UV radiation while monitoring the voltage change or performing electrochemical impedance spectroscopy (EIS). Parameters such as oxygen partial pressure, temperature, current collector material or geometry were varied.

SrTiO_3 samples had an yttria-stabilized zirconia (YSZ) thin film electrolyte, deposited by PLD (pulsed laser deposition) on the single crystalline SrTiO_3 working electrode. On the TiO_2 samples the working electrode was a titania thin film which was deposited on single crystalline YSZ by sputtering of Ti and subsequent annealing in air. On both types of samples photolithographically microstructured metal current collectors were deposited by sputtering. The electrochemical cells were completed by a porous Pt counter electrode.

Several light effects were observed in voltage-time curves as well as in EIS measurements.

- On SrTiO_3 electrodes time-resolved EIS was performed and showed a decrease in SrTiO_3 bulk resistance of up to two orders of magnitude under UV light. Decrease with light and re-increase of resistance after turning off the light showed different time behaviour.
- On both types of electrodes the same typical voltage-time evolution was observed. It was interpreted as a mixture of at least two voltages: a photovoltaic and a Nernst voltage (battery voltage), caused by oxygen incorporated into the electrode material during illumination.
- On TiO_2 electrodes a kinetic effect was observed in impedance measurements.

The oxygen stoichiometry change could be caused by the acceleration of the oxygen incorporation reaction at the electrode surface, which is in agreement with literature. The altered defect chemical state is then reflected in a changed photovoltaic voltage (different "dopant concentration"), the battery voltage as well as the enhanced conductivity.

Kurzfassung

Die Auswirkung von Licht auf elektrochemische Prozesse wird oft in Zellen mit flüssigem Elektrolyt untersucht. Arbeiten an photoelektrochemischen Zellen, die ausschließlich aus Festkörpern bestehen, sind allerdings rar. Diese Untersuchung kombiniert daher die Gebiete der Photoelektrochemie und der Festkörperchemie, wobei der Schwerpunkt auf grundlegend interessanten Aspekten der Licht-induzierten defektchemischen Änderungen liegt.

Aus der Literatur ist der Effekt von UV-Licht auf die Sauerstoff-Einbau-Kinetik der „Modellmaterialien“ SrTiO_3 und TiO_2 bekannt. Diese Studien zeigten, dass UV-Licht den Sauerstoff-Einbau, hervorgerufen durch ein plötzliches Ansteigen des Sauerstoff-Partialdrucks in der umgebenden Atmosphäre, beschleunigt. In der vorliegenden Dissertation wurden diese beiden Oxide in konstanter Atmosphäre untersucht um den Effekt von Licht auf (mehr oder weniger) äquilibrierte Proben zu erkennen. Die beiden Materialien wurden als Elektroden in photoelektrochemischen Hochtemperatur-Festkörper-Zellen verwendet, die UV-Licht ausgesetzt waren, während Spannungsmessungen und elektrochemische Impedanzmessungen (EIS) durchgeführt wurden. Parameter wie Sauerstoffpartialdruck, Temperatur, Stromsammler-Material oder Geometrie wurden variiert.

Die SrTiO_3 -Proben hatten einen Dünnschicht-Elektrolyt aus yttrium-stabilisiertem Zirkoniumdioxid, der mittels gepulster Laser-Deposition (PLD) auf der einkristallinen SrTiO_3 -Arbeitselektrode abgeschieden wurde. Die Arbeitselektrode der TiO_2 -Proben war eine Titandioxid-Dünnschicht die auf einkristallinem yttrium-stabilisiertem Zirkoniumdioxid durch Sputtern von Ti mit anschließendem Tempern in Luft aufgebracht wurde. Auf beiden Typen von Proben wurden photolithographisch mikrostrukturierte Stromsammler aus Metall mittels Sputtern abgeschieden. Die elektrochemischen Zellen wurden durch eine poröse Pt-Gegenelektrode vervollständigt.

Mehrere Licht-Effekte wurden sowohl in den Spannungs-Zeit-Kurven als auch in den EIS-Messungen beobachtet.

- Auf beiden Arten von Proben wurde das gleiche typische Spannungs-Zeit-Verhalten beobachtet. Es wurde als Überlagerung von mindestens zwei Spannungen interpretiert: Einer photovoltaischen und einer Nernst-Spannung (Batterie-Spannung), die durch Sauerstoff-Einbau in das Elektrodenmaterial während der Beleuchtung bewirkt wird.
- An SrTiO_3 -Elektroden wurde zeitaufgelöste EIS durchgeführt und zeigte ein Absinken des Bulk-Widerstands von SrTiO_3 um bis zu zwei Größenordnungen unter UV-Licht. Das Absinken mit Licht und das erneute Ansteigen des Widerstands nach dem Abschalten des Lichts zeigten ein anderes zeitliches Verhalten.
- An TiO_2 -Elektroden wurde in den Impedanzmessungen ein kinetischer Effekt beobachtet.

Die Änderung der Sauerstoff-Stöchiometrie könnte durch die Beschleunigung der Sauerstoff-Einbau-Reaktion auf der Elektrodenoberfläche bedingt sein, was in Übereinstimmung mit der Literatur ist. Der geänderte defektchemische Zustand zeigt sich dann in einer geänderten photovoltaischen Spannung (andere „Dotierkonzentration“), der Batteriespannung und verbesserter Leitfähigkeit.

Contents

Preface	1
1 Introduction	3
1.1 Status of research	3
1.1.1 Light-harvesting cells	3
1.1.2 Photocatalytic cells	5
1.1.3 Solid state electrochemistry	5
1.1.4 TiO_2	6
1.1.5 SrTiO_3	11
1.1.6 Solid state photoelectrochemical studies	11
1.2 Aims of this work	11
2 Experimental aspects	13
2.1 Sample preparation	13
2.1.1 SrTiO_3 samples	13
2.1.2 TiO_2 samples	16
2.2 Measurement setup	41
3 Results and Discussion	43
3.1 Is there a light effect on titania?	43
3.1.1 Voltage vs. time measurements on titania compared to other materials	43
3.1.2 Absorption of light in titania thin films	48
3.1.3 Probing a single interface	53
3.1.4 The “typical” effect	55
3.2 Is there a light effect on strontium titanate?	59
3.3 Systematic voltage measurements	60
3.3.1 Titanium dioxide	60
3.3.2 Strontium titanate	69
3.3.3 Comparison of STO samples (s.c. WE) with TiO_2 samples	75
3.4 Systematic impedance measurements	75
3.4.1 Titanium dioxide	75
3.4.2 Strontium titanate	88
3.5 Summarized interpretation	97
3.5.1 Summary of voltage and impedance measurements	97
3.5.2 Interpretation	98
4 Conclusions	112
Acknowledgements	113

Preface

This is my PhD thesis. According to the curriculum at Vienna University of Technology a thesis proves the student's ability to conduct independent scientific research, to use scientific methods and to solve scientific problems [2]. In order to write a thesis it is therefore necessary to know what science and its methods are. However, there is no straightforward, general answer to this question. It is debated since several decades by philosophers of science (cf. e.g. the title and page xix of [3]). How can, on this uncertain basis, a scientific work be carried out?

Even if there is no general answer it seems that there is currently a good agreement between scientists in chemistry about what chemistry, its methods and its main important theories are. Otherwise there wouldn't be rather uniform teaching in chemistry (textbooks, lectures, ...). In this case a scientific work can be carried out within this framework of ideas.

Certainly, not all the scientists agree on the question whether a certain work is scientific or not. Therefore every author has to bear the risk that his work will be rejected by the scientific community.

Consequently, this thesis was carried out with the aim of using methods which are currently considered scientific, even if this pool of methods is not defined generally but subject to social aspects and to change over time.

In many cases scientific activity has to be justified to funding bodies, politicians and other people in general. A very clear statement about the purpose of science was given by Wilhelm Ostwald in his book on electrochemistry published in 1869:

„Als letzter Zweck der Wissenschaft wird meist die Erforschung der Wahrheit bezeichnet.“ [4, p. 4]

It can roughly be translated as "The final purpose of science is usually termed to be the exploration of truth". For him, truth is a well-observed fact and the purpose of science is to describe these observations as completely and simply as possible. Several arguments in favour of striving for such a kind of truth can be found:

- It's simply interesting (without any other purpose). With culture being "the act of developing the intellectual and moral faculties" [5] science can be regarded as a cultural asset because even if the strive for truth does not yield any (usable) result, it still is considered an "expression of higher development of humankind" (definition of culture by [6]).

The same argument is applied e.g. to efforts for preserving buildings defined as cultural heritage or the the funding of arts.

- There might be future applications that push technological advance. Standard examples for the unexpected development of useful technologies are the development of the laser and the application of electromagnetic waves in communication technology [7, 8].

- Application in the near future is possible. A particularly enthusiastic view on the importance of “electrochemistry for a better world” can be found in John Bockris’ 1981 contribution to the *Comprehensive Treatise of Electrochemistry* [9], where he predicted a huge impact of electrochemical technology on many aspects of human life in the 21st century.

For this work, the most important argument can be assigned to the first two categories and is developed in the following chapter.

1 Introduction

Photoelectrochemistry in liquid electrolytes is a well-established field of research, and so is solid state electrochemistry. However, few photoelectrochemical studies on high temperature solid state materials have been reported (see section 1.1). Therefore, it is interesting to combine these two fields. For the present work the model materials strontium titanate (SrTiO_3 , STO) and titanium dioxide (TiO_2 , titania) were chosen. Using these compounds we can draw from a large number of studies which helps in designing and evaluating experiments.

The following section first illustrates the fields of photoelectrochemistry and solid state electrochemistry and gives an overview over the relevant literature on the two particular materials that were mainly used in this study.

1.1 Status of research

1.1.1 Light-harvesting cells

This subsection tries to classify the different types of ambient temperature photoelectrochemical cells (PECs) and establish a link to photovoltaic (PV) cells and natural photosynthesis. Comments on technologically important properties like efficiency, stability and scalability are omitted because this work approaches the topic of high temperature solid state photoelectrochemistry from a fundamental point of view. A thorough examination of technological issues can be found e. g. in a paper by McKone *et al.* [10].

Table 1.1 assigns light-harvesting cells to three different categories, according to whether they have an electrolyte and produce chemical compounds or electricity. If chemicals are to be produced, an electrolyte is necessary to transport ions from one electrode to the other. Therefore, the fourth category - a cell that produces chemicals and has no electrolyte - is empty. These categories are described in the following.

Table 1.1: An attempt to classify electro(chemical) light-harvesting cells.

	produces substances	produces electricity
Electrolyte	synthesis cells: different types of PECs (e.g. based on Fe_2O_3 , TiO_2 , SrTiO_3), PV cell + electrolyzer, natural photosynthesis in e.g. plants, bacteria or algae	Regenerative PECs , incl. dye-sensitized solar cells (DSSCs)
No electrolyte	-	e.g. Si, thin film, plastic, perovskite solar cells , solid state DSSCs

Synthesis cells

In table 1.1 synthesis cells are located in the top left corner. Babu *et al.* [11] note that two types of photoelectrosynthesis cells exist: Photoelectrolysis cells, for which the Gibbs energy of reaction, $\Delta_r G$, is positive and photocatalytic cells, for which $\Delta_r G$ is negative and light only catalyses the reaction, but does not drive it uphill. The term “photocatalysis”, however, is not exclusively used for reactions where $\Delta_r G < 0$. It can also denote a reaction where $\Delta_r G > 0$, so the reaction is driven uphill by light (see the first section of [12]). This subsection only deals with the first type of cells (even if they are called “photocatalytic”), the second type is mentioned at the end of this subsection. Photoelectrolysis cells are being investigated in a variety of configurations.

Cell configurations McKone *et al.* [10] distinguish between different approaches from a “macroscopic design” perspective and identify two limiting cases: One end of the scale are PV cells connected to an electrolyzer (two separate devices), while the other end are colloids in an aqueous solution, which produce H_2 and O_2 upon illumination, representing the most integrated cell design. A classification focusing on the mechanism of voltage generation is given in [13]: Solar water splitting cells are categorized in photoanode PECs, photocathode PECs, photoanode/photocathode cells (also termed p/n-photoelectrolysis cells because a p-type and an n-type photoelectrode are used), photoanode-PV cells and photocathode-PV cells, which have an additional, built-in PV cell, and finally PV-photoelectrolysis cells (= PV + electrolyzer). In these cells light is absorbed in the semiconductor(s). The charge separation occurs at the semiconductor/electrolyte-interface as well as at the p/n-junction, if present. For the oxidation or reduction of redox-active species in the electrolyte to occur, the relative energetic positions of bands and redox couples are crucial. Since the semiconductor is a key component of such a PEC it is also convenient to classify cells by working electrode material.

Materials An impressive number of studies using TiO_2 , which has been the favoured material [14] since the pioneering study of Fujishima and Honda in 1972 [15], is compiled in the review by Sheppard and Nowotny [16]. An interesting aspect of titania as a photoanode is that its conduction band edge is at a slightly higher potential (vs. the standard hydrogen electrode) than the potential of the H^+ / H_2 redox couple, which is why an electrical or chemical bias (concentration gradient) between the two half-cells has to be applied in order to effect water cleavage [13]. Many other examples for studies on titania can be found throughout the decades (e.g. [17–19]).

Extensive lists of other electrode materials, which include perovskites (e.g. $SrTiO_3$ [17, 20]), modified perovskites, pyrochlores and traditional semiconductors like Si or III-V and II-VI semiconductors are given in the reviews by Babu *et al.* and Walter *et al.* [11, 13]. Bora *et al.* [21] reviewed $\alpha\text{-Fe}_2\text{O}_3$ as a photoelectrode material, which was also used in e.g. [17, 22, 23]. Further materials include e.g. Ti-Nb-Zr-O nanotubes [24].

Finally, several PV-assisted systems, either with a built-in PV cell or with an external one driving the electrolysis can be found [25–28].

Regenerative PECs

“Regenerative” PECs, or PEC solar cells [11] are electrochemical cells which reduce electro-active species at the cathode and re-oxidise them again at the anode, so no net change occurs. The aim is to generate an electric current and drive it through an external load (see top right corner in table 1.1). The most common photoelectrode materials used are III-V and II-VI semiconductors [14].

A special type of regenerative PECs are dye-sensitised solar cells (DSSCs), first presented by O’Reagan and Grätzel in 1991 [29]. The working electrode is made of a mesoporous, nanocrystalline semiconductor on which one atomic layer of dye is chemisorbed. When light strikes the dye electron hole-pairs are generated. If electrons are transferred to the electrolyte faster than holes, the electrode is a photocathode and vice versa [14]. Although titania is “the common choice” [30], other oxides like ZnO [31], SnO₂ [32], BaSnO₃ [33], SrTiO₃ [34], Nb₂O₅ [35] and NiO [36], but also chalcogenides like CdSe [14] have been used.

Solar cells

Since the breakthrough in solar cell research at Bell Labs in 1954 [37] (at least) three generations of solar cells have evolved [38]. In the context of photoelectrochemistry and perovskite materials the appearance of two types of cells, which can be regarded as descendants of DSSCs, is particularly interesting.

As the task of the liquid electrolyte in a DSSC is to conduct holes it can be replaced by another type of hole conductor. If the electrolyte is removed the device is no longer an electrochemical cell - that’s why it is listed with the other photovoltaic cells in the bottom right corner of table 1.1. Several materials have been investigated as hole conductors: CsSnI_{3-x}F_x [39], CuI [40], spiro-OMeTAD and arylamines, reviewed in [41], or CuSCN [42]. P-type DSSCs using NiO were reviewed by Odobel *et al.* [43], hybrids from DSSCs and hybrid polymer/metal oxide solar cells were reviewed by Bouclé & Ackermann [44].

Perovskite solar cells [45] were the outcome of two modifications on a DSSC: First, the sensitizer was replaced by a perovskite (CH₃NH₃PbX₃, X = Br, I [46]), then a solid hole conductor was used instead of the ion conductor (CH₃NH₃PbI_{3-x}Cl_x and spiro-OMeTAD [47]; CH₃NH₃PbI₃ and spiro-OMeTAD [48]).

1.1.2 Photocatalytic cells

Adopting the nomenclature from [11] these devices only use light to accelerate the reaction, so they do not “harvest” light energy. Hydrogen production by oxidation of methanol on Cu-doped titania was investigated by Yoong *et al.* [49] while this strategy was reviewed by Teets *et al.* (“system 2”) [12]. Titania is also widely investigated as a catalyst for photocatalytic waste decomposition [50].

1.1.3 Solid state electrochemistry

A large field of research in solid state electrochemistry is connected with the aim of understanding and improving solid oxide fuel cells, as can be seen from textbooks on the topic [51, 52]. In order to understand electrode kinetics it is necessary to investigate the underlying defect chemical processes. Despite many poorly understood processes

there is a fair amount of standard models and methods [53, 54]. For the present study it is important to have a set of proven tools at hand to tackle new phenomena that occur by adding the influence of light to solid state electrochemical processes.

1.1.4 TiO₂

Titania occurs in three different natural polymorphs: Rutile, anatase and brookite [55, p. 1521], [56, p. 855], [57, p. 139]. Additionally, several high temperature phases are known [56, p. 855]. Rutile is the thermodynamically stable phase [56, p. 855] [57, p. 139].

Natural titania is often mixed with iron oxides and therefore has a dark colour. It can be cleaned up by the chloride process, which consists of turning TiO₂ into TiCl₄ by reaction with carbon and chlorine at high temperatures, distillation of TiCl₄ and oxidation of TiCl₄ back to TiO₂. Alternatively, titania can be produced from ilmenite (FeTiO₃). Due to its application as a white pigment (e.g. in paint [58] or as additive E171 in food [59]) it is produced industrially. It is also used in sunscreens as an absorber of ultra-violet (UV) light [60]. [55, 61]

Apart from these applications there are two streams of research on titanium dioxide [62]: The main stream is concerned with its photocatalytic properties (see above), while another stream of research is dedicated to solid state properties. Defect chemical equilibria of rutile have been investigated at least from the 1960s on - a summary is already given in Kofstad's textbook on binary metal oxides dating from 1972 [57]. More recently, the defect chemical properties of TiO₂ were intensively investigated by J. Nowotny's group [62–77]. In 2006, M. K. Nowotny *et al.* [72] noted “substantial discrepancies” between the available data and emphasized the need to generate well-defined data. Their most recent publication on the defect model of TiO₂ is a review [78], where they re-published defect diagrams calculated from equilibrium constants measured in [64] but also in an earlier study by Kofstad [79]. In figure 1.1 a Brouwer diagram for TiO₂ at 800°C is shown. Apart from the formation of electrons and holes by excitation across the band gap and the oxygen exchange with the atmosphere they consider the formation of threefold and fourfold positively charged Ti interstitials (Ti_i³⁺, Ti_i⁴⁺) as well as Ti vacancies (V_{Ti}⁴⁺). All equilibrium constants were determined from measurements above 850°C. Since this is one of the most comprehensive accounts of defect chemical equilibria in titania found in literature this model was the basis to estimate defect chemical properties of titania thin films used in the present study. There are, however, a few differences between the samples and measurement conditions that underlie the data used by Nowotny *et al.* and this work:

<u>Nowotny <i>et al.</i> [78]</u>	<u>this work</u>
bulk sample	thin film
rutile	anatase + unknown phase
$T \geq 850^\circ\text{C}$	$350^\circ\text{C} \leq T \leq 450^\circ\text{C}$

Due to these differences only estimations about the behaviour of the samples used in this work can be made. To check their plausibility a conductivity (σ) vs. oxygen partial pressure ($p(\text{O}_2)$) curve was calculated from this defect model and an attempt was made to compare it to other σ vs. $p(\text{O}_2)$ measurements in literature. The defect chemical equations given in [78] were numerically solved using the mathematics software

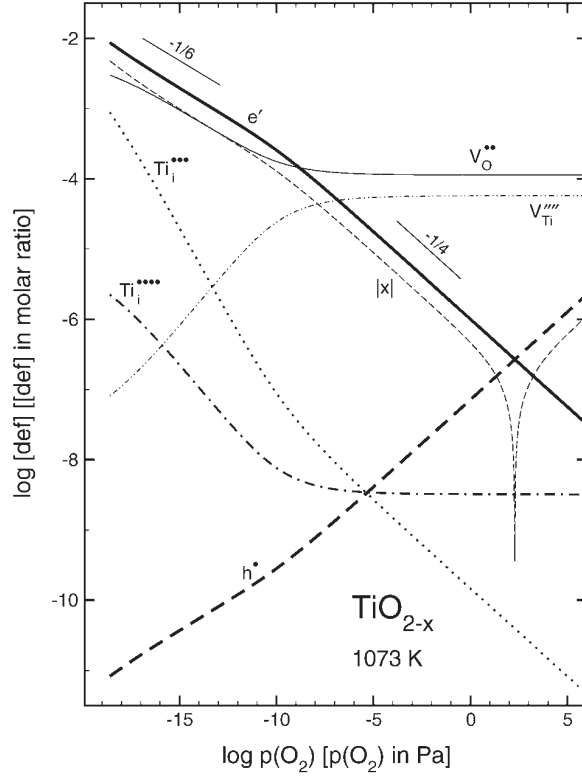


Figure 1.1: Brouwer diagram for TiO_2 at 800°C [63].

"Maple 18" (Maplesoft) to give the defect concentrations as a function of $p(\text{O}_2)$. The unit of the defect concentrations calculated was $\frac{\text{mol}}{\text{mol TiO}_2}$, as in figure 1.1, which had to be converted to defects per cm^{-3} for further use:

$$\underbrace{\frac{\text{mol defect}}{\text{mol TiO}_2}}_{\text{ratio}} \cdot \underbrace{\frac{\rho_{\text{TiO}_2} [\text{g cm}^{-3}]}{M_{\text{TiO}_2} [\text{g mol}^{-1}]}}_{\text{no. of moles per cm}^{-3}} \cdot N_A [\text{particles mol}^{-1}] = \text{concentration} [\text{particles cm}^{-3}]. \quad (1.1)$$

The density ρ of the rutile phase is 4.17 g cm^{-3} [80], the molar mass of titania M_{TiO_2} is $79.865 \text{ g mol}^{-1}$ [81]. The symbol N_A denotes Avogadro's number (approx. 6.022×10^{23} [82]). Then, the total conductivity was calculated according to

$$\sigma_{\text{tot}} = \sigma_{e'} + \sigma_{h^{\cdot}} + \sigma_{V_{\text{O}}^{\cdot\cdot}} \quad (1.2)$$

$$= [e'] \cdot \mu_{e'} \cdot e + [h^{\cdot}] \cdot \mu_{h^{\cdot}} \cdot e + [V_{\text{O}}^{\cdot\cdot}] \cdot \mu_{V_{\text{O}}^{\cdot\cdot}} \cdot 2e \quad (1.3)$$

with σ_{tot} denoting the total conductivity and $\sigma_{e'}$, $\sigma_{h^{\cdot}}$ and $\sigma_{V_{\text{O}}^{\cdot\cdot}}$ representing the electron, hole and oxygen vacancy conductivity, respectively. The symbols $\mu_{e'}$, $\mu_{h^{\cdot}}$ and $\mu_{V_{\text{O}}^{\cdot\cdot}}$ denote the respective mobilities, e is the elementary charge (approx. $1.602 \times 10^{-19} \text{ C}$ [83]). Contributions by Ti vacancies and interstitials were neglected because their mobility is expected to be very low due to their high charge. In case of the Ti interstitials, their concentration is additionally a few orders of magnitude lower than the concentration

of the other charge carriers. The mobilities for e' and h' were taken from [68]:

$$\mu_{e'} = 0.106 \text{ cm}^2 \text{ V}^{-1} \text{ s}^{-1} \quad (1.4)$$

$$\mu_{h'} = (1.05 \pm 0.89) \frac{10^6}{T} \exp\left(-\frac{0.853 \pm 0.073 \text{ eV}}{kT}\right). \quad (1.5)$$

The symbols k and T denote Boltzmann's constant (approx. $8.617 \times 10^{-5} \text{ eV/K}$ [84]) and the temperature, respectively. The mobility for V_{O}^{\bullet} was calculated from the self-diffusion coefficient for oxygen vacancies $D_{V_{\text{O}}^{\bullet}}$ via the Nernst-Einstein equation [54, p. 260]:

$$D_{V_{\text{O}}^{\bullet}} = \frac{\mu_{V_{\text{O}}^{\bullet}} kT}{2e}. \quad (1.6)$$

The diffusion data for the oxygen vacancies were taken from [85]. There, the diffusion coefficient was found to be independent of $p(\text{O}_2)$ and was given at 1000°C and 1100°C . The mobility used for V_{O}^{\bullet} is

$$\mu_{V_{\text{O}}^{\bullet}} = \frac{9.32}{T} \exp\left(-\frac{0.87 \text{ eV}}{kT}\right) \text{ cm}^2 \text{ V}^{-1} \text{ s}^{-1}. \quad (1.7)$$

The thus obtained conductivity data were first compared to the conductivity data measured in [85]. Both studies are based on measurements on rutile at high temperatures, so they should be comparable very well. The data points were read from a figure and re-plotted together with the calculated data, see figure 1.2. Two versions of calculated data are shown: For the calculation of the full line all defect chemical equilibria given in [78] were used, whereas the dashed line was obtained by omitting the formation of Ti vacancies. This was done because it takes a very long time until Ti vacancies are in equilibrium with the surrounding atmosphere (several 1000 h at 850°C for a $2 \times 3 \times 10 \text{ mm}^3$ single crystalline rutile slab [72, 75]) so this state might not always be established. The quantitative agreement between the calculated values and [85] is acceptable, the values are about one order of magnitude apart. However, the slopes are different, no matter which curves are compared. These deviations cannot be explained without further investigation but the calculated values would be sufficient to get a good guess about the conductivity's order of magnitude.

For the calculation of conductivity in this work an extrapolation had to be done down to the typical measurement temperatures ($350\text{-}450^\circ\text{C}$). To estimate whether the extrapolated data can be applied to anatase at lower temperatures literature data on conductivity under these conditions had to be found. Two suitable studies are [86] and [87]. They share many common features (see table 1.2) so the data can be expected to be comparable. However, there are substantial differences in the conductivity vs. $p(\text{O}_2)$ data in these two studies. In [86] the slope of these curves was found to be $-1/2$ (figure 1.3), whereas in [87] it was $-1/5$ or $-1/6$ (figure 1.4). The difference becomes especially apparent if the values for the temperature around 580°C are compared. Given this unclear situation a comparison of the calculated and extrapolated data from [78] and [85] is unfortunately meaningless. The calculations will still be used in this work for rough estimations but with the possibility of committing systematic errors by extrapolation in mind.

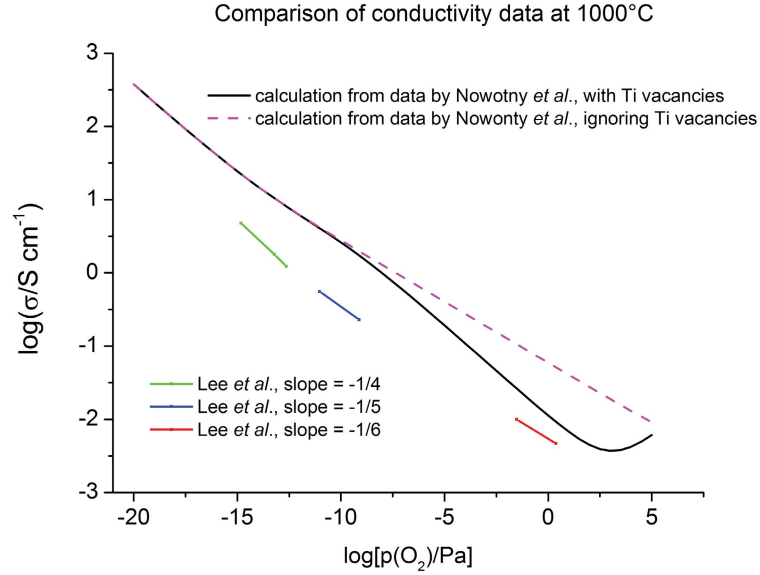


Figure 1.2: Comparison of conductivity data calculated from [78] with μ_{V_O} from [85] (full, black and pink, dashed lines) with conductivity data from [85] (green, blue and red lines).

Table 1.2: Comparison of crucial sample preparation and measurement parameters in [86] and [87]

	Knauth & Tuller, 1999 [86]	Weibel, Bouchet & Knauth, 2006 [87]
modification	anatase	anatase
preparation of powder	sulfate route, calcined at 300°C	sulfate route, calcined in air for 1 h at 800°C
preparation of pellets	pressed at 1 GPa for 2 h	cold compacted at 0.2 GPa, then pressed at 0.44 GPa and heated to 585°C for 2 h
grain size	35±10 nm	70±35 nm
main impurity	Na, ≈1300 ppm	Na, 930..1300 ppm
measurement method	impedance spectroscopy	impedance spectroscopy

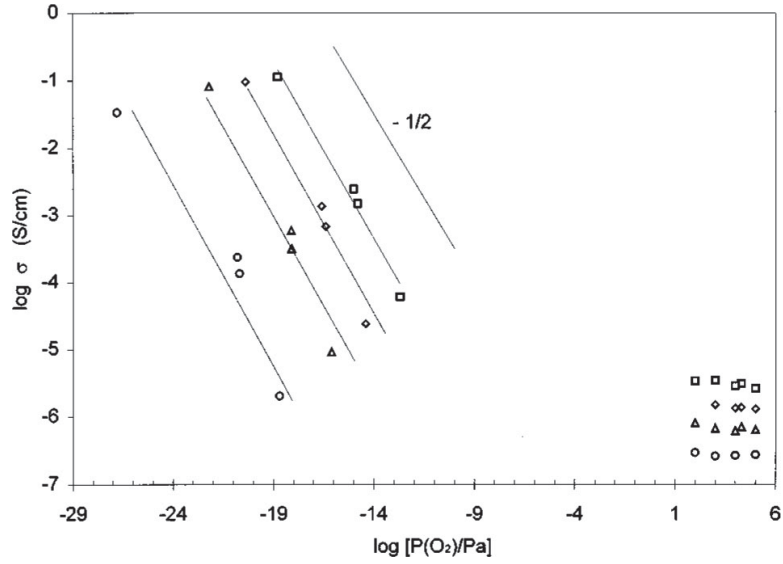


Figure 1.3: Figure 3 from [86]. The slope of the $\log(\sigma)$ vs. $\log(p(\text{O}_2))$ curve is $-1/2$.

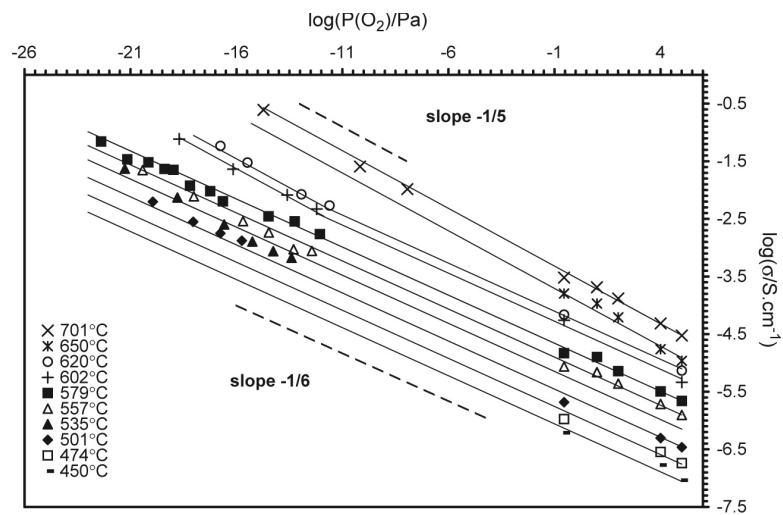


Figure 1.4: Figure 5 from [87]. The slope of the $\log(\sigma)$ vs. $\log(p(\text{O}_2))$ curve is $-1/5$ or $-1/6$.

1.1.5 SrTiO₃

Just as titania, STO has been used in liquid photoelectrochemistry (see above) as well as in high temperature studies that address its defect related properties. In solid state ionics it is considered a model material that generally represents electroceramic oxides, which are for example used in capacitors, positive temperature coefficient resistors or sensors and actuators, and particularly perovskites, which are widely used in solid oxide fuel cells [51, 88]. Therefore, its defect chemistry was subject to numerous studies (e.g. [89–91], and references therein). The works by Denk *et al.* [92] and Bieger & Maier [93] are particularly interesting because they present a defect chemical model (including mobilities for electrons, electron holes and oxygen vacancies) and chemical diffusion coefficients and surface exchange coefficients for weakly Fe-doped STO, respectively. In contrast to the defect data for TiO₂ the study by Denk *et al.* was conducted within the same temperature range as the present work, so extrapolation is not necessary.

1.1.6 Solid state photoelectrochemical studies

To the best of the author's knowledge the only investigations which deal with the influence of light on defect related properties of TiO₂ and STO were carried out by Gundlach & Heusler [94, 95] and Merkle *et al.* [96], respectively.

Gundlach & Heusler grew TiO₂ thin films on a Ti metal substrate by anodic oxidation in a liquid electrolyte. These films were subsequently reduced by placing the sample in a vacuum. Then, air was admitted again and the mass change was monitored *via* a quartz crystal microbalance (QCM). Upon irradiation with UV light that can excite electrons across the band gap they observed the mass to increase faster than without light.

Merkle *et al.* subjected a weakly Fe-doped STO single crystal to a jump in oxygen partial pressure while measuring its oxygen content by optical spectroscopy. They observed a faster oxygen incorporation when the sample was irradiated with UV light that can excite electrons into the conduction band.

In short, both studies found the oxidation kinetics to be faster with UV light.

A more recent theoretical study using a combination of other materials was done by Ye *et al.* [97].

1.2 Aims of this work

The studies by Gundlach & Heusler [94, 95] and Merkle *et al.* [96] suggest that there is an influence of light on the kinetics of the oxygen exchange reaction in TiO₂ and SrTiO₃. However, light may affect further defect chemistry related properties in oxides. Therefore, the aims of this work are to

- find experimental setups that allow the observation of any kind of light effects on oxide-based systems at elevated temperature
- find ways to prepare the needed (thin film) samples
- measure light effects as a function of defect chemically relevant parameters such as temperature, atmosphere, dopant content, etc.

- relate the observed effects to defect chemical properties of the materials and incorporate them into the existing models.

2 Experimental aspects

2.1 Sample preparation

2.1.1 SrTiO₃ samples

Samples with a thick single crystalline working electrode

5×5×0.5 mm³ STO single crystals polished on both sides were obtained from Crystec, Germany. An approximately 900 nm thick Y_{0.16}Zr_{0.84}O_{3-δ} (YSZ) thin film was deposited by pulsed laser deposition (PLD) using a Kr/F excimer laser (Lambda COMPex Pro 205F, wavelength $\lambda = 248$ nm; PLD parameters see table 2.1). The same target as in [98] was used (8 mol% YSZ from Tosoh, Japan - pressed, then sintered at 1200°C). After deposition the crystals were sometimes broken into smaller pieces in order to obtain more samples. On top of the STO single crystal a metal (Pt or Au) thin film with a thickness of about 100 nm was applied by DC magnetron sputtering (BAL-TEC MED 020 Coating System, Pt and Au targets with 99.95% purity obtained from Ögussa, Austria; sputtering parameters see table 2.2). It was microstructured into a current collector grid (stripes of 15 μm width with distance of 35 μm) by lift-off photolithography or standard photolithography and subsequent ion beam etching (photoresist: micro resist technologie ma-N 1420, developer: microresist technologie ma-D 553S). Finally a porous Pt counter electrode was brushed on and dried for about half an hour at around 100°C (Pt paste obtained from Gwent Group, item number C2000904P3, United Kingdom).

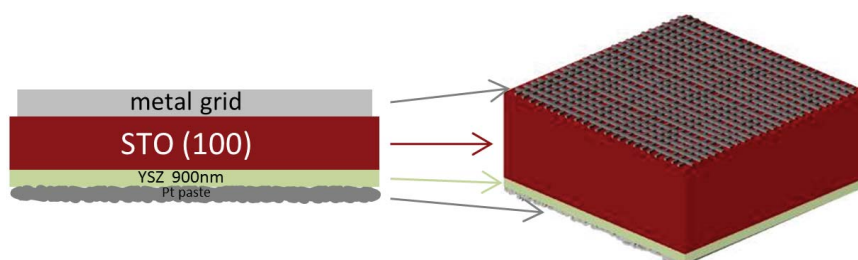


Figure 2.1: Schematic representation of an STO sample.

For each metal one sample was produced.

A separate sample was prepared for characterization of the YSZ thin film (STO_YSZ_XRD). It consisted of a YSZ thin film on single crystalline STO (10×10×0.5 mm³, Crystec) only, deposited under the same conditions as the YSZ layers on the electrochemically measured samples. The morphology was investigated by scanning electron microscopy (SEM; FEI Quanta 200 FEG), the crystal structure was determined by grazing incidence X-Ray diffractometry (XRD). The data were recorded on a PANalytical Empyrean diffractometer with PIXcel3D 1×1 detector, the Cu X-ray tube

Table 2.1: PLD parameters for the deposition of YSZ and STF0.4

parameter	YSZ	STF0.4
desired film thickness/nm	900	150
distance target-furnace/cm	4	5.5
sample temperature/°C	590-640	approx. 650°C
O ₂ pressure/mbar	4×10^{-2}	1.5×10^{-1}
pulse rate/Hz	10	5
laser energy per pulse/mJ		400
deposition time/min	60	15

Table 2.2: Sputtering parameters for Pt and Au

parameter	value	
	Pt	Au
desired film thickness/nm		100
Ar pressure/mbar	2×10^{-2}	1×10^{-2}
current/mA	100	50
sputtering time/s	150	80

operating at 45 kV and 40 mA. The incident beam angle was 2°. PANalytical’s “High-Score” software was used to compare the measured diffractogram to literature data in the ICDD PDF-4+ 2014 database.

Figure 2.2 shows the resulting X-ray diffractogram of the YSZ thin film on sample STO_YSZ_XRD. The layer can clearly be identified as YSZ.

The SEM micrograph in figure 2.3 (a) shows the cross section of the sample after it had been broken apart. The YSZ layer with a thickness of approximately 930 nm can clearly be seen. The measured thickness is in good agreement with the desired value of 900 nm. In panel (b) a top view of the surface is shown. Small holes or dents are visible. In panel (d) such a dent is magnified. From the data available by SEM it cannot be judged whether the hole reaches down to the STO substrate or not. So, the possibility of a parallel electronic short-circuit path has to be considered when interpreting the results of the electrochemical measurements. Apart from the holes the layer looks dense (panel (c)).

Sample with a thin film electrode

A YSZ (100) single crystal ($10 \times 10 \times 0.5 \text{ mm}^3$) was obtained from Crystec, Germany. A $\text{SrTi}_{0.996}\text{Fe}_{0.004}\text{O}_{3-\delta}$ (STF0.4) thin film of about 150 nm thickness was deposited by PLD (equipment see above, parameters see table 2.1, same target used as in [99, p. 24]), then the crystal was broken into smaller pieces. Afterwards, a Pt current collector grid and a porous Pt counter electrode were applied in the same way as for the single crystalline STO samples.

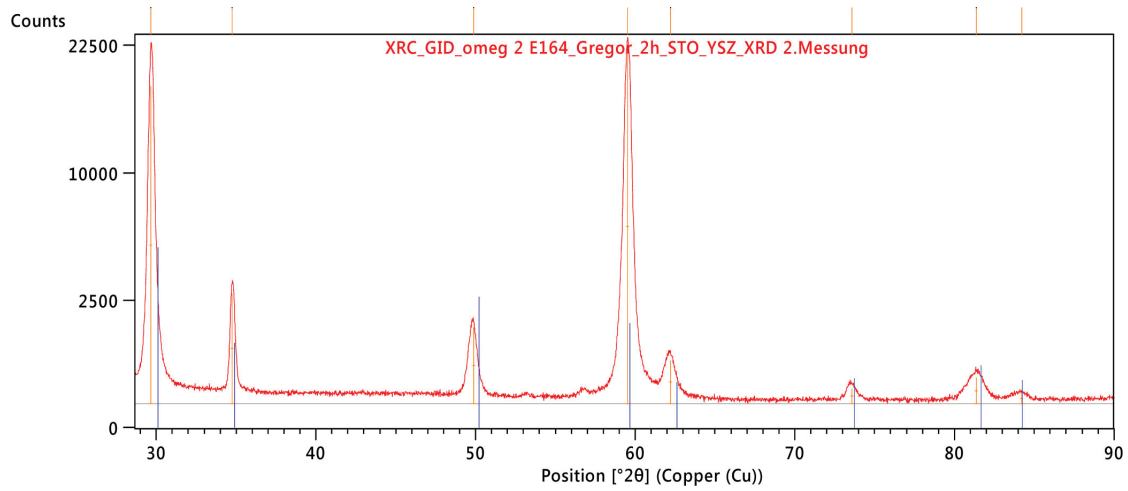


Figure 2.2: Grazing incidence X-ray diffraction pattern of sample STO_YSZ_XRD. By comparison with the database pattern (PDF 04-018-5452; 6 mol% YSZ, blue lines) the layer can be identified as YSZ.

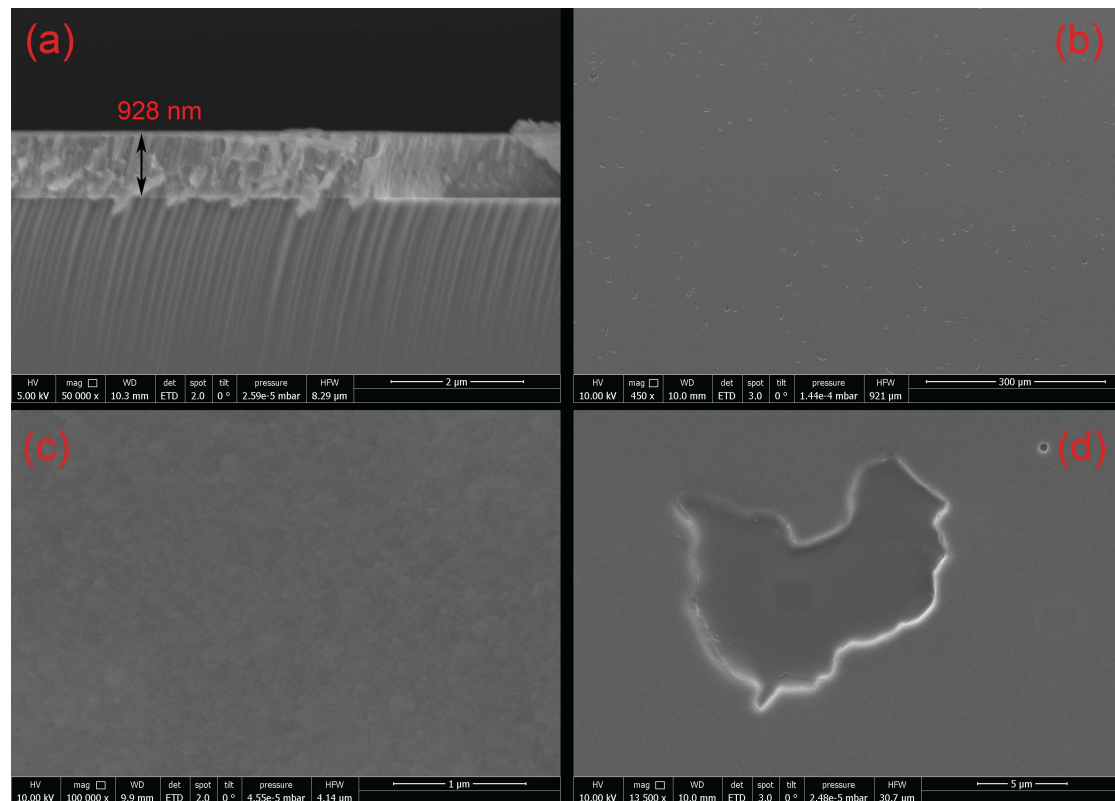


Figure 2.3: SEM micrographs of the YSZ layer on sample STO_YSZ_XRD. (a): The film thickness is around 930 nm, which is close to the desired thickness of 900 nm. (b): The surface has holes/dents (magnification in (d)). (c) Apart from the dents the layer looks dense.

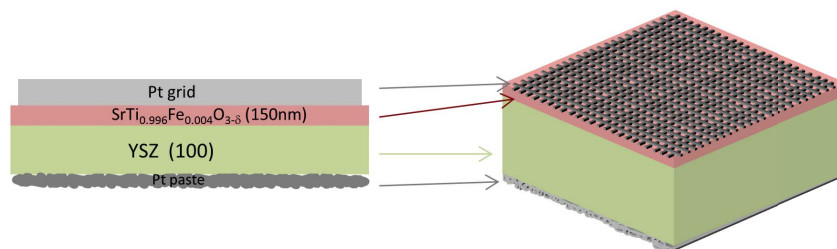


Figure 2.4: Schematic representation of the STF0.4 sample

2.1.2 TiO₂ samples

The aim of the TiO₂ thin film preparation experiments was to produce a TiO₂ thin film on YSZ which remains stable within several measurements.

The polymorphism of titania (see subsection 1.1.4) has to be considered when preparing titania samples because a phase transition while measuring might cause artefacts that are hard to identify. It turned out that measurements between approximately 400°C and 600°C were most promising and the measurement durations were up to a couple of ten hours (see chapter 3). If several measurements were to be performed on the same sample it had to be stable for at least a few days at these temperatures. From literature it is known that the anatase to rutile phase transition depends on many parameters such as heating rate, impurities, volume of the sample, measurement technique and so on [56, p. 858]. As a rough guideline this transition temperature can be regarded to be around 600°C, but also lower temperatures have been reported [56, p. 862], [100]. Therefore, the first approach was to produce the rutile phase.

In order to check the phase of the resulting thin film grazing incidence X-ray diffraction patterns (incident beam angle: 2°) were recorded on a PANalytical Empyrean diffractometer with a PIXcel3D 1x1 detector with the Cu X-ray tube operating at 45 kV and 40 mA. For phase identification literature diffractograms from the ICDD PDF-4+ 2014 database were compared to the measured data using PANalytical's "HighScore" software.

Sputtering

While there are several reports on the production of anatase thin films by sputter deposition in literature (e.g. [101–104]), fewer studies deal with sputtered rutile thin films. An example for rutile thin films deposited on quartz substrates by reactive DC magnetron sputtering from a Ti target is the study by Sarma *et al.* [105]. The DC magnetron sputtering technique using a Ti target in Ar atmosphere was applied by [106] and [107] (in the latter case the Ti target partially covered by TiO₂).

As in these studies post-annealing was necessary also for reactively sputtered films the experimentally easier method with pure Ar as a processing gas was chosen to be attempted in the present study. Samples were prepared on the same equipment as above using a Ti target (supplied with the BAL-TEC sputtering machine). Additionally, a quartz crystal microbalance (QCM; BAL-TEC QSG 100) was used to monitor the film thickness. Table 2.3 shows sputtering parameters from [106] and [107] compared to the ones used in this study. The parameters used in this study differ from the ones found

Table 2.3: Sputtering parameters for Ti in literature and in this study

parameter	[106]	[107]	this work
substrate	quartz	quartz	quartz glass/YSZ (100)
desired film thickness/nm	170	?	100-350
Ar pressure/mbar	1.07×10^{-2}	7.5×10^{-6}	7×10^{-3}
measure for energy	?	power = 100 W	current = 100 mA
sputtering time/s	900	3600	750...4120

in literature because due to the differences in equipment not all the parameters can be taken from other authors (e.g. different target-sample distance, different vacuum range accessible, different power control, etc.). Some values were even not reported.

After deposition the samples were annealed in air. Heat treatments in literature that resulted in rutile formation were 1h/700°C [105, 106] and 1h/1100°C [107].

Table 2.4 shows annealing parameters and results in the present study (*d*... desired film thickness, t_{anneal} ... annealing time, T_{anneal} ... annealing temperature, t_{sput} ... sputtering time, r_{sput} ... sputtering rate, d_{QCM} ... film thickness measured by QCM).

Table 2.4: Results of post-annealing of TiO₂ thin film samples

sample name	substrate	d/nm	t _{anneal} /T _{anneal}	t _{sput} /s	r _{sput} /nm s ⁻¹	d _{QCM} /nm	crystal structure (XRD)	comment
Quarz_Ti_002	quartz	100	2h/900°C	750	no QCM	no QCM	anatase	sputtered together with Quarz_Ti_003
Quarz_Ti_003	quartz	100	10h/1200°C	750	no QCM	no QCM	amorphous	
Quarz_Ti_004	quartz	200	2h/900°C	2997	0.08...0.1	155	anatase	
Quarz_Ti_005	quartz	200	10h/1200°C	2997	0.08...0.1	155	rutile, but unexplained peaks	
Quarz_Ti_006	quartz	100	10h/1000°C	750	0.05...0.07	45	amorphous	After deposition sample looks shiny, golden, el. conductive.
Quarz_Ti_007	quartz	200	10h/1000°C	1998	≈0.15	300	rutile	
Quarz_Ti_008	quartz	100	10h/1000°C	≈1540	0.12...0.15	200	rutile	Pre-sputtering for 78 min, sample looks metal-like, golden.
YSZ_TiO2_Ana_XRD_001	YSZ	100	2h/550°C	1560	no QCM	no QCM	anatase	
YSZ_TiO2_Ana2-550_XRD_002	YSZ	350	2h/550°C	4120	up to approx. 60 min: 0.08, then 0.12...0.15	350	mix anatase and rutile	
YSZ_TiO2_Ana2-550_XRD_003	YSZ	100	2h/550°C	1740	≈0.07	100	anatase, but two unexplained peaks	
YSZ_TiO2_Ana2-550_XRD_004	YSZ	100	2h/550°C	≈1430	0.05...0.08	100	anatase, but unexplained peak	
YSZ_TiO2_Ana2-550_XRD_005	YSZ	100	2h/550°C	1853	0.05...0.08	100	anatase, but unexplained peak	
YSZ_TiO2_Ana2-550_XRD_006	YSZ	100	2h/550°C	1862	≈0.07	100	anatase, but unexplained peak	
YSZ_TiO2_Ana2-550_XRD_007	YSZ	100	2h/550°C	1556	≈0.07	100	anatase, but unexplained peak	
YSZ_TiO2_Ana2-550_XRD_008	YSZ	100	2h/550°C	1684	0.05...0.08	100	anatase	
YSZ_TiO2_Ana2-550_XRD_009	YSZ	100	2h/550°C	1799	0.05...0.07	≈108	anatase	
YSZ_TiO2_Ana2-900_XRD_001	YSZ	100	2h/900°C	1520	floating	80	anatase (many peaks missing)	
YSZ_TiO2_Ana2-900_XRD_002	YSZ	350	2h/900°C	4120	up to approx. 60 min: 0.08, then 0.12...0.15	350	mix anatase and rutile	sputtered together with YSZ_TiO2_Ana2-550_XRD_002
YSZ_TiO2_Ana2-900_XRD_003	YSZ	100	2h/900°C	1149	≈0.07	100	anatase, but unexplained peaks	

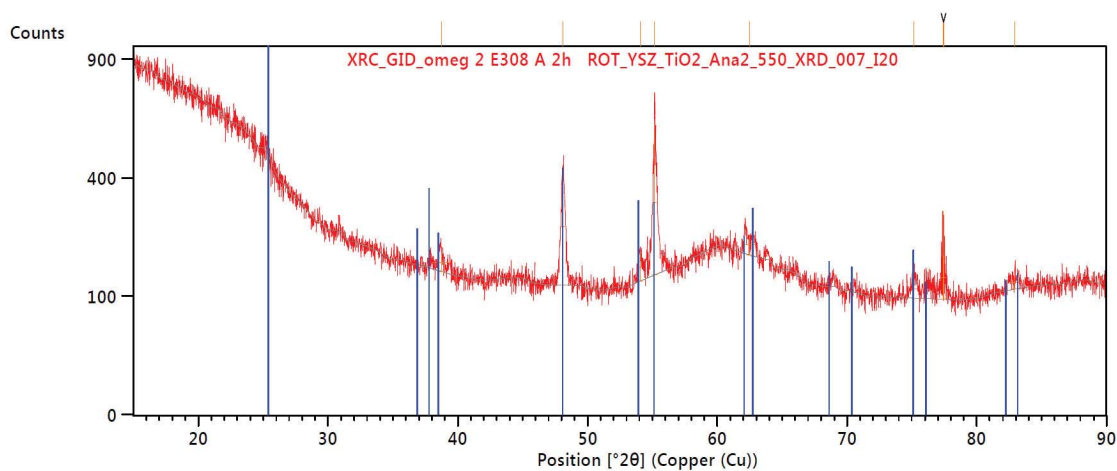


Figure 2.5: X-ray diffractogram of sample YSZ_TiO2_Ana2-550_XRD.007. All peaks correspond to the database anatase structure (PDF 00-004-0477 shown as blue lines), except for the one at around 77.5°.

Figures 2.5 to 2.10 show X-ray diffractograms of samples YSZ_TiO2_Ana2-550_XRD.007, YSZ_Ana2-550_XRD.008, Quarz_Ti.005, Quarz_Ti.008 (as deposited), Quarz_Ti.008 (after annealing) and YSZ_TiO2_Ana2-900_XRD.003 respectively, to exemplify the results of the annealing experiments. The outcome of the XRD measurements in its entirety is included in table 2.4.

Analyzing the results from all sputtering experiments, several observations can be made:

- The conversion of the deposited material to rutile did not readily occur even at annealing temperatures well above 600-700°C. Either the rutile phase formed (but unexplained peaks in the XRD occurred), the anatase phase remained, or the film became amorphous.
- Two different sputtering rates could be observed: 0.05...0.08 and $\geq 0.012 \text{ nm s}^{-1}$.
 1. The higher sputtering rate appeared chiefly after long pre-sputtering (samples Quarz_Ti.008 and YSZ_TiO2_Ana2-550_002 or YSZ_TiO2_Ana2-900_002; see also deposition rate during sputtering with spectroscopy, next paragraph). The samples produced with this higher sputtering rate looked shiny and golden, on one sample electrical conductivity could be measured with a hand-held Ohm meter. By XRD the material was found to be TiN (see figure 2.8). Regardless of the substrate, the material converted to rutile after annealing. If both sputtering rates occurred a mixture of rutile and anatase resulted.
 2. Samples produced with the lower sputtering rate looked mostly grey.
- Layers sputtered with the lower sputtering rate could be converted to anatase by thermal treatment but often there were unexplained peaks. The production of anatase (+ unidentified phase) thin films on YSZ was reproducible with 2 h of annealing at 550°C in air (8 samples with YSZ substrate), but also with 2 h at 900°C (2 samples on YSZ, 2 samples on quartz glass).

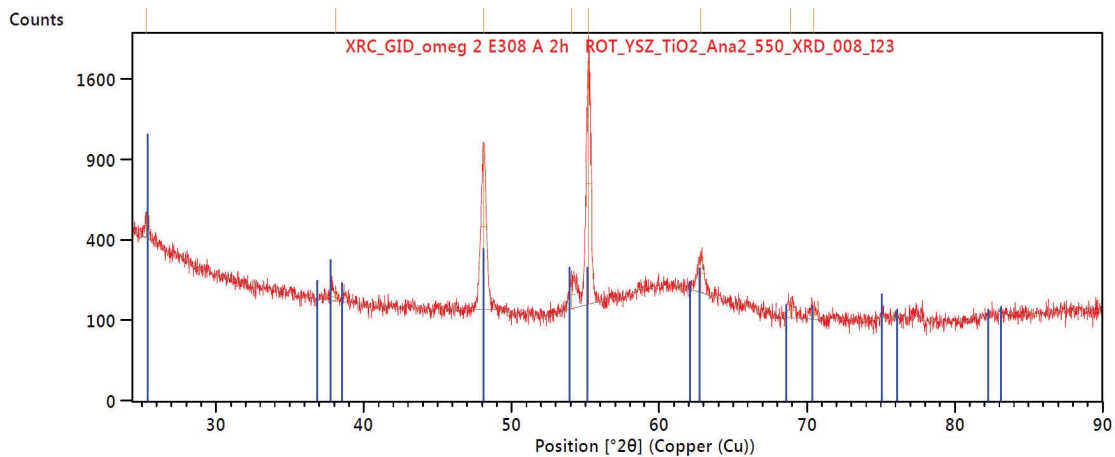


Figure 2.6: X-ray diffractogram of sample YSZ_TiO2_Ana2-550_XRD_008 compared to PDF 00-004-0477 (anatase, blue lines). All of the peaks correspond to the anatase structure.

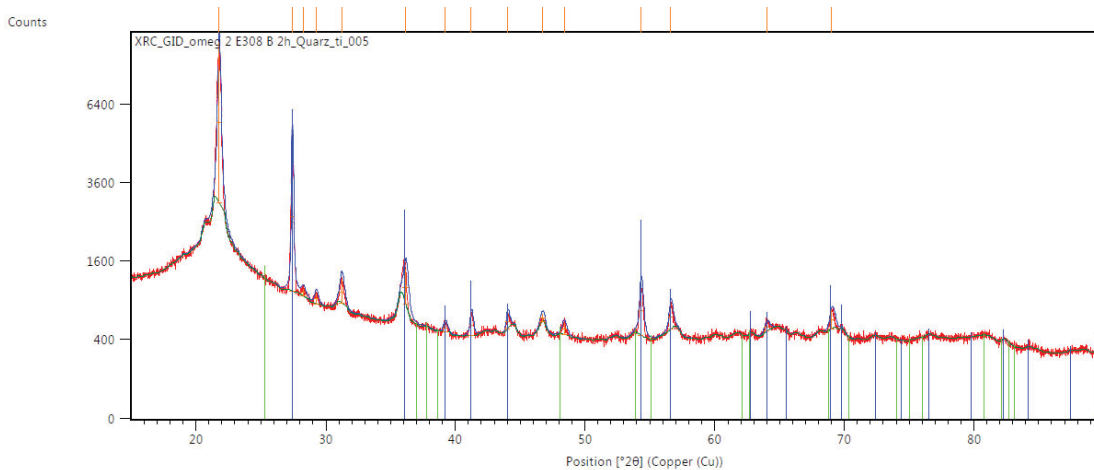


Figure 2.7: X-ray measurement of sample Quarz_Ti.005 compared to PDF 01-079-6029 (rutile, blue lines) and PDF 00-021-1272 (anatase, green lines). Anatase is not present, the rutile phase can be identified, but there are several unexplained peaks, among them the most intensive one at around 22° .

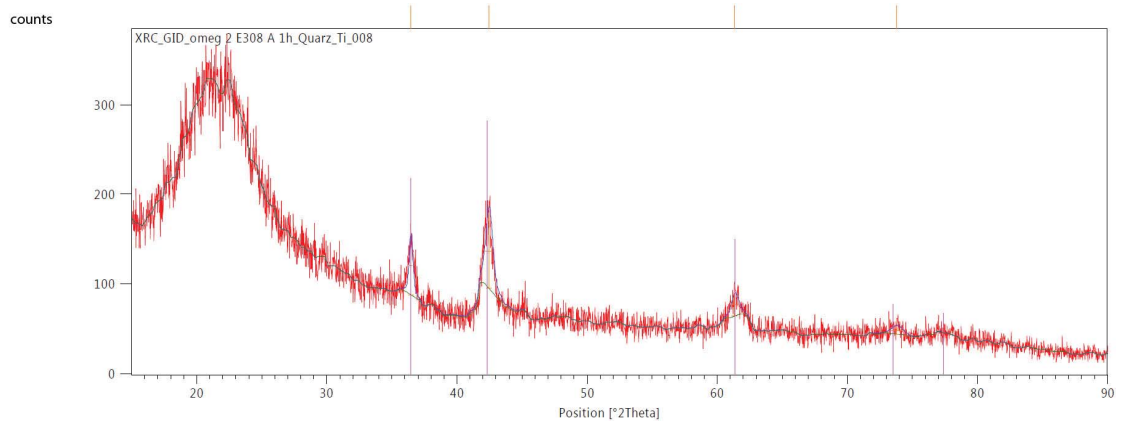


Figure 2.8: X-ray diffractogram of sample Quarz_Ti.008, as deposited, compared to PDF 04-016-4690 (TiN, pink lines). TiN can clearly be identified.

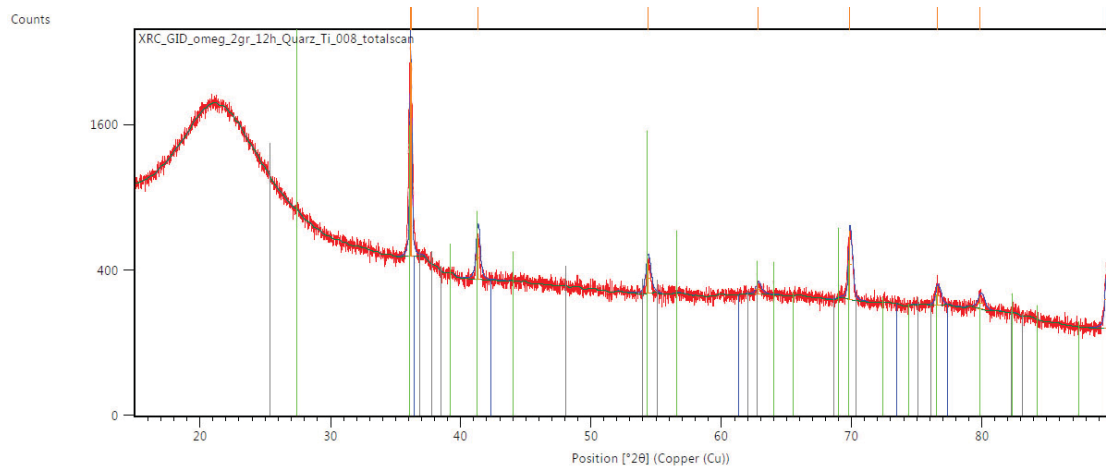


Figure 2.9: X-ray diffractogram of sample Quarz_Ti.008, after annealing for 10 h at 1000 °C, compared with PDF 04-003-0648 (rutile, green lines), PDF 04-016-4690 (TiN, blue lines) and 00-004-0477 (anatase, grey lines). All observed peaks correspond to the rutile phase.

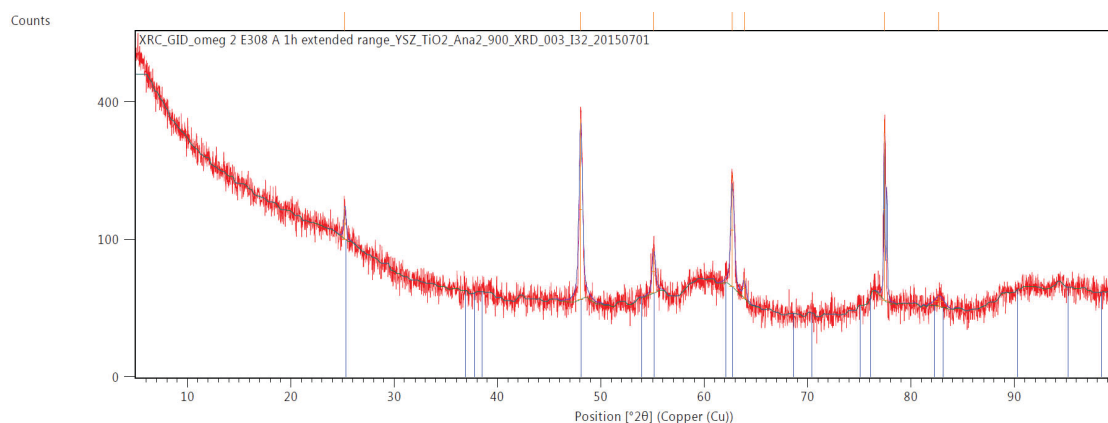


Figure 2.10: X-ray diffractogram of sample YSZ_TiO2_Ana2-900_003 compared to PDF 00-004-0477 (anatase, blue lines). Apart from anatase reflections, there are several unexplained peaks.

As it turned out that the desired rutile thin films could be produced from annealing TiN the origin of the different sputtering rates was investigated by optical spectroscopy with the possibility for a rutile thin film production path in mind.

Sputtering with optical spectroscopy Inspired by commercial spectroscopic sputtering control systems such as the PEM 05 by Von Ardenne Anlagentechnik, Dresden [108] which was used in [103] (Ti emission line at ≈ 453 nm), the sputtering process was monitored *via* plasma emission by means of an external spectrometer (QE 65000 by Ocean Optics, USA) placed next to the sputtering apparatus.

First, a UV/VIS transmission spectrum of the sputtering chamber's plastic wall was recorded using the spectrometer, Ocean Optics waveguides and a lamp which houses both a tungsten and a deuterium light source (model BDS 130 by BWTek, USA). The waveguides connected to the lamp and the spectrometer were clamped to laboratory tripods with the device under test placed in the beam path.

The measurements show that the polymer is acceptably transparent down to a wavelength of about 350 nm (see figure 2.11). The strong variation in the transmission between the three recorded spectra are due to the experimental setup which was very prone to shaking which caused the wave guides to move slightly out of axis. The sharp peaks in the spectrum result from saturation of the spectrometer's detector at the wavelengths of the characteristic deuterium emissions (approximately 486.0 nm and 656.1 nm [109]).

Then, the sputtering process was investigated. The setup is shown in figure 2.12. Sputtering rate (QCM), temperature (thermocouple type K placed in the middle of the recipient) and UV/VIS spectra of the light emitted by the plasma were recorded as a function of time. In order to record a typical spectrum without overloading the detector an integration time of 1 s was chosen and the average of two spectra was calculated by the Ocean Optics Spectra Suite software. After 15 min of sputtering the integration time was set to 20 s even though this caused detector overload in large parts of the spectrum because a more sensitive measurement provides higher resolution to the small intensity of the 453 nm Ti emission line which was the primary interest in this experiment.

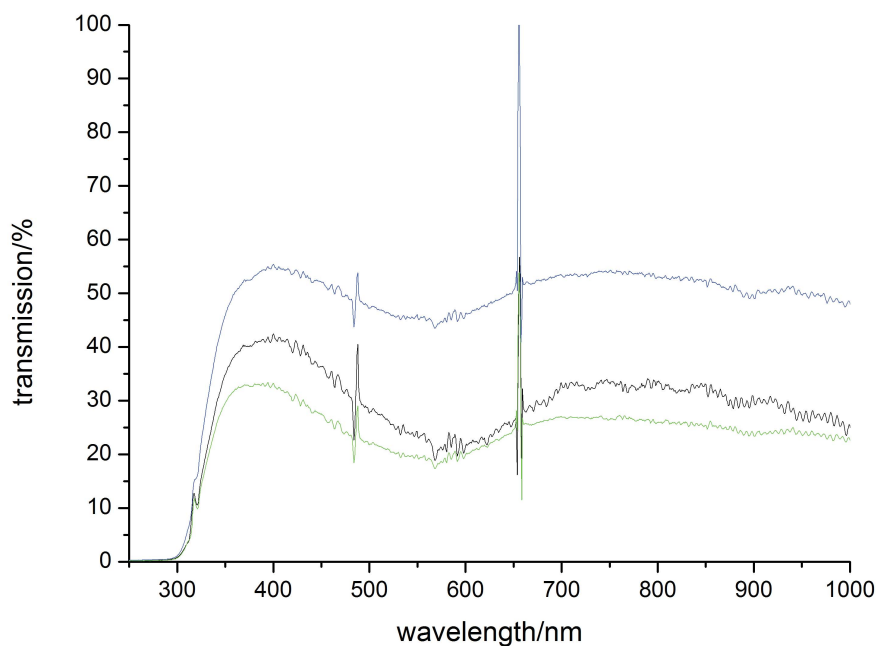


Figure 2.11: Several UV/VIS spectra of the sputtering chamber's plastic wall. It is acceptably transparent for $\lambda > 350$ nm.

The obtained spectra were compared with data from the NIST Atomic Spectra Database [109]. This database calculates the intensities of atomic spectra as a function of electron temperature T_e (given as an energy in eV). Since the kinetic energy of the electrons in the plasma is unknown the electron temperature value which fitted the measured spectra best was chosen (1 eV). Figure 2.13 shows a spectrum with 1 s integration time compared with a database spectrum for Ar I (the roman number indicates a neutral Ar atom [110]). Many peaks can be clearly identified as Ar I emission lines.

At approximately 656 nm there is a peak with considerable intensity which does not originate from an Ar emission. It can be identified as a hydrogen emission - H I has several of its most intensive emission lines between 656.27 nm and 656.29 nm [109]. Also, two other H I peaks can be found. A comparison of a measured spectrum (integration time 20 s) with the H I database spectrum is shown in figure 2.14. Hydrogen could be the product of dissociated residual water.

A comparison of the same measured spectrum with the Ti I database spectrum from [109] is shown in figure 2.15.

The Ti lines cannot be identified in such a straightforward manner as for Ar. This might be due to additional substances present in the gas which emit light in the same range as Ti. However, the 453 nm Ti emission line can be observed as a small shoulder.

During the sputtering process the intensity of the whole spectrum decreased. This can be witnessed in figure 2.16, where four spectra at different points in time during the sputtering process are shown.

The decrease in intensity can be attributed to deposition on the recipient's plastic wall

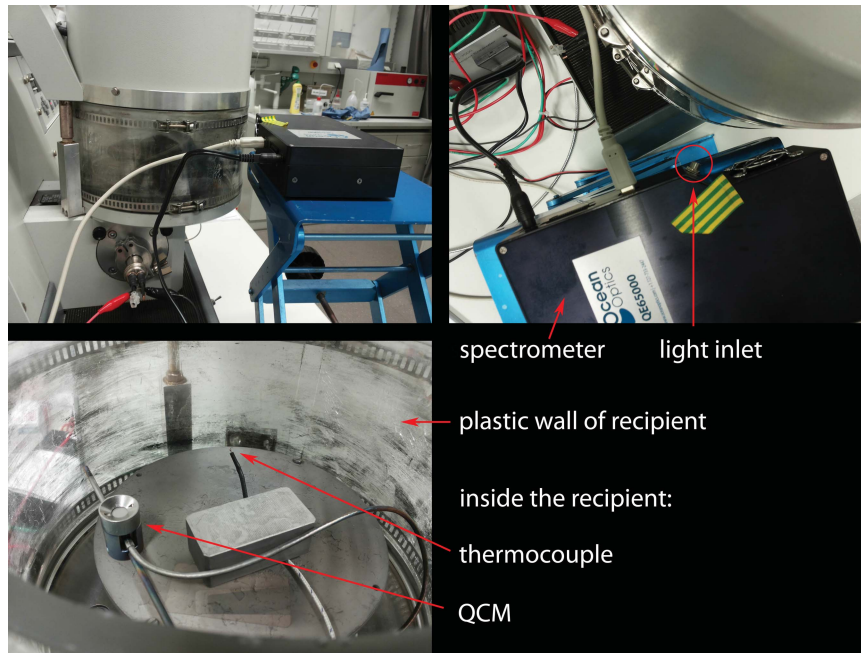


Figure 2.12: Setup for sputtering with spectroscopic monitoring. Top left: recipient of the sputtering machine with spectrometer on the blue lifting platform. The light inlet of the spectrometer was placed as close as possible to the recipient (top right). Thermocouple and QCM are shown inside the sputtering chamber in the bottom left image.

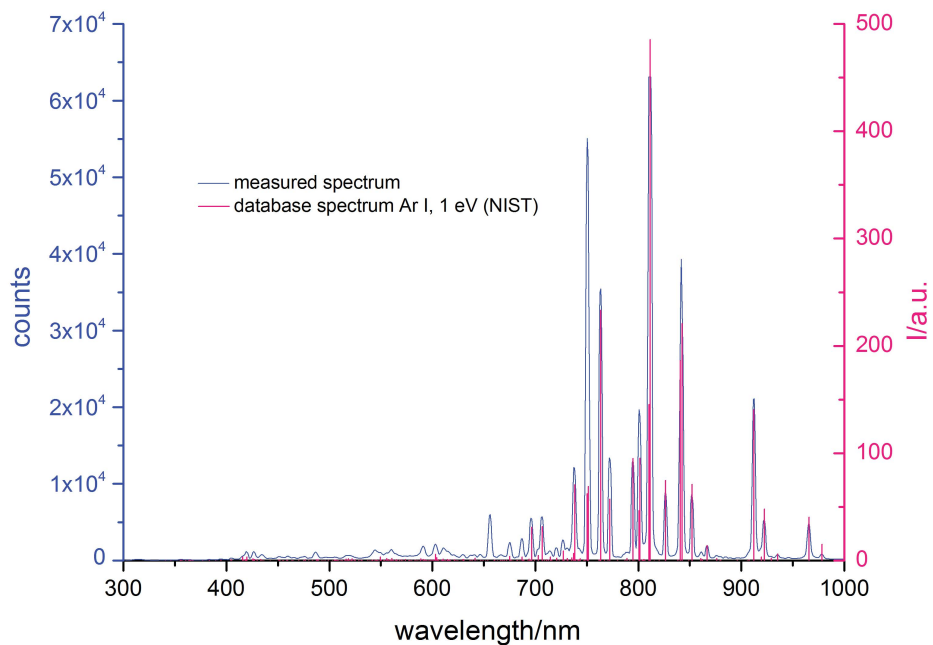


Figure 2.13: Typical plasma emission spectrum (integration time = 1 s, averaged over 2 spectra) compared with a database spectrum for Ar I ($T_e = 1$ eV).

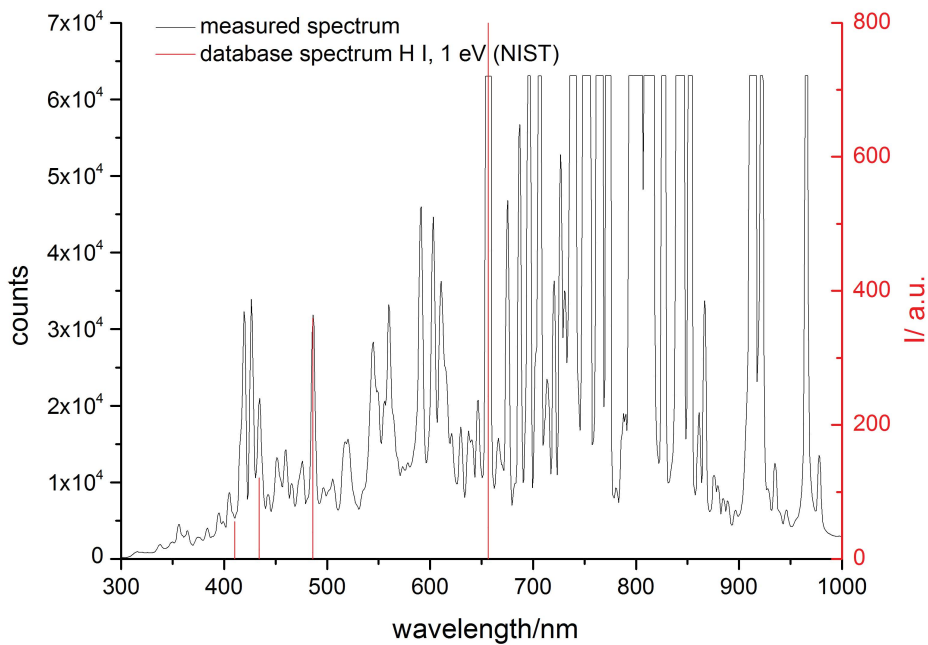


Figure 2.14: Typical plasma emission spectrum (integration time = 20 s, averaged over 2 spectra) compared with a database spectrum for H I ($T_e = 1$ eV).

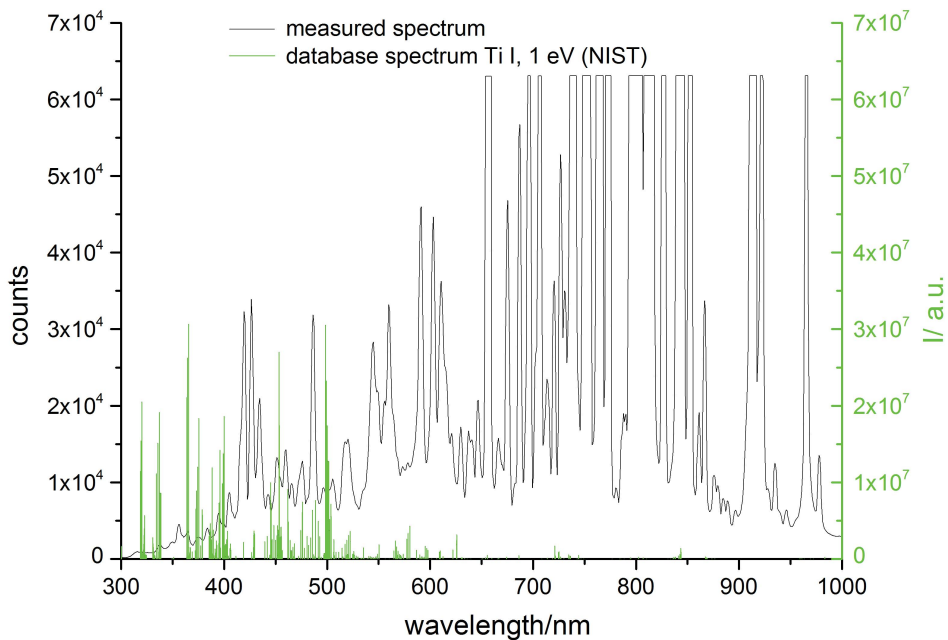


Figure 2.15: The same measured plasma emission spectrum as in figure 2.13 compared with a database spectrum for Ti I ($T_e = 1$ eV).

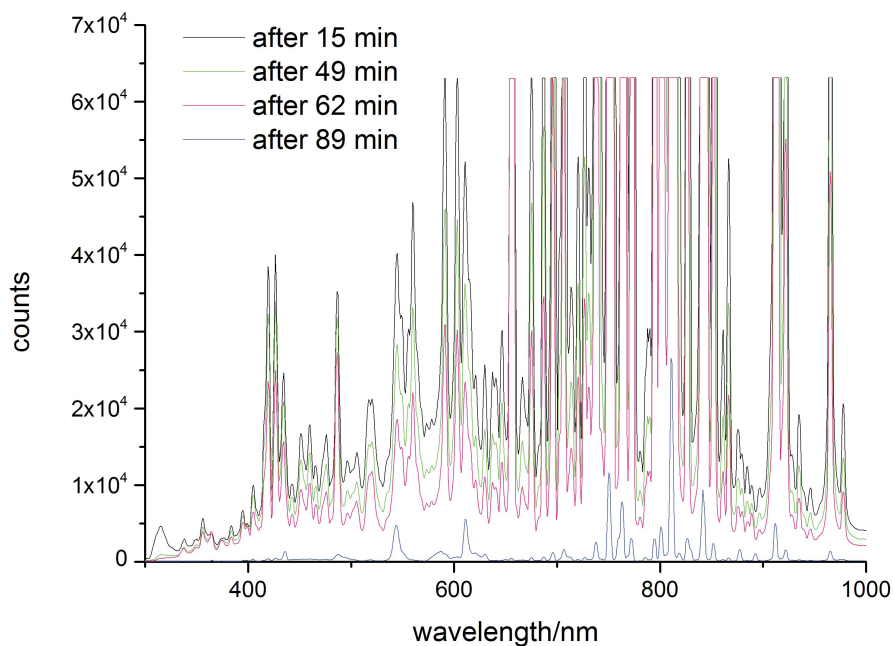


Figure 2.16: Comparison of 4 spectra: after 15, 49, 62 and 89 minutes sputtering time. Integration time = 20 s, averaged over 2 spectra.

which makes it less and less transparent. It can be evaluated quantitatively by observing the intensity of an Ar line. The wavelength of 603.04 nm was chosen to be representative for Ar because it is very close to an Ar emission line (≈ 603.21 [109]) and lies far enough from Ti emissions, of which the closest are at around 601.7 nm and 606.5 nm [109]. The intensity of this Ar emission is shown in figure 2.17 in the bottom panel as blue dots.

Likewise, the intensity of the 453 nm Ti emission line also decreased over time as a result of the plastic's reduced transparency (see figure 2.17, bottom panel, black squares). Assuming the emitted Ar I intensity is constant the overall decrease in measured intensity can be accounted for by dividing the Ti signal by the Ar signal. The resulting numbers are plotted in the same figure as red stars.

The QCM measurement yielded the two different sputtering rates already described on page 19. Additionally, there is a small change in sputtering rate after about 45 min. It is plotted in figure 2.17 in the top panel as red dots.

The measurement of the temperature shows an increase followed by a plateau, a small step up and finally a bigger step towards lower values. The temperature values are represented by the black squares in the top panel of figure 2.17.

Comparing sputtering rate, temperature and the corrected Ti emission intensity values a small and a big step in all three parameters can be observed (at 45 min and 75 min respectively).

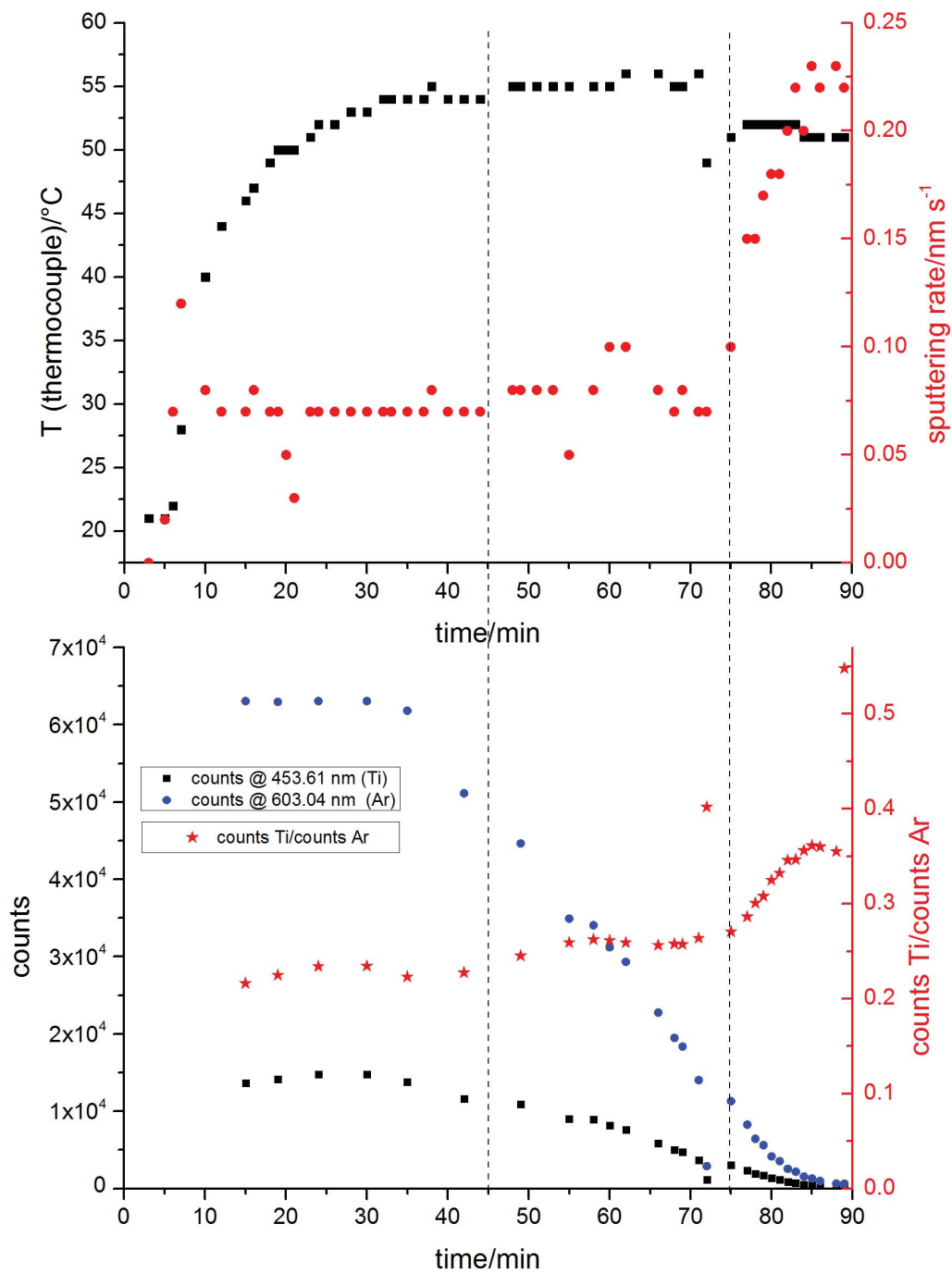


Figure 2.17: Results of the sputtering with spectroscopic monitoring. The top panel shows temperature and sputtering rate as function of time. The bottom panel shows the intensities of a Ti I and an Ar I emission line (≈ 453 nm and ≈ 603 nm, respectively) and their ratio.

This observation can be explained by the following hypothesis: During the first 75 min the native TiO₂ layer [61, S. 786] is sputtered off (with a small change at 45 min), then metallic Ti is ablated. The increasing Ti intensity in the spectroscopic measurement can be attributed to the “increased Ti content” in the sputtering target. Since TiO₂ is sputtered more slowly than Ti the rate is smaller at first and rises strongly as the TiO₂ layer vanishes. The changes in temperature can be explained by assuming that at the Ar pressure of 7×10^{-3} mbar heat transport by convection is negligible and occurs mainly *via* radiation. As the spectrum of the emitted light changes, also the measured temperature changes.

Summary of sputtering TiO₂ Combining the findings from spectroscopy, the XRD and QCM measurements it can be concluded that during the first approximately 75 min mainly TiO₂ is sputtered with a rate of about 0.07 to 0.1 nm s⁻¹. After annealing mainly anatase is formed.

Then, Ti metal is sputtered which forms TiN on the sample. TiN can be thermally oxidised to rutile, which was the desired product.

The downside of this rutile preparation method is the very long “pre-sputtering” time. Also, a second shutter is needed to prevent deposition on the sample during pre-sputtering while leaving the QCM open in order to control the process.

PLD

The deposition of rutile by PLD could not only provide an alternative way to sputtering but also the possibility to deposit doped titania, which would open up a whole new world of defect chemically interesting experiments. Therefore, the deposition of both doped and undoped rutile was attempted.

Deposition of undoped rutile There are studies that show the successful deposition of pure rutile by PLD on glass [111, 112] and on GaAs [113]. In the present study the parameters used in [113] were slightly adapted to meet the conditions realizable on the available PLD equipment. Both parameter sets are shown in table 2.5.

For the production of the target rutile powder (obtained from Aldrich, 99.99% trace metals basis purity) was compacted by cold isostatic pressing (approximately 3000 bar, 20 s) and subsequently sintered at 1300°C for 5 h. The pellet was analyzed by XRD on a Panalytical X'Pert Pro diffractometer (Θ/Θ geometry) with an X-ray tube with Cu anode (40 kV acceleration voltage, 40 mA current) and an X'Celerator detector. In the diffractogram no other phases than rutile can be identified (see figure 2.18).

Three thin film samples were produced, two with a deposition time of 50 min (samples YSZ_TiO2_PLD_001 and YSZ_TiO2_PLD_XRD_002) and one with 16 min 40 s. Assuming a similar deposition rate as in [113] (0.02-0.03 nm s⁻¹) the film thickness should be 300-450 nm and 100-150 nm, respectively. After deposition of the thin film the samples were annealed for 10 h at 1000°C in air.

The grazing incidence X-ray diffraction patterns (setup as described in subsection 2.1.2) showed varying results. A rutile thin film could be deposited successfully on sample YSZ_TiO2_PLD_001, see the diffraction pattern in figure 2.19. From an SEM micrograph (figure 2.20) the layer was observed to be dense and microcrystalline.

Table 2.5: PLD parameters for deposition of TiO₂ in literature and in this work

parameter	[113]		this work
laser		KrF, $\lambda = 248$ nm	
fluence at target/J cm ⁻²	2.5		1.5 [114]
laser pulse rate/Hz		5	
target		TiO ₂ powder, sintered at 1000°C for 5 h	see text
substrate		GaAs (100)	YSZ (100)
substrate temperature	700°C		≈ 705-720°C
distance target-furnace/cm		4	
deposition rate/nm pulse ⁻¹	0.02-0.03		?
base pressure/mbar	5×10^{-6}		≈ 5×10^{-5}
O ₂ pressure/mbar		5×10^{-2}	

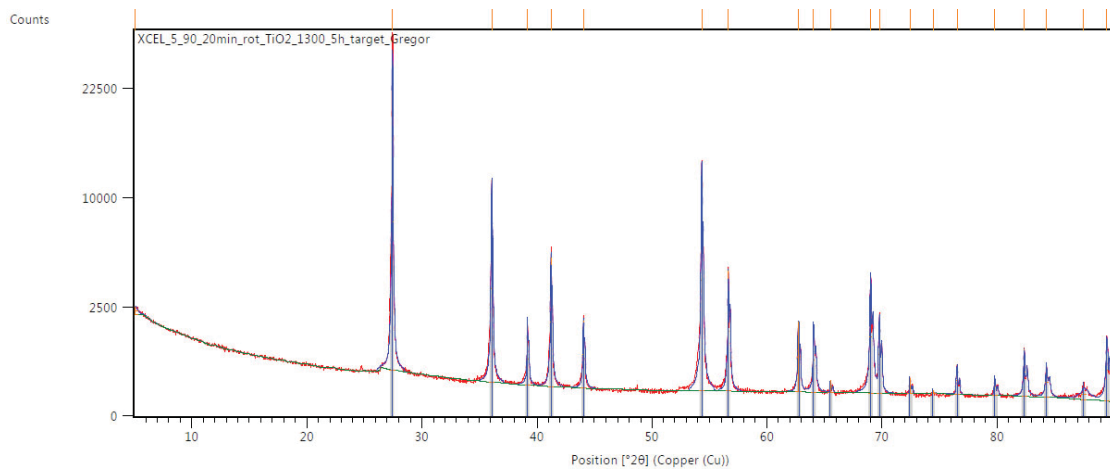


Figure 2.18: Diffractogram of the rutile target pellet compared to a database diffractogram (rutile, blue lines, PDF 01-076-1938). No other phases than rutile can be observed.

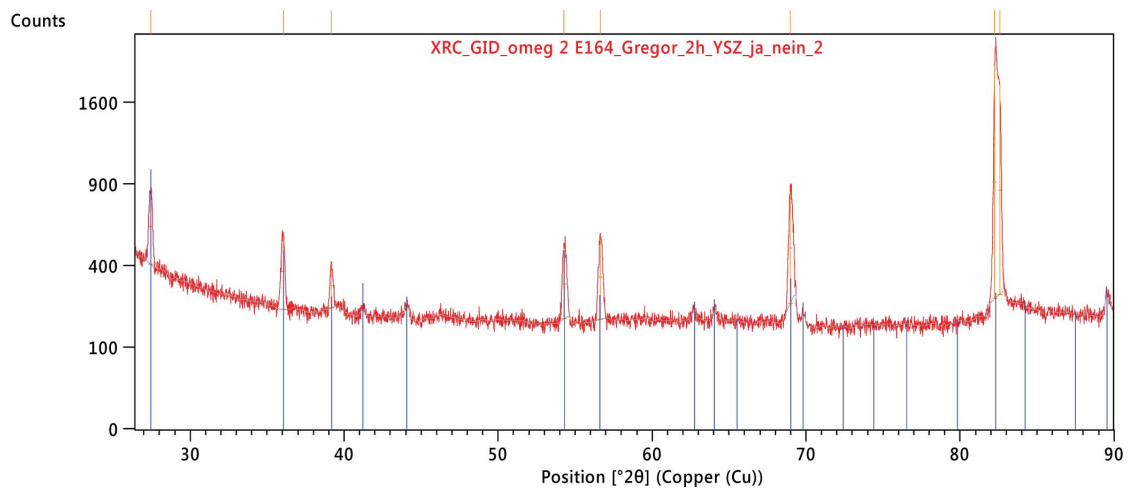


Figure 2.19: Grazing incidence X-ray diffraction pattern of a TiO₂ thin film on YSZ (100) (sample YSZ_TiO2_PLD_001). Comparison with the rutile database pattern (PDF 04-003-0648, blue lines) shows that only the rutile phase is present.

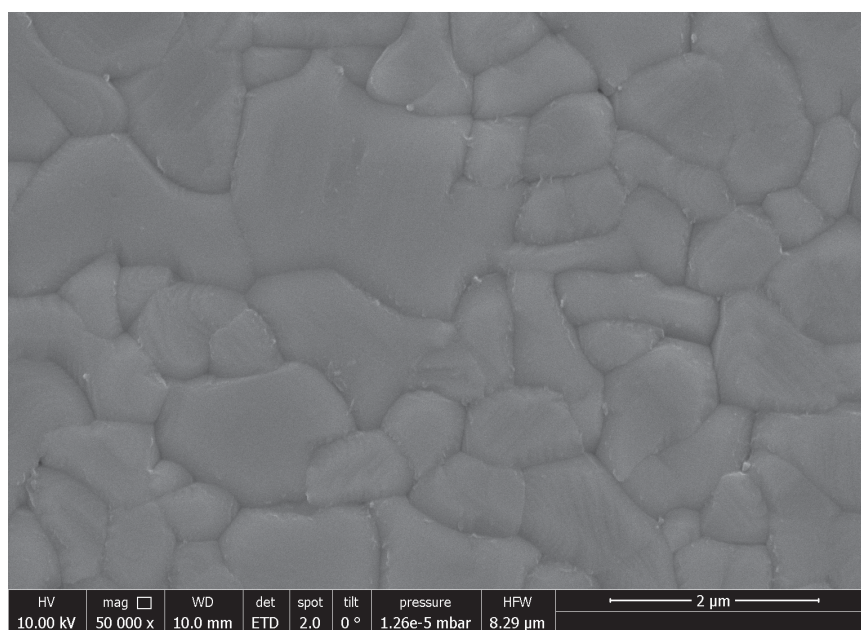


Figure 2.20: SEM micrograph of the titania layer on sample YSZ_TiO2_PLD_001, top view. A dense layer and grains in the micrometer size are visible.

In contrast to this, on sample YSZ_TiO2_PLD_XRD_002, which was produced according to the same procedure as sample YSZ_TiO2_PLD_001, rutile reflections can be found in the XRD pattern but there are two unknown peaks that have comparable intensity to the rutile peaks (see figure 2.21). The preparation procedure of sample YSZ_TiO2_PLD_XRD_001 differed from the other two samples only in deposition time. The grazing incidence diffraction pattern shows no rutile or anatase reflections, of the three peaks present two could stem from an orthorhombic high temperature titania phase (see figure 2.22), although the origin of this phase is unknown. The non-reproducible phase composition of the titania thin films raises the question in what other ways the samples might differ.

All PLD settings (except the deposition time for YSZ_TiO2_PLD_XRD_001) were the same. In spite of this, the temperature varied in an interval of 15°C (see table 2.5), which is within the usual accuracy achievable on this instrument. However, this is not expected to have an influence on the crystal structure because higher temperature should only lead to higher mobility of the cations and facilitate the arrangement into a thermodynamically stable compound.

A common observation on many samples deposited on the PLD apparatus used in this work is the appearance of ring-shaped colourful structures, visible to the naked eye. These could be light interference effects caused by inhomogeneous film thickness. This phenomenon was observed on samples YSZ_TiO2_XRD_002 and YSZ_TiO2_XRD_001, but not on sample YSZ_TiO2_PLD_001. If this inhomogeneity can cause either different structure or artefacts in the XRD measurement should be the subject of future investigations.

Deposition of doped rutile In literature several reports on the production of 1-6% Cr-doped rutile by a simple solid state reaction can be found [115–118]. On the one hand,

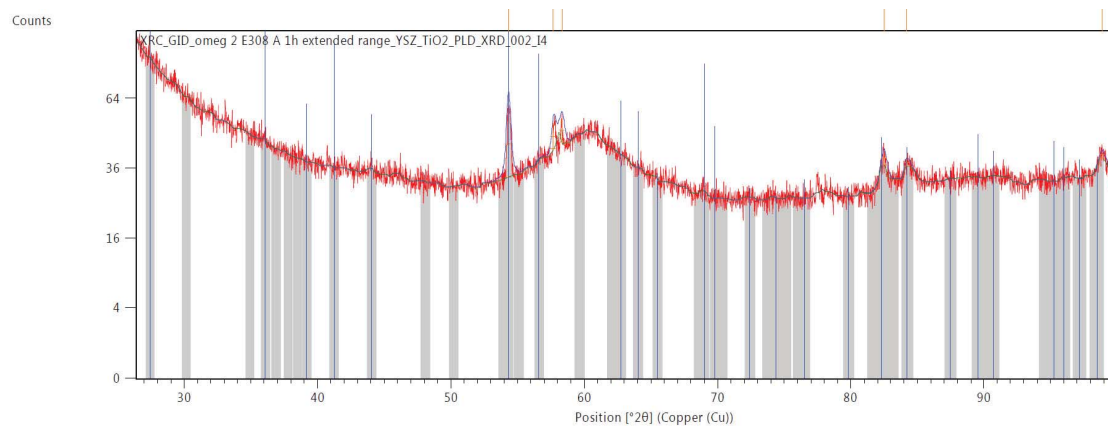


Figure 2.21: Grazing incidence X-ray diffraction pattern of sample YSZ.TiO₂.PLD.XRD.002 compared to database reflection positions of rutile (PDF 04-003-0648, blue lines), anatase (PDF 00-004-0477, green lines) and YSZ (6 mol% Y₂O₃, PDF 04-018-5452). Some peaks can be identified as originating from rutile but there are two unidentified peaks at around $2\Theta = 58^\circ$.

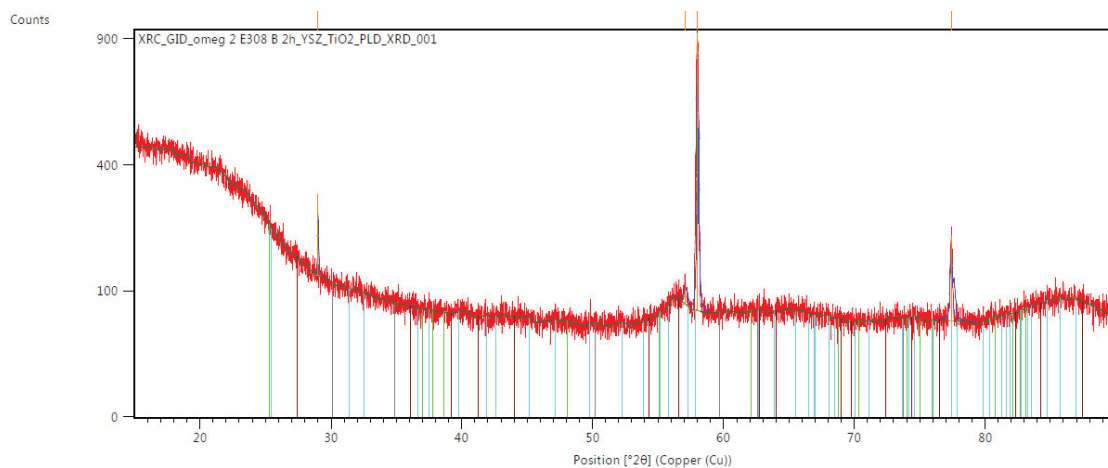


Figure 2.22: Grazing incidence X-ray diffraction pattern of sample YSZ.TiO₂.PLD.XRD.001 compared to database reflection positions of anatase (PDF 00-021-1272, light green lines), rutile (PDF 04-003-0648, brown lines), YSZ (6 mol% Y₂O₃, PDF 04-018-5452, grey lines) and an orthorhombic high pressure TiO₂ phase (PDF 04-014-5355, light blue lines).

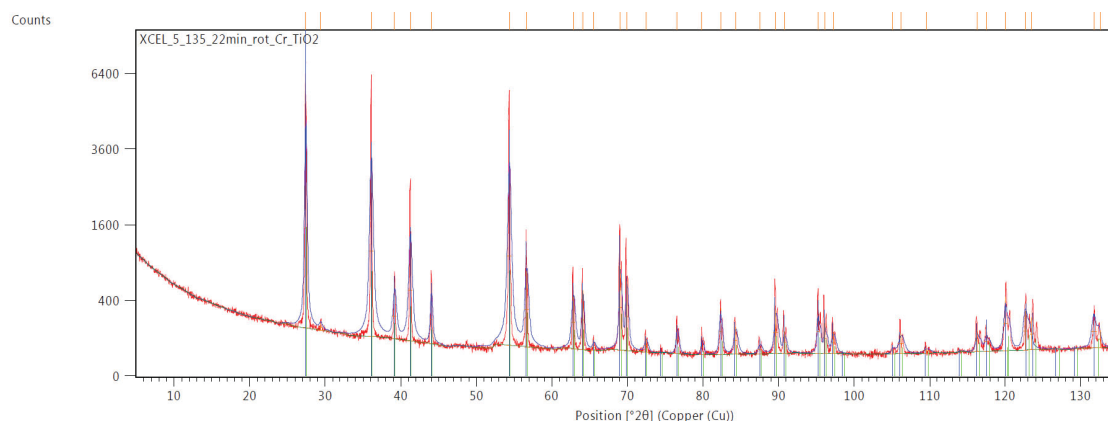


Figure 2.23: XRD pattern of the Cr-doped rutile pellet, compared with a database pattern of $\text{Ti}_{0.97}\text{Cr}_{0.03}\text{O}_2$ (PDF 04-015-2312, green lines) and TiO_2 (PDF 04-003-0648, blue lines). The only non-rutile reflection can be found at approximately $2\Theta = 29^\circ$.

the synthesis seemed to be straightforward but on the other hand, no X-ray diffraction patterns were included in any of the cited papers to confirm phase purity.

In [115] the samples were prepared by mixing TiO_2 and $\text{Cr}(\text{NO}_3)_3$ powder followed by isostatic pressing under 2000 bar for 1 h. It can be assumed that sintering took place during the measurements at 1000°C .

The authors of [117] refer to the method of [116], who sintered mixtures of TiO_2 and Cr_2O_3 powders for 10 h at 1420 K.

Also in [118] mixtures of TiO_2 and Cr_2O_3 powders were sintered but no further comment on the conditions was given.

In the present study the synthesis of 3% Cr-doped rutile ($\text{Ti}_{0.97}\text{Cr}_{0.03}\text{O}_{2-\delta}$) was tried. 2.0338 g TiO_2 (Alfa Aesar, 99.99% metals basis purity) was mixed with 0.0620 g Cr_2O_3 (Sigma Aldrich, $\geq 99\%$ purity), then cold isostatically pressed (approximately 3000 bar, 20 s) and subsequently sintered at 1300°C for 72 h. An X-ray diffractogram was recorded on the same setup as for the pure rutile target, it is presented in figure 2.23. Comparison with a database diffractogram shows that all reflections but one, at $2\Theta = 29.3774^\circ$, can be attributed to a compound having rutile structure. Since TiO_2 and $\text{Ti}_{0.97}\text{Cr}_{0.03}\text{O}_2$ have very similar diffraction patterns with the peak positions additionally depending on the amount of oxygen vacancies, further analysis would be necessary in order to find out whether or not Cr was successfully inserted into the TiO_2 lattice.

As far as the unknown peak is concerned, it is remarkable that this peak has an intensity of 2.67% of the highest peak in the pattern. This value is close to the nominal dopant content of 3%. A possible explanation for this similarity is that the small peak is in fact the strongest reflection coming from a second phase which contains large parts of the dopant. An observation which gives further hints about the nature of the unidentified phase is the fact that the pill is weakly magnetic (see figure 2.24). CrO_2 is a candidate material to unite the above observations: It is a magnetic Cr compound [55, p. 1572] and it shows an X-ray reflection at $2\Theta = 28.526^\circ$, which is about 0.85° left of the observed peak. However, this deviation cannot be explained. Furthermore, the fact that according to literature it decomposes at temperatures above 200°C [55, p. 1572] is puzzling.

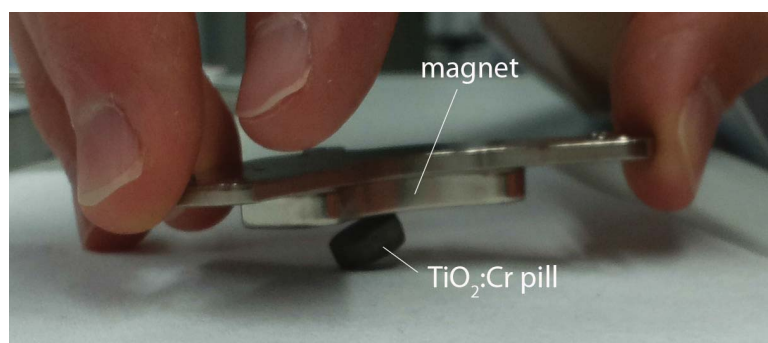


Figure 2.24: The product of the attempted synthesis of 3% Cr-doped TiO_2 (dark pill) is attracted by a magnet.

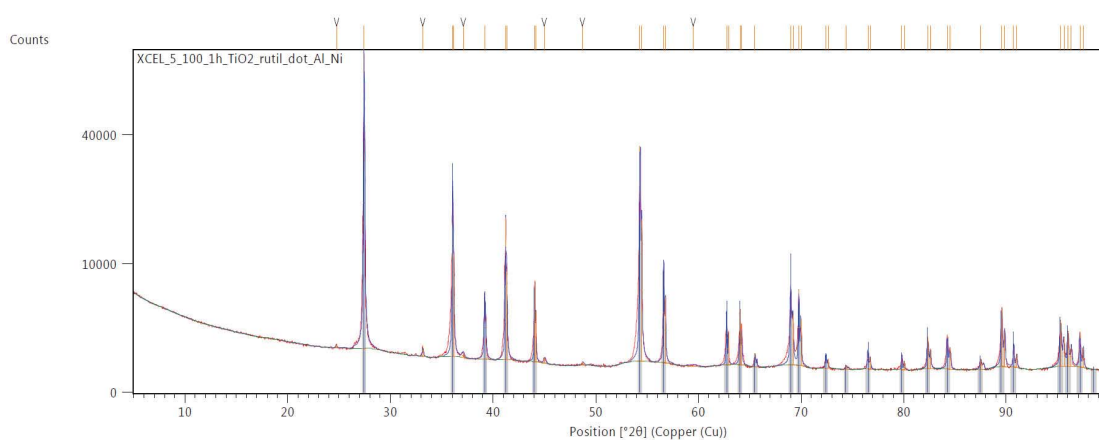


Figure 2.25: X-ray diffraction pattern of the synthesis product of the $\text{Ti}_{0.98}\text{Ni}_{0.01}\text{Al}_{0.01}\text{O}_{2-\delta}$ synthesis compared to a rutile database pattern (PDF 04-003-0648, blue lines). There are several unexplained reflections, marked by the black arrow tips on the upper edge of the image.

Provided, however, that CrO_2 formed on cooling and that the target temperature in the PLD does not exceed the decomposition temperature, this magnetic phase could still be present.

A second attempt of doping rutile *via* a solid state reaction was made. The aim was to produce the co-doped compound $\text{Ti}_{0.98}\text{Ni}_{0.01}\text{Al}_{0.01}\text{O}_{2-\delta}$ by mixing and grinding 0.0158 g Ni powder (Riedel de Haën, 99.8% purity), 0.0132 g Al_2O_3 (Sigma Aldrich, purity 99.998%) and 2.0607 g TiO_2 (Aldrich, 99.99% trace metals basis purity). The mixture was cold isostatically pressed (approximately 3000 bar, 20 s) followed by a sintering step (1300°C, 65 h). An X-ray diffraction pattern (setup as for the pure rutile target) is shown in figure 2.25. There are several unexplained peaks and so it is assumed that doping was (partially) unsuccessful. Then, a thin film was deposited by PLD using this target (sample named YSZ_NATO11.001; same deposition parameters as for sample YSZ_TiO2_PLD.001). The grazing incidence XRD pattern revealed the rutile structure of this layer (see figure 2.26). Also, an SEM micrograph of the thin film surface was recorded (figure 2.27). Grains in the micrometer range are visible, confirming again the crystalline nature of the film. However, there are segregations present on the sur-

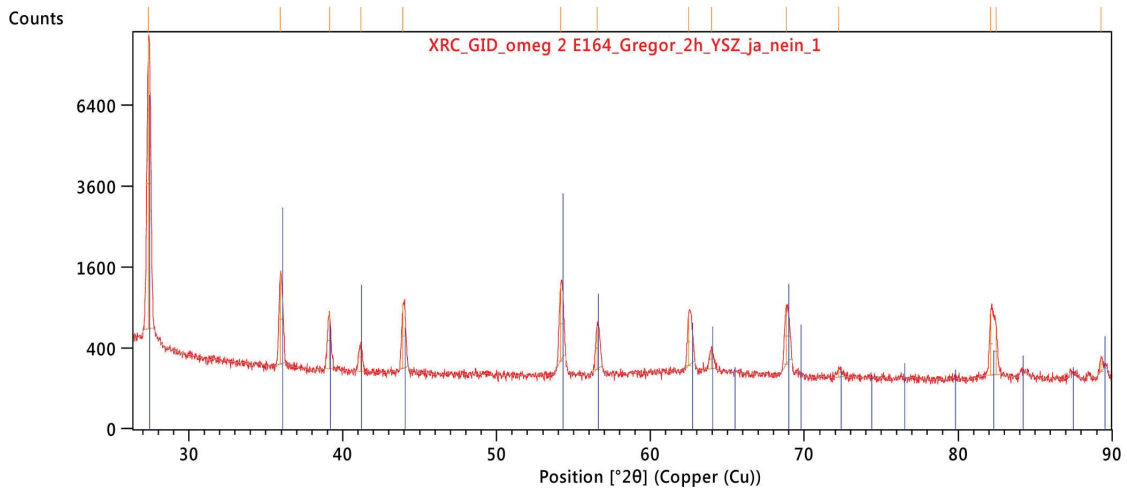


Figure 2.26: X-ray diffraction pattern of sample YSZ_NATO11.001 (Ni and Al-doped TiO_2). Comparison with the database pattern for rutile (PDF 004-003-0648) shows good agreement.

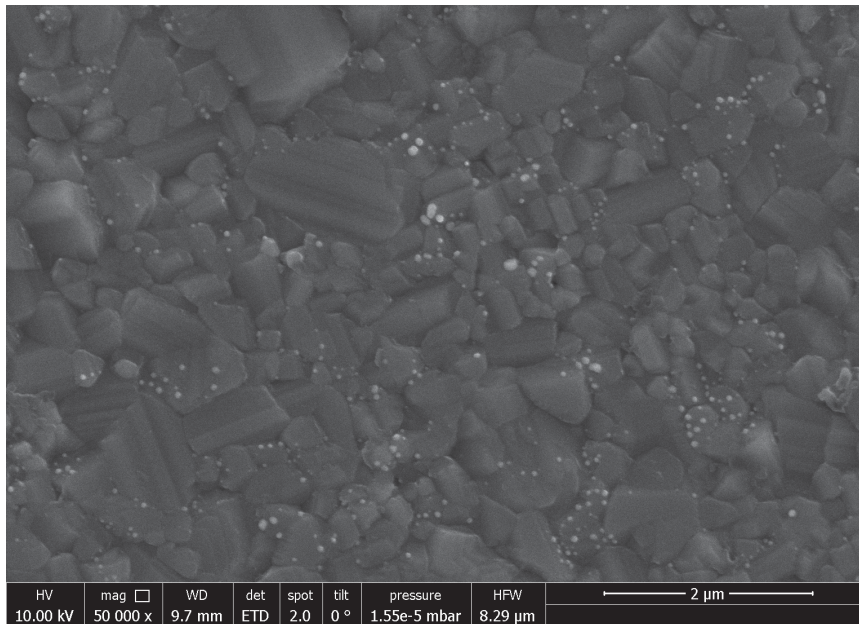


Figure 2.27: SEM micrograph of sample YSZ_NATO11.001, an attempt to produce a Ni and Al-doped rutile thin film on YSZ. Clearly, micrometer-sized grains and segregations are visible.

face, which is not the case for the undoped rutile thin film deposited by PLD (sample YSZ_TiO2_PLD_001). Considering the unidentified reflections in the XRD pattern of the PLD target these particles can be interpreted as another hint that doping with Al and Ni was not successful: The dopant elements probably accumulated on the surface instead of being integrated into the host lattice.

Summary of deposition of TiO₂ by PLD Pure rutile could be successfully deposited by PLD once, but couldn't be reproduced. Doping rutile with 3% Cr by a "shake and bake" synthesis was reported to be successfully performed in literature, but was not confirmed in this work. A new combination of dopants for rutile was tried out, the result are multiple phases.

Summary of TiO₂ deposition

The goal of the titania deposition experiments was to reproducibly deposit TiO₂ layers which are stable during a few measurements. Rutile could be produced by thermally oxidising a layer sputtered from a Ti target, but pre-sputtering for more than 75 min and a separate shutter for the sample were necessary, making this process rather inconvenient.

PLD of pure rutile was successful once but irreproducible, the preparation of phase-pure doped rutile targets by solid state reaction was not successful, even though Cr-doping by this method was reported in literature.

While rutile was complicated to obtain by sputtering, anatase formed readily, even with different annealing procedures. As mentioned in subsection 2.1.2, there was an unexplained reflection in many X-ray patterns of samples annealed for 2 h at 550°C. Also the treatment at 900°C for 2 h yielded anatase, but there were also unexplained peaks in the XRD patterns. However, the deposition of this substance(s) was reproducible: This was shown for the 2 h/900°C-method for 2 samples on quartz glass, 2 samples on YSZ, for the 2 h/550°C-method for 8 samples on YSZ.

In order to assess the stability of the anatase thin film during a series of measurements samples YSZ_TiO2_Ana2-900_XRD_001 (annealed 2 h at 900°C) and YSZ_TiO2_Ana_XRD_001 (annealed 2 h at 550°C) were fired for 99 h at 500°C in air, which corresponds to typical, prolonged measurement conditions. X-ray patterns of the samples after annealing are shown in fig 2.28 (sample YSZ_TiO2_Ana2-900_XRD_001) and 2.29 (sample YSZ_TiO2_Ana_XRD_001). The heat treatment does not change the sample which was produced *via* the 2 h/550°C-way, but the 2 h/900°C-sample shows unexplained reflections. This does not necessarily mean that the sample has changed. Several XRD measurements on the same sample have shown that the intensity of these unknown peaks, especially the one which appears at $2\Theta \approx 77^\circ$ depends on the orientation of the sample in the diffractometer. Therefore, if only one orientation was probed, it can be assumed that this reflection might have appeared in another orientation and that the phase causing it is present anyway. The appearance of unexplained XRD peaks is acceptable because it seems to be reproducible. This type of sample can still be used for electrochemical measurements since the only requirements are reproducibility, stability and electrochemical effects worth studying, all of which were given. One cannot speak of "anatase samples", though. Rather, they are "samples containing mainly anatase and and unknown phase".

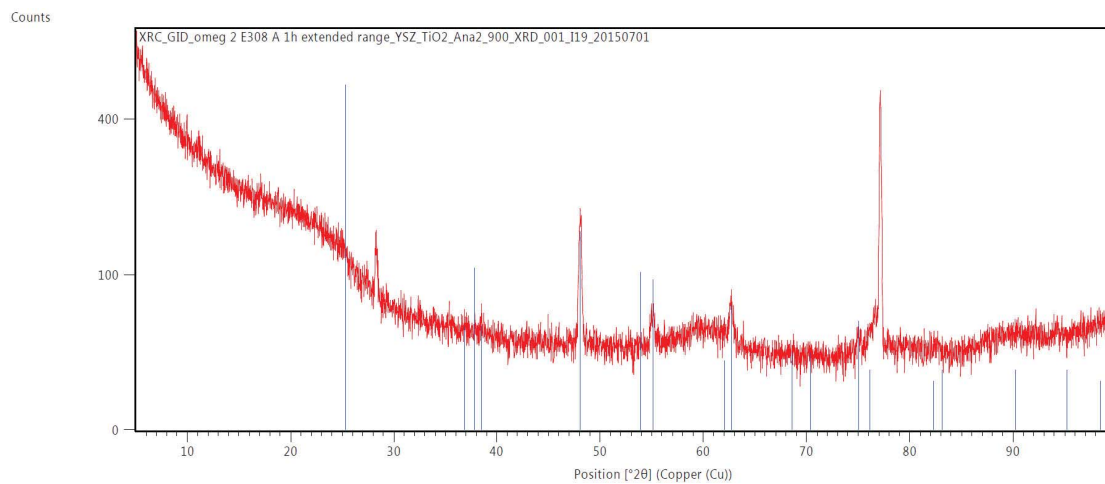


Figure 2.28: X-ray diffractogram of sample YSZ_TiO2_Ana2-900_XRD_001 after firing for 99 h at 500°C, compared to PDF 00-004-0477 (anatase, blue lines). There are unexplained peak, the intensity of one of them is comparable to the highest anatase reflection.

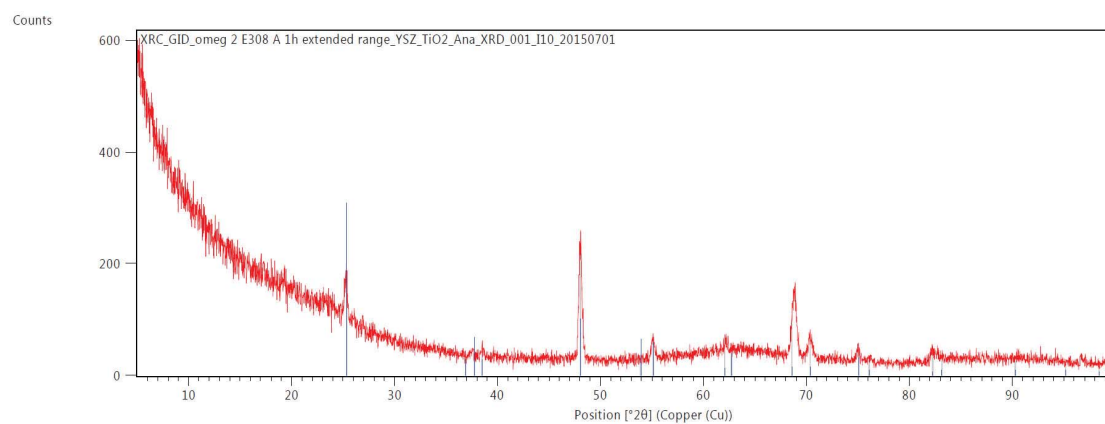


Figure 2.29: X-ray diffractogram of sample YSZ_TiO2_Ana_XRD_001_I10 after firing for 99 h at 500°C compared to PDF 00-004-0477 (anatase, blue lines). Only anatase reflections are visible.

Therefore, sputtering of Ti followed by one of these two annealing programmes was used to produce the samples for the electrochemical measurements.

Table 2.6 gives an overview of nominal and approximate real layer thicknesses of all TiO₂ samples used in this work. For several samples a “control sample” was prepared along with the electrochemically measured samples, which was coated in the same sputtering procedure. On some of these “control samples” the thickness of the titania layer was determined by SEM. In the table these values are given. It is also indicated which of these samples correspond to which electrochemically measured samples. Parts of the data were already presented in table 2.4 but are listed again for better comparability.

Table 2.6: Overview of titania layer thicknesses of all samples presented in this work. . . . plasma went out several times, no sputtering time can be given

sample name	$d_{\text{nominal}}/\text{nm}$	t_{sput}/s	d_{QCM}/nm	$r_{\text{sput}}/\text{nm s}^{-1}$	control sample	d_{SEM}
Quarz_Ti	80	600	no QCM	-	none	-
Quarz_Ti_002	100	750	no QCM	-	none	-
Quarz_Ti_004	200	2997	155	0.08...0.1	none	-
Quarz_Ti_008	100	1540	200	0.12...0.15	none	-
SZ.001_003a	100	750	no QCM	-	none	-
YSZ.001a, b, _002, _004a1, _004a2	20	150	no QCM	-	none	-
YSZ_Ti-Pt-Kreise_004, 005, 006	100	750	no QCM	-	none	-
LSC64-TiO2_001, _002c, d	100	750	no QCM	-	none	-
YSZ.poly_6	20	150	no QCM	-	none	-
YSZ.poly_7, 8	100	750	no QCM	-	none	-
LSC64-TiO2.Hutetc.001, 002	100	750	no QCM	-	none	-
YSZ.TiO2-Pt.Ana2-900.001	100	1528	95.5	0.07	none	-
YSZ.TiO2-Pt.Ana2-900.002	100	?	?	?	none	-
YSZ.TiO2-Pt.Ana2-900.004	100	1149	100	0.05...0.07	YSZ_TiO2_Ana2-900_XRD_003	-
YSZ.TiO2-Pt.Ana2-550.001b	100	1520	79.3	floating	YSZ_TiO2_Ana2-900_XRD_001	-
YSZ.TiO2-Ag_Ana2-550.002	100	1556	100.5	0.07	YSZ_TiO2_Ana2-550_XRD_007	-
YSZ.TiO2-Ag_Ana2-550.001	100	1862	100.6	0.07	YSZ_TiO2_Ana2-550_XRD_006	-
YSZ.TiO2-Pt.Ana2-550.004, 005	100	1740	100.1	0.07	YSZ_TiO2_Ana2-550_XRD_003	116
YSZ.TiO2-Au_Ana2-550.001	100	1740	100.1	0.07	YSZ_TiO2_Ana2-550_XRD_003	116
YSZ.TiO2-Pt.Ana2-550.006	100	1920	100.5	0.07	none	-
YSZ.TiO2-Pt.Ana2-550.009	100	*	100.3	0.05...0.08	YSZ_TiO2_Ana2-550_XRD_004	113.5
YSZ.TiO2-Au_Ana2-550.004, 005	100	*	100.3	0.05...0.08	YSZ_TiO2_Ana2-550_XRD_004	113.5
YSZ.TiO2-Au_Ana2-550.005	100	1853	100.2	0.05...0.08	YSZ_TiO2_Ana2-550_XRD_005	-
YSZ.TiO2-Pt.Ana2-550.010	100	1853	100.2	0.05...0.08	YSZ_TiO2_Ana2-550_XRD_005	129.5
YSZ.TiO2-Pt.Ana2-550.011	100	1684	100.4	0.05...0.08	YSZ_TiO2_Ana2-550_XRD_008	-
YSZ.TiO2-Pt.Ana2-550.012	100	1799	≈ 108	0.05...0.07	YSZ_TiO2_Ana2-550_XRD_009	-

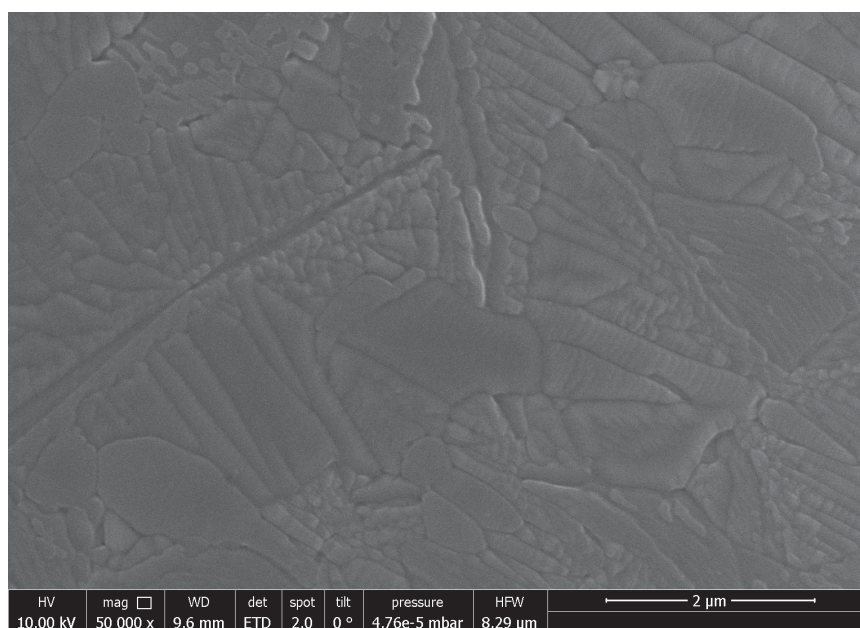


Figure 2.30: SEM micrograph of sample YSZ_TiO₂_Ana2-900_XRD.003's titania thin film surface showing a dense layer with micrometer-sized grains.

From this table it can be seen that most samples with a nominal thickness of 100 nm were produced by sputtering 750 s without QCM or around 1800 s with QCM. Assuming a similar sputtering rate the first group of samples has an approximate layer thickness of $750 \cdot 0.07 = 52.5$ nm. The SEM micrographs, which are the most reliable of the used methods to determine the film thickness, show that the layers are roughly 10% thicker than expected from the QCM measurement. Therefore, most of the samples can be assumed to have a titania film thickness of around 60 or 110 nm.

On one sample, YSZ_TiO₂_Ana2-900_XRD.003 (produced by sputtering and subsequent annealing at 900°C for 2 h in air) an SEM micrograph of the titania surface was recorded (figure 2.30). The film has microcrystalline structure and is dense.

Different types of TiO₂-samples

The titania thin films obtained by these two preparation procedures were deposited on $5 \times 5 \times 0.5$ mm³ YSZ single crystals (Crystec, Germany) and on polycrystalline YSZ disks with a diameter of roughly 1 cm. For the polycrystalline substrates 8 mol% yttria doped zirconia powder (Tosoh, Japan) was pressed and subsequently sintered at 1550°C for 5 h (see [119, p. 10], [120, p. 11]). The thin films were microstructured into various shapes by standard photolithography and subsequent ion beam etching or by lift-off photolithography. Current collector metals (Pt, Au) were deposited by sputtering and microstructured in the same way (see subsection 2.1.1). For an overview of the used cell geometries see figure 2.31. Figure 2.32 shows an optical microscope image of sample YSZ_Ti-Pt-Kreise.005 to illustrate the real appearance of some of the electrodes.

For samples LSC64-TiO₂_Hutetc.001, and -.002, LSC64-TiO₂.001.c and

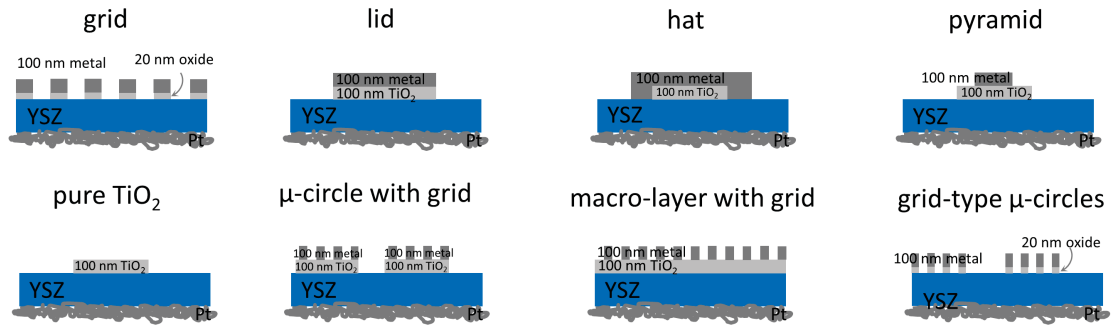


Figure 2.31: Overview of cell geometries.

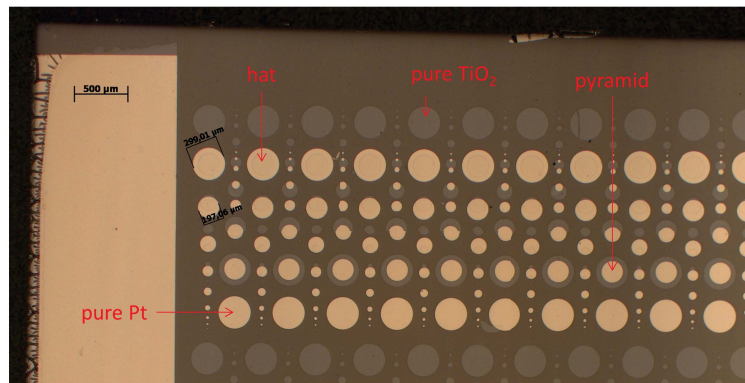


Figure 2.32: Microscope image of different electrodes on sample YSZ_Ti-Pt-Kreise_005.

LSC64-TiO₂.003_a and -b La_{0.6}Sr_{0.4}CoO_{3-δ} (LSC) was used as a current collector instead of a metal. The LSC target prepared in [114] was used. The PLD parameters from [114] were slightly adapted and are given in table 2.7. The counter electrode was porous Pt paste (see subsection 2.1.1).

Table 2.7: PLD parameters for deposition of La_{0.6}Sr_{0.4}CoO_{3-δ} [114]

parameter	value
laser	KrF, $\lambda = 248 \text{ nm}$
fluence at target/ J cm^{-2}	1.5
laser pulse rate/Hz	5
target	LSC
substrate	YSZ (100)
substrate temperature/ $^{\circ}\text{C}$	550
distance target-furnace/cm	6
intended film thickness /nm	100
deposition time/s	610
O ₂ pressure/mbar	4×10^{-2}

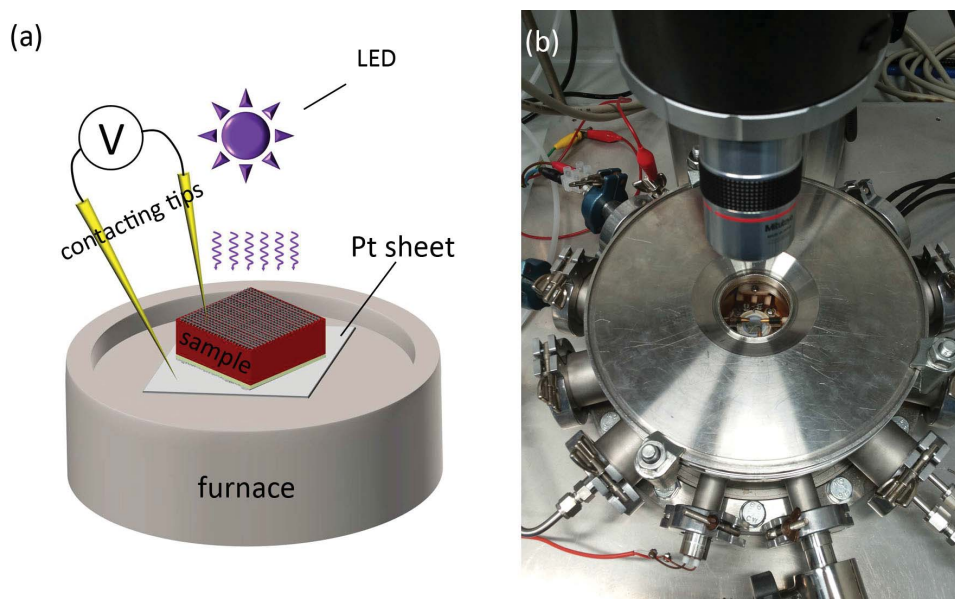


Figure 2.33: Measurement setup. (a) Sketch showing an STO sample in the measurement setup, the voltmeter symbolises an electrochemical measurement. (b) Photograph of the setup, without lamp.

2.2 Measurement setup

For the electrochemical measurements a micro-contact heating stage was used (figure 2.33). This apparatus is described in detail elsewhere [121]. The oxygen partial pressure could be changed by filling the apparatus with different gas mixtures. Using N_2 or Ar (Air Liquide Alphagaz 1, O_2 impurity ≤ 2 ppm) a $p(O_2)$ of approximately 10 ppm is assumed due to leakage in the gas pipe system. A reducing atmosphere was created with moistened hydrogen gas: 2.5 % H_2 in Ar (Air Liquide Arcal 10) was bubbled through a gas washing bottle filled with deionized water at room temperature. Equilibrium between H_2 , O_2 and H_2O was assumed to be established at the measurement temperature. The contacting tips were gold-plated steel acupuncture needles of type “EGON” and “Blum Diamant”. For voltage measurements Keithley 2000 or Keithley 616 voltmeters were used. Electrochemical impedance spectroscopy (EIS) was usually performed with an Alpha-A High Performance Frequency Analyzer (Novocontrol Technologies, Germany) with a ZG-2, ZG-4 or POT/GAL interface, except for sample STO_002_b, where an HP 4192A Impedance Analyzer was preferred for its high measurement speed. AC voltage amplitudes were usually 10 mV (RMS), and only sometimes increased to 20 mV (RMS) when necessary. DC measurements were carried out on a Novocontrol Alpha A with the POT/GAL interface or alternatively on a Keithley PA 6487 picoammperemeter with voltage source.

Light-emitting diodes (LEDs) were mounted above the sapphire window. Two types of LEDs were used: a red one (Led Engin LZ4-00R300; 740 nm, 6.3 W electric power) and a blue one (Led Engin LZ4-00U600; 365 nm, 11 W electric power). The distance from sample to LED was roughly 2.4 cm. Methods for the calculation of the intensity of both LEDs from the data sheet as well as an in-depth measurement of the intensity and its

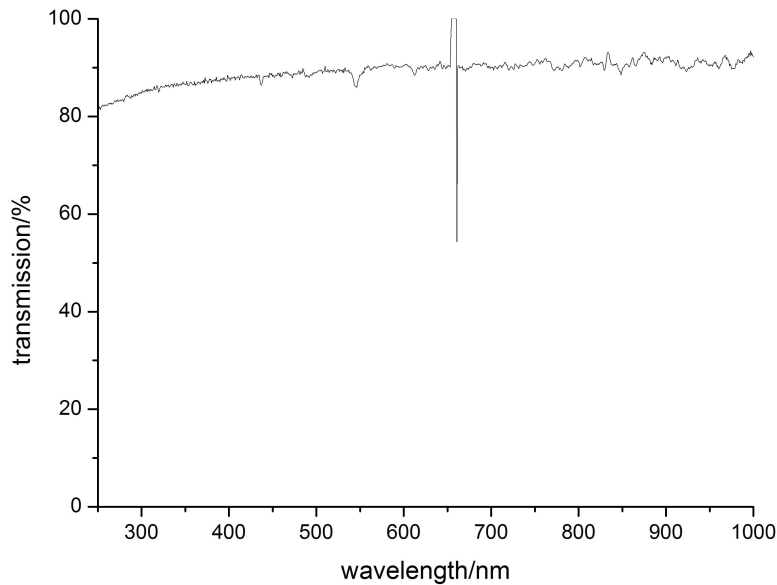


Figure 2.34: Transmission spectrum of the micro-contact measurement setup’s sapphire window. It is almost completely transparent down to wavelenghts in the ultraviolet range.

spectral distribution with a spectrometer and a host of light sensors was done in [122] and the data given in this work are taken from there. LEDs identical in type and similar in time used were characterized in [122], so the data can be applied also for the devices used in the present study.

For the 365 nm LED the analysis of the data sheet yields a power of around 60 mW cm^{-2} . In contrast to this, the measurement results suggest a value of 6.2 or 8.6 mW cm^{-2} (different data sets available).

The values for the 740 nm LED are about twice as high as for the 365 nm LED.

Thanks to the broad transparency range of the sapphire window in the measurement apparatus the power arriving at the sample is still 80-90% of the emitted value. This can be seen in the spectrum in figure 2.34, which was recorded with the spectrometer described in subsection 2.1.2, but for the present measurement the waveguides were held in place by hand.

Optical microscope images of the samples were recorded on a Zeiss Imager.M1m.

3 Results and Discussion

The results chapter is roughly divided into two parts. The first part, sections 3.1 and 3.2, aims at finding out if the materials of interest are responsible for any kind of light effect and if so, what the features of a typical response are. In the second part mostly systematic measurements are presented that should shed light on how the typical light effect depends on the characteristics of the sample (geometry, materials combination, . . .) and on measurement parameters such as oxygen partial pressure and temperature.

For any measurements that are compared to others it is required to either hold all parameters but one constant or to assume that the effect of changing a certain parameter is negligible. While the experiments in the second part hold as many parameters as possible constant and make few negligibility assumptions, the opposite is the case for the rough measurements in the first part. There, the samples sometimes have only very few features in common, while the differing properties, that are assumed to have little effect on the interpretation, are numerous. This allows more samples to be included into the first overview and at the same time makes the comparison more meaningful. If a common light response can be found on those samples despite their differences this effect is general and not limited to very special conditions. In contrast to this, the second part takes advantage of the very similar samples from which more detailed information about the effects of light can be obtained.

3.1 Is there a light effect on titania?

3.1.1 Voltage vs. time measurements on titania compared to other materials

To find out whether light has any high temperature solid state electrochemical effect cells of type WE|YSZ|Pt were prepared with different geometries (WE. . . working electrode). The voltage U was measured as a function of time t between working and counter electrode while the sample was irradiated with blue (wavelength $\lambda = 365$ nm) and red ($\lambda = 740$ nm) light. While the blue light should be able to excite electrons over the band gap of TiO_2 (≈ 3.2 eV, corresponding to ≈ 387 nm for anatase [56]) the red light can not and only for blue light an effect is expected. Therefore, a sample is termed to show a light effect if there is a significant qualitative and quantitative difference in the voltage response following illumination with blue compared to red light.

A good example for a sample that shows no light effect is LSC64.001 (100 nm LSC on YSZ). The working electrode is a circular microelectrode with a diameter of 200 μm . The measured voltage as a function of time at 400°C set temperature (represented by the symbol T) is shown in figure 3.1. The voltage changes upon turning on the light are small and almost the same for blue and red light. An additional conclusion is that the Pt paste counter electrode, which is illuminated as well through the YSZ single crystal (cf. figure 3.2) is photoelectrochemically inactive. This is an important confirmation of our expectations.

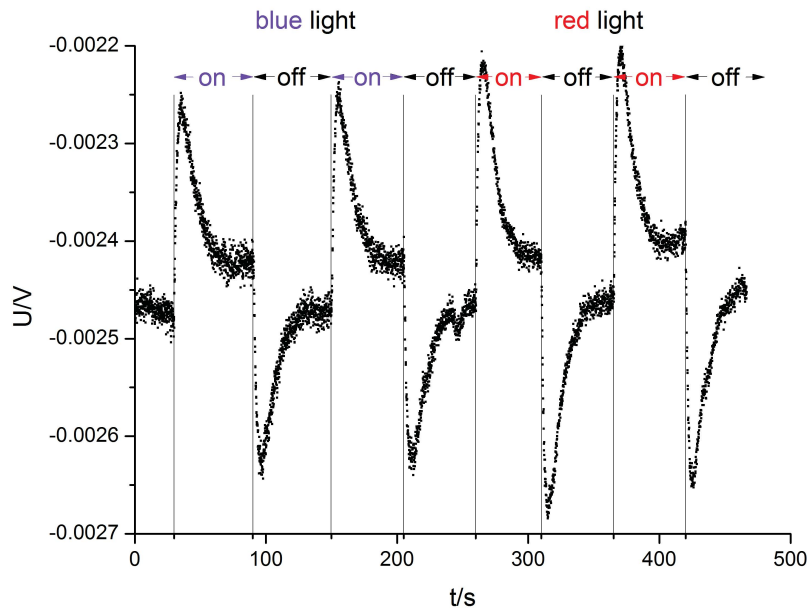


Figure 3.1: U vs. t curve for sample LSC64.001. Blue and red light cause similar, small changes in the voltage, so the response is decided to be no light effect.

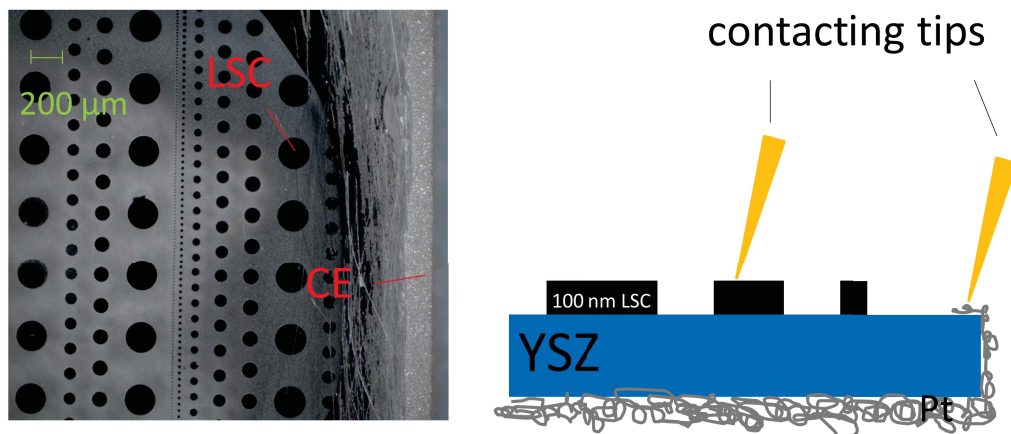


Figure 3.2: Microscope image (left) and sketch (right) of sample LSC64.001. In the left panel the dark dots are LSC thin film microelectrodes. Next to the LSC circles the Pt counter electrode can be seen through the YSZ single crystal.

Table 3.1: Samples with grid-type WEs and results of $U(t)$ measurements

sample name	material 1	material 2	$U(t)$ behaviour
YSZ.001a	20 nm TiO ₂	100 nm Pt	30 mV change with blue light
YSZ.001b	20 nm TiO ₂	100 nm Pt	60 mV change with blue light
YSZ.002	20 nm TiO ₂	100 nm Pt	30 mV change with blue light
YSZ.003b1	20 nm Cr	100 nm Pt	no effect
YSZ.003b2	20 nm Cr	100 nm Pt	no effect
YSZ.001c1			
YSZ.001c2	100 nm Pt	-	slow change of 20 mV with blue light
YSZ.001c3			
YSZ.003d	100 nm TiO ₂	-	100...300 mV with blue light, depending on read-out method
YSZ.004a1	20 nm TiO ₂	100 nm Au	3...10 mV change with blue light
YSZ.004a2	20 nm TiO ₂	100 nm Au	25...40 mV change with blue light
YSZ.004b1	20 nm Cr	100 nm Au	no effect
YSZ.004b2	20 nm Cr	100 nm Au	no effect
YSZ.004c1	100 nm Au	-	2 mV change with blue light
YSZ.004c2	100 nm Au	-	5 mV change with blue light
YSZ.poly_005	100 nm Pt	-	no effect
YSZ.poly_006	20 nm TiO ₂	100 nm Pt	20 mV change with blue light
YSZ.poly_007	100 nm TiO ₂	-	150 mV with blue light

The first series of samples to probe the light response of titania thin films has grid-shaped WEs consisting of one metal or two materials stacked one above the other (see figure 2.31, "grid"). Titania was not prepared as described in the experimental section (subsection 2.1.2) but was simply assumed to form from sputtered Ti during heating on the furnace in the sample holder. The assumption that titania is present even without a separate annealing step is supported by the hypotheses made on the sputtering process (initial sputtering of TiO₂ then Ti metal, see subsection 2.1.2, page 22). All measurements were carried out at 400°C set T in air.

Table 3.1 specifies the type of WE on each sample and lists the corresponding change in voltage caused by illumination. All samples have a WE geometry as sketched in figure 2.31 (grid) except for sample YSZ.002, where the grid was further microstructured into circles with a diameter of a few 100 μm .

The samples containing TiO₂ showed a light effect which was biggest on a pure TiO₂ WE grid (100...300 mV) but the measurements on this type of electrodes were extremely sensitive to interferences. The light effect occurred on single and polycrystalline YSZ substrates. It was bigger on a TiO₂/Pt WE (25...60 mV) than on TiO₂/Au (3...40 mV). Figure 3.3 shows a $U(t)$ curve for a titania grid WE on a single crystalline YSZ substrate. The effect of blue light can clearly be observed. Interestingly, also on pure Pt and Au WEs a light effect occurred. On Au WEs it was only a few mV but on Pt WEs a change of up to 20 mV occurred after switching on the blue light. However, the time behaviour was different than for the titania-containing samples. An example for such a $U(t)$ curve is shown in figure 3.4. On samples with a Cr/Au or a Cr/Pt grid no effect was observed. A representative measurement is shown in figure 3.5. It can be concluded from this first series of measurements that several materials (combinations) cause a light effect but it is biggest if TiO₂ is involved. The effect also seems to de-

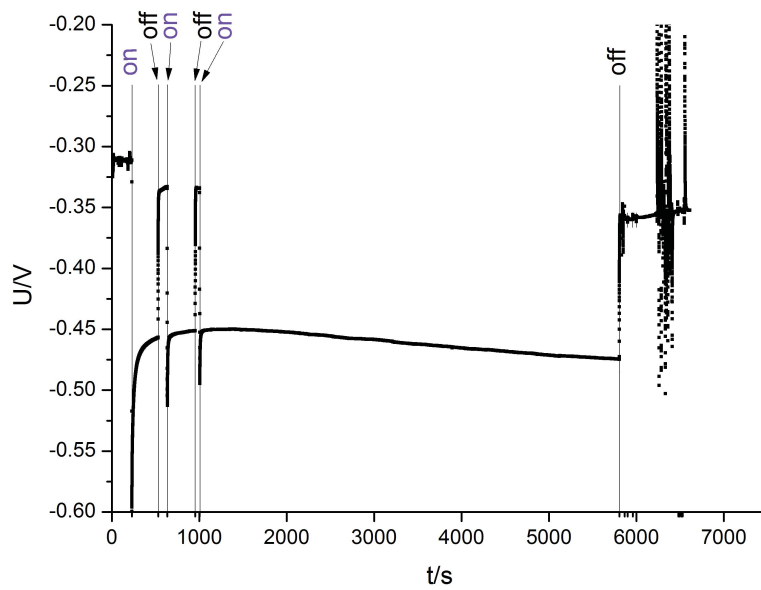


Figure 3.3: $U(t)$ curve for sample YSZ.003d (pure TiO_2 grid). The lines indicate when blue light was switched on and off. Irradiation with blue light leads to a change in voltage of >100 mV.

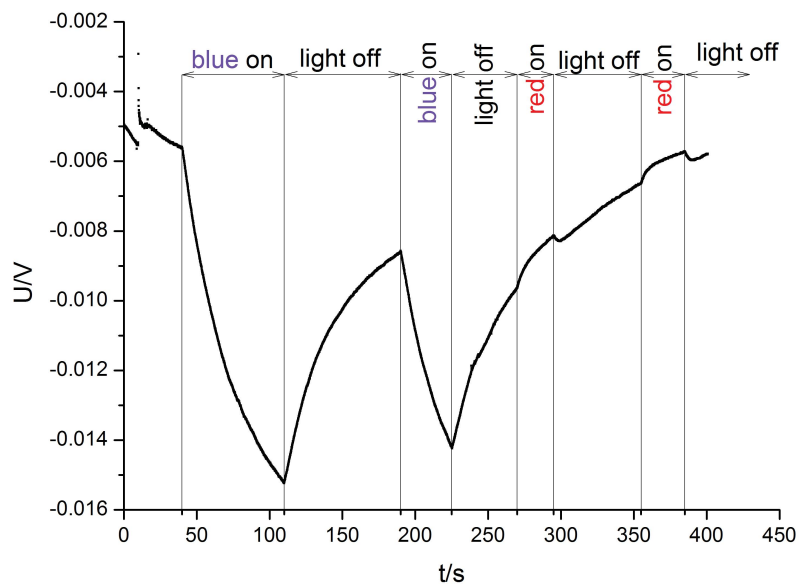


Figure 3.4: $U(t)$ curve for sample YSZ.003c3 (pure Pt grid). On this type of sample irradiation with blue light lead to a change in voltage of up to 20 mV. The time behaviour, however, is different from titania-containing samples.

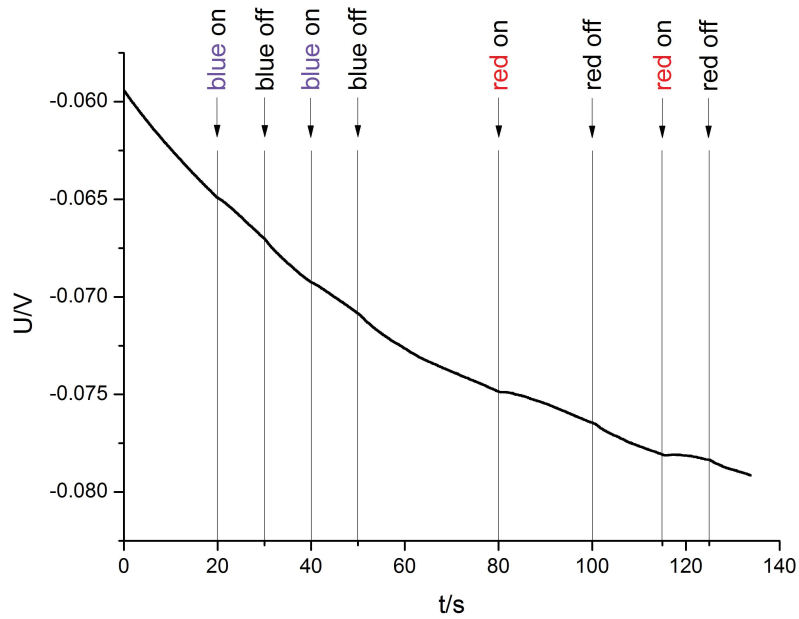


Figure 3.5: $U(t)$ curve for sample YSZ_003b2 (Cr/Pt grid). The response to irradiation with blue and red light is similar and very small, so this sample is defined to show no light effect.

pend on the other materials present and on the film thickness. Additionally, results on nominally identical samples vary, as can be seen on samples YSZ_004a1 and YSZ_004a2.

The second series of measurements was performed on samples with 100 nm thick Pt or TiO_2 circular WEs that were 300 μm in diameter (except for one electrode which was 75 μm in diameter). Samples YSZ_Ti-Pt-Kreise_004 and YSZ_poly_8 were sintered at 900°C for 2 h in air, sample YSZ_Ti-Pt-Kreise_005 was sintered at 1150°C for 10 h. For the elementary considerations on the light effect which are presented in this section this difference in preparation procedure will be neglected. The substrates were single and polycrystalline YSZ. Table 3.2 lists the measurement results.

Table 3.2: Samples with mostly 300 μm circular WEs and results of $U(t)$ measurements. s.c.... single crystalline, p.c.... polycrystalline

sample name	electrode name	substrate	WE material	$U(t)$ behaviour
YSZ_Ti-Pt-Kreise_004	Ti 1E	s.c. YSZ	TiO_2	150 mV change with blue light
YSZ_Ti-Pt-Kreise_005	Ti 2E	s.c. YSZ	TiO_2	100 mV change with blue light
YSZ_Ti-Pt-Kreise_005	Ti 2F	s.c. YSZ	TiO_2	150 mV change with blue light
YSZ_poly_8	Kreis Nr. 1	p.c. YSZ	TiO_2	300 mV change with blue light
YSZ_poly_8	Kreis Nr. 2	p.c. YSZ	TiO_2	75 mV with blue light
YSZ_poly_8	Kreis Nr. 3	p.c. YSZ	TiO_2	60 mV with blue light
YSZ_Ti-Pt-Kreise_004	75 μm	s.c. YSZ	Pt	no effect
YSZ_Ti-Pt-Kreise_005	Pt 1C	s.c. YSZ	Pt	no effect
YSZ_Ti-Pt-Kreise_005	Pt 1E	s.c. YSZ	Pt	no effect
YSZ_poly_8	Pt-Kreis	p.c. YSZ	Pt	<1 mV with blue light

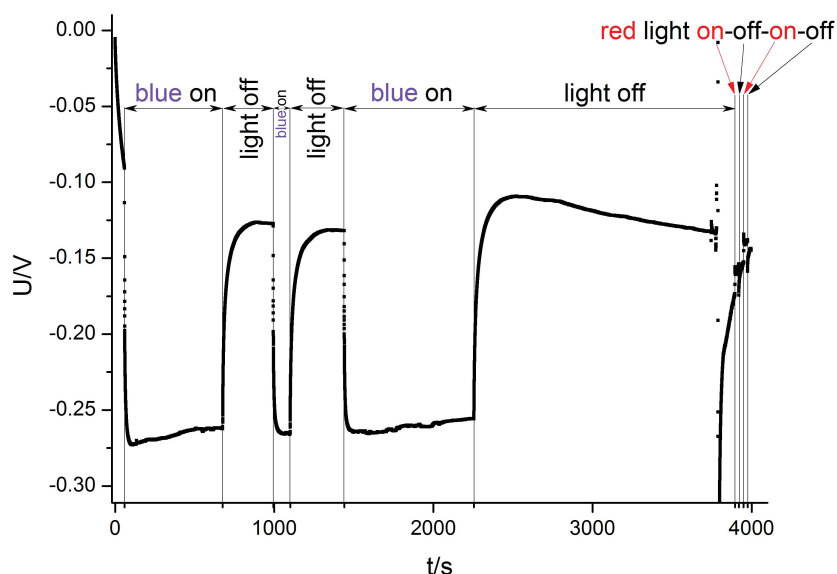


Figure 3.6: $U(t)$ curve for sample YSZ.Ti-Pt-Kreise.005, electrode 2F (pure TiO_2 circle). Voltage changes of about 150 mV upon irradiation with blue light can be observed whereas red light causes almost no change in voltage.

Samples with a TiO_2 WE respond to blue light by a voltage change of 60 to 300 mV, with a mean value of around 140 mV. An example for a $U(t)$ measurement is shown in figure 3.6. In contrast to this, samples with a Pt WE showed only a response to blue light of around 1 mV if at all. This set of measurements shows a strikingly clear difference between these two WE materials compared to the first series of measurements. This is attributed to the thicker TiO_2 films and the controlled Ti oxidation. Noisy measurements on pure titania WEs and strong variation of voltage changes measured on different microelectrodes on the same sample (see sample YSZ_poly.8) remained an issue.

3.1.2 Absorption of light in titania thin films

The experiments presented in the last subsection show that if TiO_2 is used as a working electrode a change in voltage results when blue light is turned on. In the present subsection it is explored how the TiO_2 layer is irradiated and how much light is absorbed.

How light reaches the titania layer

It is not immediately clear how light can reach the titania layer in samples with a hat- or grid-type geometry (see figure 2.31) because the thin film is covered by an intransparent metal layer. However, since the surface of the YSZ single crystal is not fully covered, light passes through the YSZ, is reflected at the counter electrode and finally reaches the TiO_2 layer from below. This works even when a circular TiO_2 microelectrode is completely covered by Pt, as will be shown in subsection 3.1.4. This situation

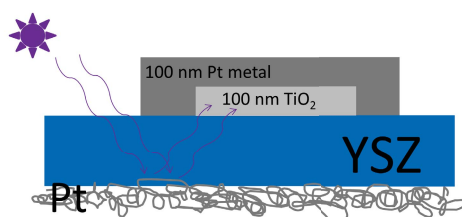


Figure 3.7: A TiO_2 microelectrode fully covered with Pt is illuminated from below by reflection of light at the counter electrode.

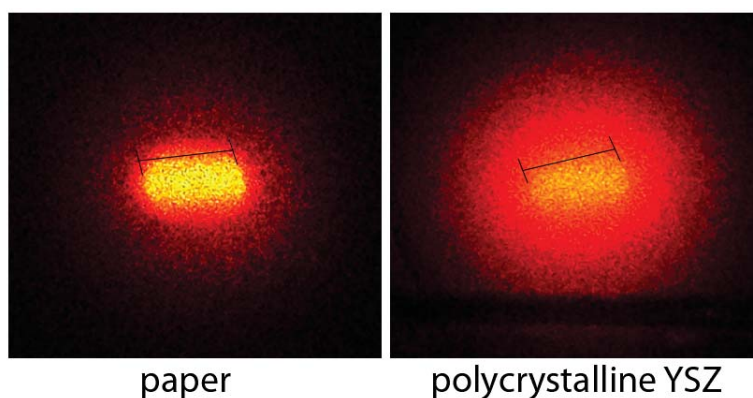


Figure 3.8: A laser spot on polycrystalline YSZ compared to paper. The black bar indicates the spot size of the laser (a few mm). Light is scattered strongly in YSZ.

is sketched in figure 3.7.

The effect of using a polycrystalline substrate on the irradiation conditions can be estimated by the experiment shown in figure 3.8 where a red laser beam hits a polycrystalline YSZ disk. Considerable intensity can be observed in a distance of more than half a millimeter next to the edge of the light spot. This can be explained by scattering of light at grain boundaries. Assuming that the scattered intensity is similar for other wavelengths light can still reach a covered TiO_2 microelectrode.

Optical spectroscopy

To check if the used titania thin films absorb the light emitted by the 365 nm LED optical transmission spectra of titania thin films on quartz glass were recorded. The spectroscopy equipment was the same as described in subsection 2.1.2 but a custom-built spectroscopy furnace was used as a sample holder/heater. This apparatus is described in detail in [122]. Figure 3.9 shows optical transmission spectra of six different samples. All samples consisted of a TiO_2 layer on quartz glass which was produced by sputtering of Ti and (often) subsequent thermal oxidation. The temperature at which the spectrum was recorded, the heat treatment and the sputtering time are indicated in the legend. If no heat treatment is given the thin film was only subject to the measurement temperature. Accordingly, e.g. sample SZ_003a, which was measured at room temperature, was not oxidised deliberately. Comparing the spectra of samples Quarz_Ti_002 and SZ_003a with Quarz_Ti_004, which differ by roughly a factor of four in sputtering time, we notice that there is a difference in transmission. However, it is

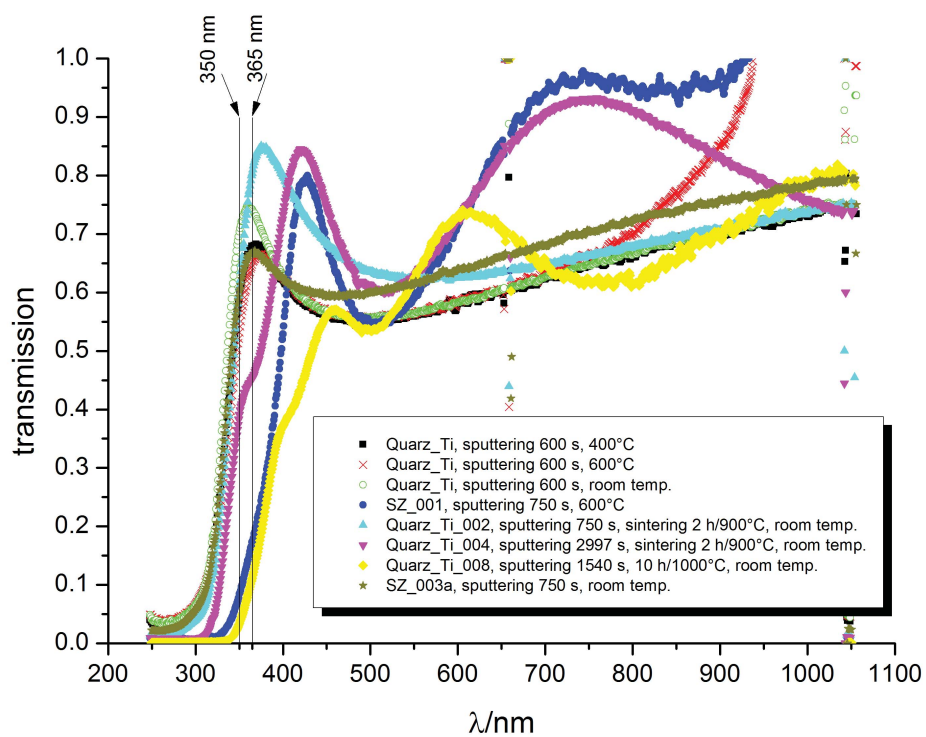


Figure 3.9: Optical transmission spectra of five different titania thin films on quartz glass. Samples differ in band gap energy.

not as big as could be expected from Lambert-Beer's law [123, p. 432]:

$$I = I_0 e^{-\alpha cd} \quad (3.1)$$

In this equation I , I_0 , α , c and d denote the light intensity after passing the sample, the initial light intensity, the absorption coefficient, the concentration of absorbing species and the sample thickness, respectively. Introducing the transmission T ,

$$T = \frac{I}{I_0}, \quad (3.2)$$

and comparing the transmission T_1 of a sample with thickness d with the transmission T_2 of a sample with thickness $4d$ we realize that

$$T_2 = e^{-\alpha c 4d} = \left(e^{-\alpha cd}\right)^4 = T_1^4. \quad (3.3)$$

For a transmission of approximately 0.6 at 350 nm an increase in film thickness by a factor of four should result in a transmission of $0.6^4 = 0.1296$. The measured transmission, however, is roughly 0.4, see figure 3.9.

A temperature dependence of the band gap is expected for two reasons:

- The lattice expands with increasing temperature, influencing the band structure.
- From the change in oxygen vacancy concentration an enlargement of the crystal lattice is expected because due to the missing oxide ions the repulsion between cations increases.

In contrast to this, the three spectra of sample Quarz.Ti, which were recorded at room temperature, 400°C and 600°C set T , are almost identical. This could be owed to little lattice expansion combined with slow equilibration kinetics (heating time was only about ten minutes).

Also, samples SZ_003a, Quarz.Ti and Quarz.Ti_004 show similar spectra even though the oxidation conditions for Ti were different. The Ti layer on SZ_003a was measured as deposited (without heat treatment), Quarz.Ti was oxidised in the spectroscopy furnace for around 10 min at 600°C set T and Quarz.Ti_004 was subject to 2 h at 900°C in air. From this observation it can be concluded that already directly after deposition TiO_2 is present instead of metallic Ti. This is in agreement with the hypothesis put forward in subsection 2.1.2, which states that the native TiO_2 layer is sputtered from the Ti target prior to deposition of Ti metal.

Assuming that the influence of sample preparation and film thickness on the spectrum are negligible we can identify spectra of two samples which differ from the other three: The spectra of samples SZ_001 and Quarz.Ti_008 are shifted towards longer wavelengths. A comparison with literature was done to check if the observed shift could be a random.

A small collection of literature data is displayed in table 3.3. Apart from the band gap E_g the wavelength of the first visible peak in the spectrum which occurs in the wavelength region with higher transmittance is listed. This number is used as a measure for the position of the steep section of the spectrum when no band gap energy was given and serves to compare the spectra to those measured in the present study, where no band gap energy was determined. In literature there is also some variation within the

Table 3.3: Overview of properties of optical spectroscopy measurements on TiO₂ thin films in literature compared to this work

ref.	film thickness/nm	preparation method	substrate	$\approx \lambda$ at 1 st peak/nm	E_g /eV
[124]	145	sol/gel	quartz glass	370	3.19 or 3.26
[125]	?	sol/gel	quartz glass	360	-
[104]	130...220	reactive DC magnetron sputtering	glass	375	3.28 or 3.31
[126]	102...391	reactive DC magnetron sputtering	In-doped SnO ₂ -coated glass	380	-
[106]	170	DC magnetron sputtering	quartz glass	380	3.12...3.2
[127]	300	RF magnetron sputtering	quartz glass	375	3.23...3.31
[128]	600	reactive RF magnetron sputtering	quartz glass	370	3.25...3.33
this study	100 (nominal)	DC magnetron sputtering	quartz glass	365	-

position of the steep section in the spectrum. Except for the spectra of samples SZ_001 and Quarz_Ti_008 the data for the position of the first peak in the high transmittance part of the spectrum measured in this work (360...375 nm) correspond acceptably to the data observed in literature, but the literature value for the first peak after the steep section in the spectrum tends to be at slightly higher wavelengths. Therefore, another parameter is likely to cause the right-shift. Among the literature data given in table 3.3 the only study using rutile samples is [106], all other measurements were carried out on the anatase polymorph. Interestingly, the position of the characteristic peak indicated in the table is similar for anatase and rutile, and also film thicknesses are comparable. This is surprising because due to the different band gap of rutile (3 eV corresponding to 413 nm [56]) a shift in the spectrum is expected. Nevertheless, the right-shift in the spectra of samples SZ_001 and Quarz_Ti_008 is attributed to the rutile crystal structure of these two samples. For Quarz_Ti_008 this was found from an XRD measurement (see table 2.4 on page 18). Sample SZ_001, for which no X-ray diffractogram was recorded, is therefore also assumed to have rutile structure. The unusually high band gap of rutile in the study by [106] remains unexplained.

Concerning the absorption of light with $\lambda = 365$ nm, which we set out to check, this wavelength will practically not be absorbed. Better absorption was expected from the literature value for the anatase band gap of 3.2 eV (see table 3.3) which corresponds to around 387 nm. The used LED also emits wavelengths shorter than 365 nm, but their intensity is very low, see figure 3.10. For example, blue light with 350 nm is emitted with an intensity of a little less than 5% compared to the intensity at 365 nm. At 350 nm the used TiO₂ layers are expected to absorb at least a little bit of the incident light. It is however not clear, how the considerable electric effects could be measured given this faint absorption. This needs further investigation. While the spectra shown here were

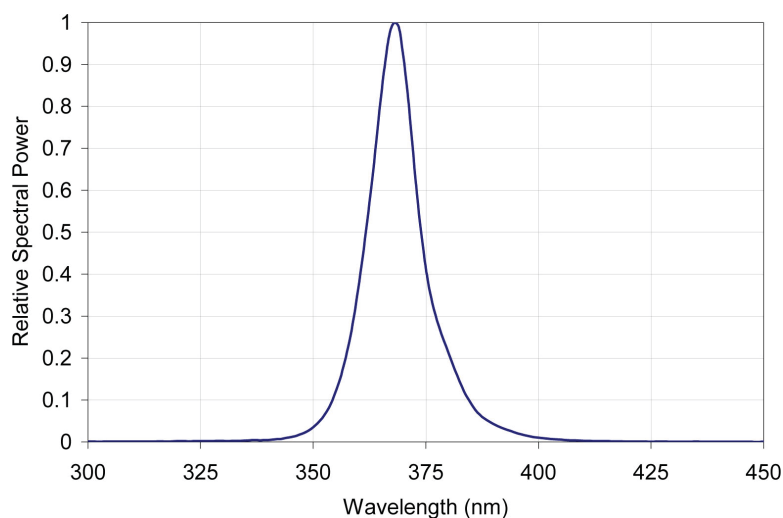


Figure 3.10: Spectrum of the 365 nm LED taken from the datasheet [129].

recorded on titania thin films on quartz glass it would be interesting to measure transmission spectra on YSZ|TiO₂ samples because this is the materials combination used in electric measurements. This could perhaps clarify if absorption occurs by interface states at the YSZ|TiO₂ interface.

The absorption behaviour of single crystalline STO is very different to the situation described for titania. STO absorbs light with 365 nm completely and the band gap decreases with temperature (see [122] for details).

3.1.3 Probing a single interface

To find out more about the origin of the voltage changes observed on TiO₂ WEs it would be advantageous to examine the metal|TiO₂ and the TiO₂|YSZ interface separately because they might cause charge separation due to the electric field present at the interface. In this subsection it is shown why this is experimentally extremely challenging. The two most obvious sample geometries for such an experiment are shown in figure 3.11. Cell type (a) depicts a cell with a titania layer on YSZ, topped by a Pt current collector. This type of cell was already used for testing titania as a photoelectrode material. The current collector and also the titania layer can be microstructured into different shapes, the Pt grid on a macroscopic titania layer in figure 3.11 is just an example. Also the substrate can be varied. If the voltage is measured between the current collector and the titania layer the photoactivity of the metal|titania interface should be probed. Cell type (b) has an additional Pt current collector underneath the titania layer. This type was not used in this work because it has two Schottky contacts which are both illuminated. If a voltage is produced at one interface a voltage equal in magnitude but opposite in sign is expected to occur at the other Schottky contact as well, so they will cancel and no statement is possible if the metal|TiO₂-interface in our cell contributes to the overall voltage.

The measurement results on (a)-type cells are summarized in table 3.4. All measurements were carried out at 400°C set temperature on titania layers with a desired thick-

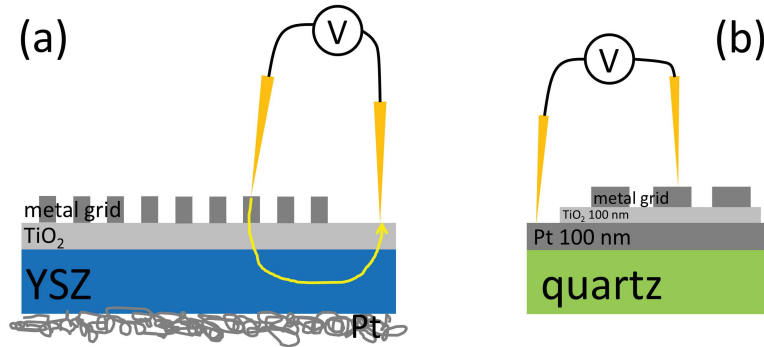


Figure 3.11: Two possible samples geometries for probing the metal|TiO₂-interface. (a): An electrochemical cell could be measured instead of a single interface. (b): Two Pt|TiO₂ interfaces can be within the mean free path of electrons and holes.

Table 3.4: Summary of measurements aiming at the investigation of the Schottky-contact metal|TiO₂

sample name	electrode	heat treatment	substrate	light effect
SZ..001	macroscopic, Pt stripes	10 min/600°C	quartz glass	none
SZ..003c	with 25µm, distance	during measurement	quartz glass	none
SZ..004a, SZ..004c	100µm on TiO ₂	2 h/900°C	MgO	none
SZ..005a, SZ..005b		2 h/900°C	s.c. YSZ	5...40 mV
YSZ..Ti-Pt-Kreise..004	Pt circle (∅= 200 µm) on TiO ₂ circle (∅= 300 µm), #1	2 h/900°C	s.c. YSZ	40 mV
YSZ..Ti-Pt-Kreise..004	Pt circle (∅= 200 µm) on TiO ₂ circle (∅= 300 µm), #2	2 h/900°C	s.c. YSZ	none
YSZ..Ti-Pt-Kreise..004	Pt circle (∅= 200 µm) on TiO ₂ circle (∅= 300 µm), #4	2 h/900°C	s.c. YSZ	none
YSZ..poly_8	Pt circle (∅= 200 µm) on TiO ₂ circle (∅= 300 µm)	2 h/900°C	p.c. YSZ	100 mV

ness of 100 nm. They were extremely prone to disturbances. However, in some cases a light effect can clearly be observed. The most pronounced change in voltage upon irradiation with blue light is shown in figure 3.12.

In spite of non-ideal measurements the results show a correlation between the appearance of the light effect and the substrate. YSZ seems to be a necessary (but not sufficient) condition for a voltage change when the blue light is turned on.

Explaining the influence of the substrate turns out to be not straightforward because at first glance it is not part of the electric circuit and therefore the space charge at the TiO₂|YSZ interface should not play an important role. However, another circuit is possible, see the yellow line in figure 3.11 (a). In this alternative circuit not only the metal|TiO₂ interface can act as a voltage source but also the TiO₂|YSZ interface. Additionally, since an electrolyte is involved, also a Nernst voltage, from whatever origin, is conceivable. Therefore, this measurement setup cannot be used. It doesn't make sure that the only measurable voltage is the one originating from the metal|TiO₂ interface.

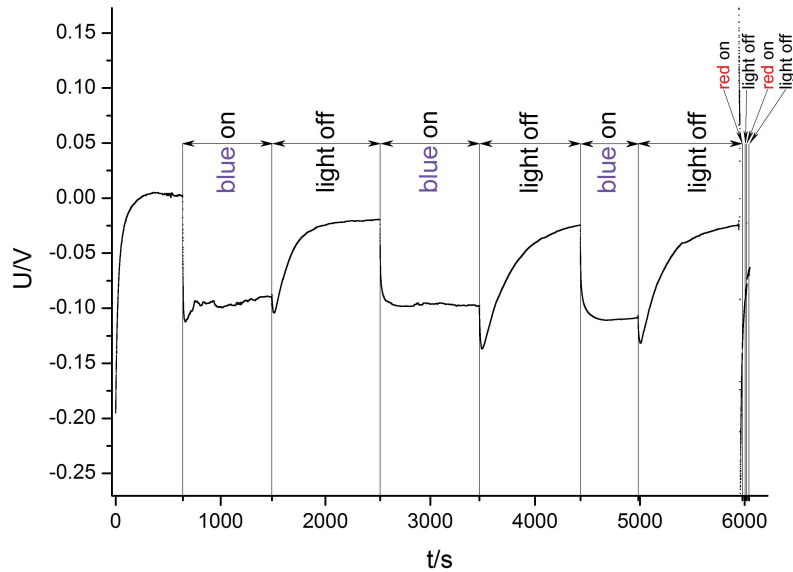


Figure 3.12: $U(t)$ curve for a circular microelectrode (Pt circle with $\varnothing = 200 \mu\text{m}$ on TiO_2 circle with $\varnothing = 300 \mu\text{m}$) where the voltage was measured between Pt and TiO_2 .

3.1.4 The “typical” effect

While optimizing the sample design of the metal| TiO_2 |YSZ system many different geometries and materials were tried out. The results varied but taking advantage of the fair amount of samples and measurements the search for a light effect that is typical in spite of the inhomogeneous ensemble of samples promises to yield a result. In this subsection it is therefore attempted to divide measurements into two groups: (1) measurements showing a similar $U(t)$ behaviour, which can be termed “typical”, and (2) all other measurements. $U(t)$ curves of group (1) samples are schematically depicted in figure 3.13. Without irradiation there is a certain offset voltage which is termed U_{dark} . When blue light is switched on there is a sudden voltage jump towards negative values. Since very quick voltage changes are typical for PV cells we call this initial fast voltage change (vs. U_{dark}) U_{PV} . Further investigations and interpretations follow in the next chapters. Then the curve goes back towards more positive values and develops a steady state and the corresponding voltage compared to U_{dark} is given the name U_{ss} . There may be several inflection points in the voltage curve as it develops into the plateau. Upon switching off the light there is again a fast jump towards positive values. The voltage remaining directly after switching off the light, compared to U_{dark} , is given the name U_{batt} because it is like the voltage of a battery that has been charged during illumination. Finally the voltage reaches its dark value again. In figure 3.13 not only these values but also differences are indicated because they will be listed in subsections 3.3.1 for TiO_2 and subsection 3.3.2 for STO.

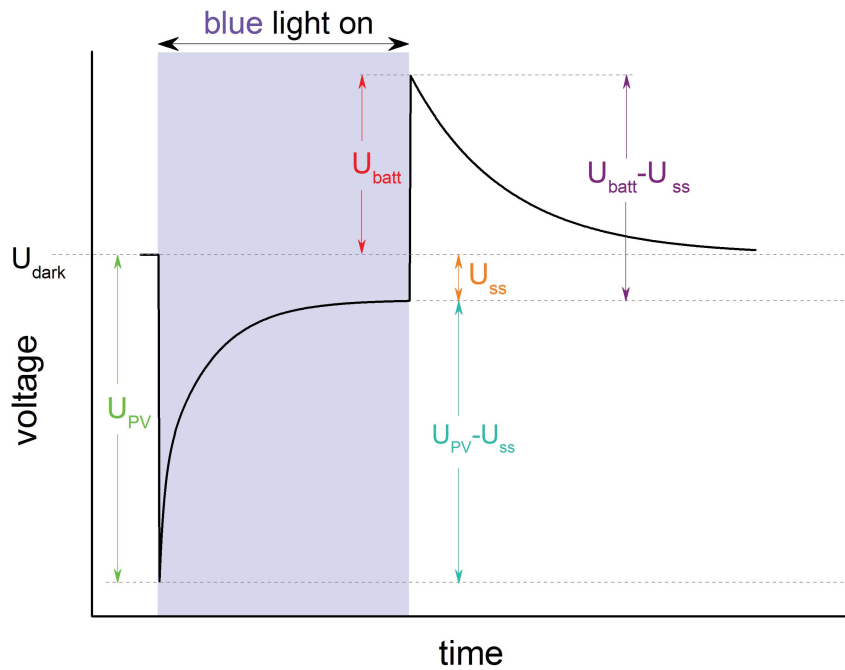


Figure 3.13: Typical $U(t)$ curve.

Table 3.5: Results of search for a typical light effect on TiO_2 WEs.

	no. of samples	no. of electrodes	no. of measurements	no. of geometries
typical effect	22	35	37	6
any other effect	20	25	25	7

Examples for measurements of typical and non-typical effects are shown in figure 3.14 (a) and (b), respectively. The measurements analysed here were all carried out in air at a set temperature of 400°C or 500°C , the results are shown in table 3.5. The presumably typical effect was observed on more samples and on more electrodes.

Variation between different samples

Are there samples on which both kinds of effects, typical and non-typical were measured? Yes, indeed. On six samples both the typical and the untypical effect occurred. Therefore, the appearance of typical or untypical effects can be caused by random variations between samples, but not only. Consequently, the geometry dependence of the light effect was analysed.

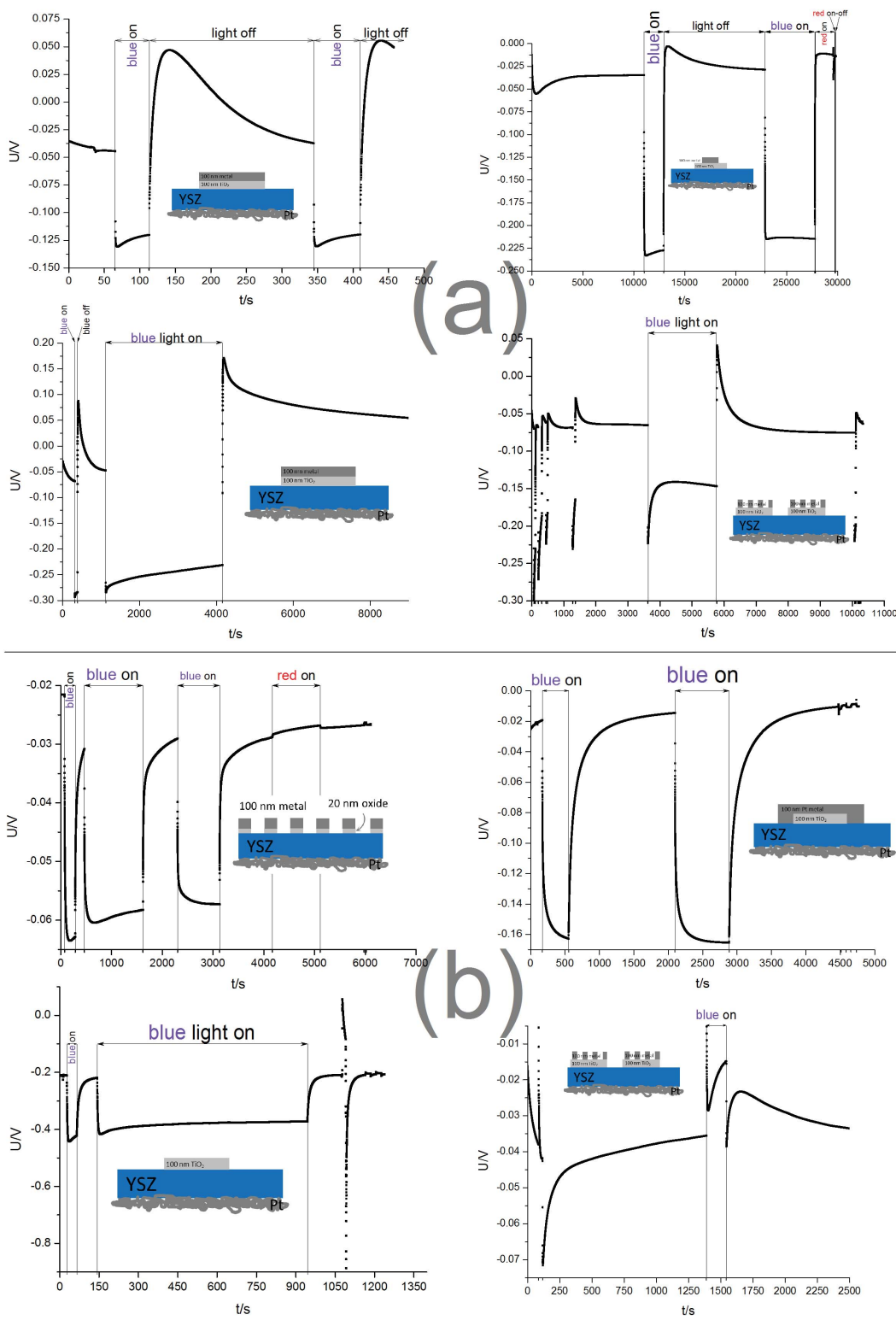


Figure 3.14: (a) typical and (b) untypical $U(t)$ measurements.

Geometry dependence

A geometry dependence can be deduced from the data in table 3.6, where occurrence of the typical and untypical effect is counted for all examined geometries.

Table 3.6: Data on geometry dependence of light effects

no.	name	geometry		effect	
		sketch		typical	untypical
1	grid			3	7
2	lid			3	-
3	hat			4	3
4	pyramid			10	1
5	pure TiO2			2	8
6	micro-circle with grid			14	5
7	macro-layer with grid			-	1
8	grid-type micro circles			-	1

The typical effect occurs preferably but not exclusively on geometries no. 2, 4 and 6, whereas the untypical effect seems to be favoured by geometries no. 1 and 5. Interestingly, geometries 2, 4 and 6 have two features in common: They have micro-electrodes and Pt does not fully cover TiO₂.

Random variation and geometry dependence combined

There are five samples on which both the typical and the untypical effect were observed on the same electrode geometry. So, is the “typical” light effect still typical if it can not be attributed to certain samples or geometries?

Further samples with STO as WE showing the typical behaviour will be presented in subsections 3.3.2 and 3.4.2. The appearance on different materials further supports the hypothesis that the effect is typical.

3.2 Is there a light effect on strontium titanate?

Absorption of light by the STO single crystal is expected due to its band gap of 3.3 eV (extrapolation to 0 K) or rather 2.9 eV at 350°C (measured for weakly Fe-doped STO in ref. [93]). In-depth measurements of the absorption of STO single crystals and thin films were carried out in [122]. A plot taken from [122, 130] showing transmission spectra of an STO single crystal is displayed in figure 3.15.

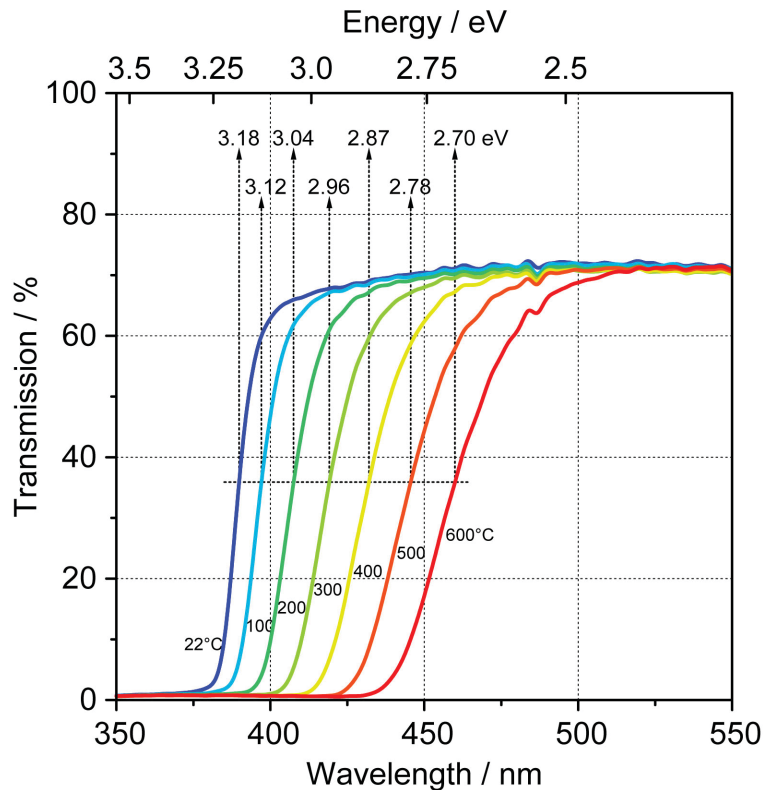


Figure 3.15: Transmission spectra of a nominally undoped STO single crystal measured in the same setup as the TiO₂ thin film samples. Plot reprinted from [122, 130].

There are only three STO samples (YSZ_STF0.4_001, STO_001, STO_002b) which all behave typical. They will be presented in detail in subsection 3.3.2. Three samples would not be enough to make any statement about the type of effect but given that many TiO₂ samples behaved similarly the three STO samples can be classified to be typical.

3.3 Systematic voltage measurements

3.3.1 Titanium dioxide

In the present subsection the response of a typical $U(t)$ curve's features to systematic variation of parameters such as current collector material, $p(\text{O}_2)$ or temperature is discussed.

Equilibration time

Since very little is known about the influence of light on the defect chemical properties of MIECs the interpretation of measurement results is easier if the effect of light can be investigated with or without an additional driving force. Therefore, the time needed for equilibration of a thin film sample in a new atmosphere has to be estimated.

First, the rate-limiting process must be determined. It can be either associated with the oxygen exchange on the electrode surface or with chemical diffusion in the electrode bulk. Nowotny *et al.* measured the kinetics of the gas-solid reaction on rutile single crystals at temperatures above 800°C in atmospheres with $p(\text{O}_2)$ between 1×10^{-13} and 7.5×10^4 Pa. The authors found out that bulk diffusion is rate-limiting under these conditions [74]. Further long-term investigations by this group (more than 1500 h) revealed two kinetic regimes, both of which were governed by bulk transport phenomena [75]: Kinetic regime I was associated with the movement of oxygen vacancies, kinetic regime II with the slower motion of titanium vacancies.

At low temperature, however, the rate-limiting process could change, as is the case in STO, for example [93], due to a change in activation energy of the diffusion process. Surface-controlled reaction kinetics are additionally favoured by thin films compared to bulk samples [93].

For titania thin films at low temperature (200...325°C) Rothschild *et al.* did find that the oxygen incorporation kinetics is dominated by a surface process within the first few minutes [131, 132]. Then, however, the diffusion into the film became rate-limiting. The authors emphasized the role of grain boundaries as diffusion paths in nanocrystalline thin films in a different paper [133]. In contrast to this, Gundlach & Heusler pointed out that "an interfacial reaction must determine the rate at which oxygen is incorporated into the oxygen deficient oxide" [95]. It is clear from the text that this limitation by surface reaction persists for the majority of the investigated time, and not only in the beginning. Rothschild *et al.*, who quoted Gundlach & Heusler [132], do not resolve this apparent contradiction by stating that the reaction occurred "in two stages with first chemisorption of oxygen, involving rate-determining electron transfer to oxygen adsorbates followed by incorporation into the non-stoichiometric oxide by diffusion". A reconciliation of both studies is perhaps possible by taking into account the measurement temperature. Gundlach & Heusler measured at 77°C and below which is about 123°C lower than in the study by Rothschild *et al.* and could be enough for a change in mechanism to happen.

A worst-case scenario for the equilibration time of the thin film samples used in this work can be estimated using the chemical diffusion coefficient "associated with the transport of Ti vacancies" measured in [75] in an atmosphere of 0.75 bar oxygen, which has to be extrapolated from the high temperature (850...1050°C) to the low temperature

regime (350...450°C). This diffusion coefficient describes the ambipolar diffusion of Ti vacancies and positive counter charges such as holes and therefore is the chemical diffusion coefficient of Ti. As a rule of thumb the time needed for the sample to be more or less in equilibrium with the surrounding atmosphere can be calculated as $10 \cdot t$ from the equation for the diffusion length $L = \sqrt{Dt}$ by inserting the extrapolated chemical diffusion coefficient for Ti for D and the sample thickness for L . This is of course a very rough estimation by no means least because the time needed for equilibration to a new atmosphere depends on the defect chemical state that the sample is in after preparation. The result is approximately 167 h for a 100 nm thin film at 350°C and 4.6 h at 450°C. It follows from this consideration that equilibration should be possible by heating a sample overnight in the new atmosphere at 500°C set temperature. This was done for samples YSZ_TiO2-Pt_Ana2-550.009 to ...012.

For samples measured at 400°C set T , which corresponds to roughly 360°C (see subsection 3.4.1), equilibration might not be possible overnight. Since many samples were equilibrated for an even shorter time (around 1/2 h) it was attempted to assess the influence of the equilibration state on the voltage measurements. On eight samples (100 nm nominal film thickness, oxidised by heat treatment 2 h/550°C in air, different current collector materials (Pt, Ag, Au), micro-circles with grid (geometry no. 6, table 3.6)) the difference in light effect observed shortly after the beginning of the measurement and after about 16 h was judged. In only two cases there was a significant change in voltage response upon blue light. Figure 3.16 shows an example for a slight and a significant change (top and bottom panel, respectively). As the time of illumination was not the same every time it is possible that this parameter also affects the voltage response. It follows from these measurements that either the samples were equilibrated more than estimated or that the defect chemical state of the thin film did not change significantly during the measurement. Both possibilities are acceptable and do not hamper the interpretation much. However, assessing whether blue light can cause defect concentrations in a MIEC to deviate from their equilibrium values, thus representing a driving force, is only possible on equilibrated samples. In contrast to this, a change in voltage is also expected on a sample on its way to equilibrium, which is e.g. accelerated by blue light (catalytic effect).

Current collector

Varying the current collector material and position is a very interesting experiment because it changes the properties of the metal|MIEC interface which might have an influence on the voltage change upon irradiation with blue light. In the first part of this subsection different metals used as current collectors are treated. The second part deals with LSC on top of titania electrodes.

Metals as current collectors All samples had a TiO₂ layer with a nominal thickness of 100 nm that was produced by oxidation of the sputtered film at 550°C in air for 2 h. They were equilibrated in air at the measurement temperature for different periods of time. Equilibrating at 400°C set temperature might not be enough to fully equilibrate the thin film but as was shown in the previous subsection this influence is likely to be not dramatic. Additionally, the comparisons made in the present subsection are still valid because the light effect is only assessed in a very rough manner: The highest

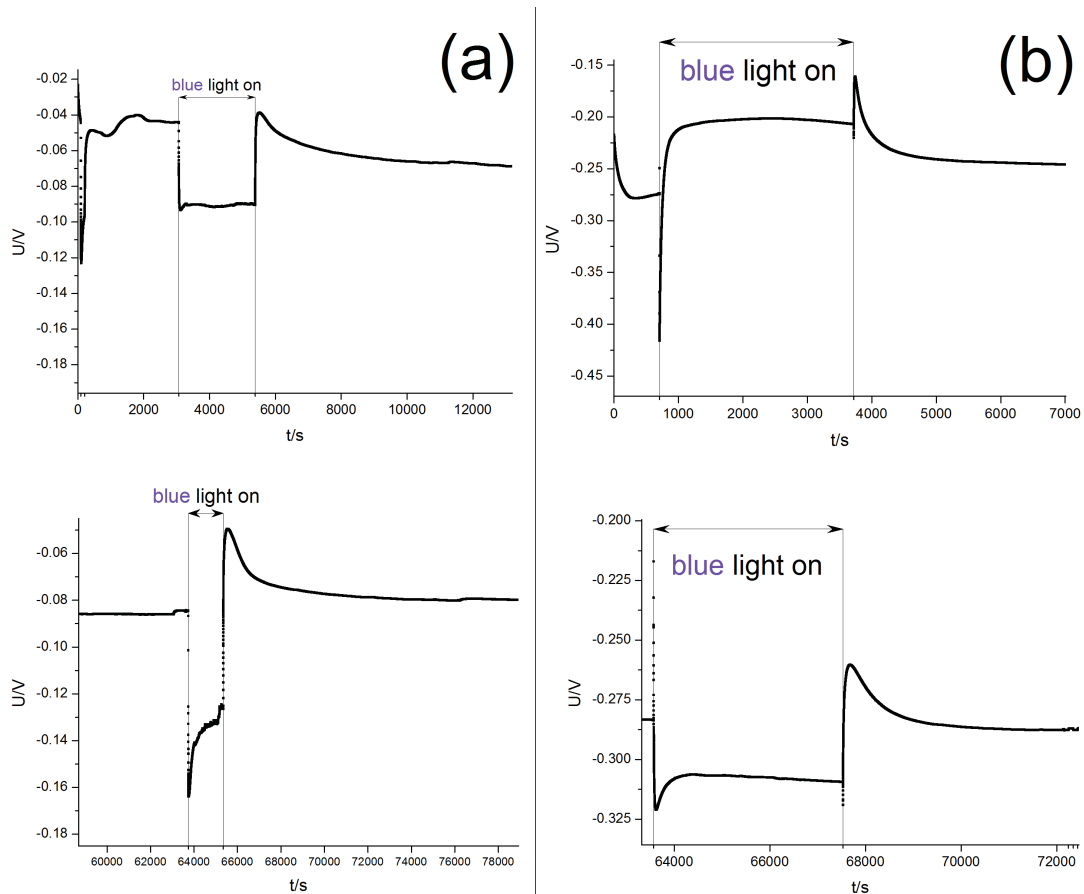


Figure 3.16: Examples for the effect of equilibration time on the voltage response upon irradiation of blue light (samples YSZ-TiO₂-Pt-Ana2-550_002 and ...006, WE = micro-circle with grids). (a): Slight change from measurement after around 1 h (top panel) to measurement after around 18 h (bottom panel). (b): Significant change within about the same time.

Table 3.7: Comparisons of U_{\max} and U_{dark} with Ag or Pt current collector on top.

		comparison 1		comparison 2		
set temperature/°C		500		400		
		$U_{\text{dark}}/\text{mV}$	U_{\max}/mV		$U_{\text{dark}}/\text{mV}$	U_{\max}/mV
results	Pt 010	5	70	Pt 004	50	150
	Pt 012	10	80	Pt 010	40	150
	Ag 002	30	25	Pt 009	75	150
				Ag 001	20	20

Table 3.8: Effect of current collector position (on top of the titania layer or buried underneath) on voltage offset and maximum voltage. Pt current collector, 400°C set temperature, air. The data for the samples with the current collector atop are the same as in table 3.7, comparison 2.

on top			buried		
sample	$U_{\text{dark}}/\text{mV}$	U_{\max}/mV	sample	$U_{\text{dark}}/\text{mV}$	U_{\max}/mV
Pt 004	50	150	Pt 006	80	80
Pt 010	40	150	Pt 008b	25	50
Pt 009	75	150			

deviation from the offset voltage is taken as a general measure for the photoactivity (U_{\max}). Also, the voltage offset U_{dark} itself is extracted here and subject to analysis. All voltages are approximate absolute values.

Table 3.7 shows two comparisons of samples with Pt and Ag current collectors, deposited on top of the titania layer. Samples in comparison 1 were equilibrated overnight, except for sample Pt 009, which was only equilibrated for 4000 s. It was included in the comparison anyway because no significant change occurred within the last 2000 s of the measurement. These data suggest that while the voltage offset is similar for Pt and Ag current collectors the Pt current collector causes higher photo-effects compared to Ag. In each comparison there is only one sample with a Ag current collector but this disadvantage is compensated by considering two different comparisons.

The influence of the current collector's position (on top or buried) can be evaluated from the data in table 3.8. Measurements were performed at 400°C set temperature in air. The samples with the current collector on top are the same as in table 3.7. Sample Pt 006 was equilibrated for 60000 s, sample Pt 008b only for 4000 s, but they are included in the comparison by the same argument as above. While the voltage offset is comparable for both types of samples the photovoltage is considerably smaller when a buried current collector is used.

Finally the influence of Au compared to Pt on the voltage offset was investigated. To do this U_{dark} was compared for different types of typically behaving samples with Au or Pt current collector, regardless of their geometry or equilibration state.

Table 3.9: Voltage offset U_{dark} on Au samples at 400°C in air. All samples were equilibrated for at least 10000 s.

sample	geometry no. (see table 3.6)	$U_{\text{dark}}/\text{mV}$
Au 004	6; μ -circle with grid, current collector on top	250
Au 002	μ -circle with grid, buried current collector	275
Au 001	2; lid	325

If, despite these differences in geometry, a tendency can be observed this results in a quite general statement. From the Pt samples treated so far we can extract an offset voltage between 5 and 80 mV. When comparing this range to U_{dark} for the Au samples presented in table 3.9, which is >250 mV, it is clear that the use of Au as a current collector material enhances the voltage offset.

LSC as a current collector The use of current distributing metal structures on titania is expected to limit the zone which is active for the oxygen exchange reaction to the triple phase boundary TiO_2 -metal-gas because no oxide ion transport is possible through the bulk of a metal. For Pt it was suggested that a bulk path, most likely along grain boundaries, exists at low temperatures [134], but using a MIEC with high electronic and ionic conductivity as well as low surface exchange resistance promises to facilitate oxygen exchange and transport, thereby maximising the active reaction area and increasing the chance to not only measure a photovoltage but also a photocurrent. On two samples with titania on YSZ (produced by oxidation of Ti in air for 2 h at 900°C) LSC was deposited by PLD (see subsection 2.1.2) and microstructured into lid- and hat-type electrodes (for geometry sketches see table 3.6). Three lid-type as well as three hat-type electrodes were measured at 400°C set T in air on each of the two samples. Electrodes with the same geometry behaved similarly with only one exception. Typical $U(t)$ curves for lid- and hat-type TiO_2/LSC and TiO_2/Pt electrodes (also produced *via* the 2 h/900°C method) are compared in figure 3.17. Here, on the LSC-containing samples only a small voltage change upon illumination with blue light was observed. Almost no permanently changed voltage remained while the light was on. Compared to the TiO_2/Pt samples the voltage changes were faster. As a consequence of the almost vanished light effect LSC could not be used as a current collector material.

LSC electrodes next to TiO_2

With the possibility of measuring a significant photocurrent on a kinetically fast electrode in mind $U(t)$ curves were recorded on LSC electrodes located close to TiO_2 electrodes but without LSC touching TiO_2 . As shown in subsection 3.1.1 LSC electrodes are not photoactive themselves.

Samples with four different geometries were investigated at 400°C in air. The geometries and resulting $U(t)$ curves are shown in figure 3.18. Only one sample of each type was measured. The only sample on which a light effect was demonstrated is sample LSC64-TiO2.001c, shown in figure 3.18 (a). It consisted of stripes of TiO_2 and LSC which were about 45 μm wide and around 2.5 mm in length. They were separated from each other by a channel that was about 10 μm wide. The $U(t)$ curve shown in figure 3.18

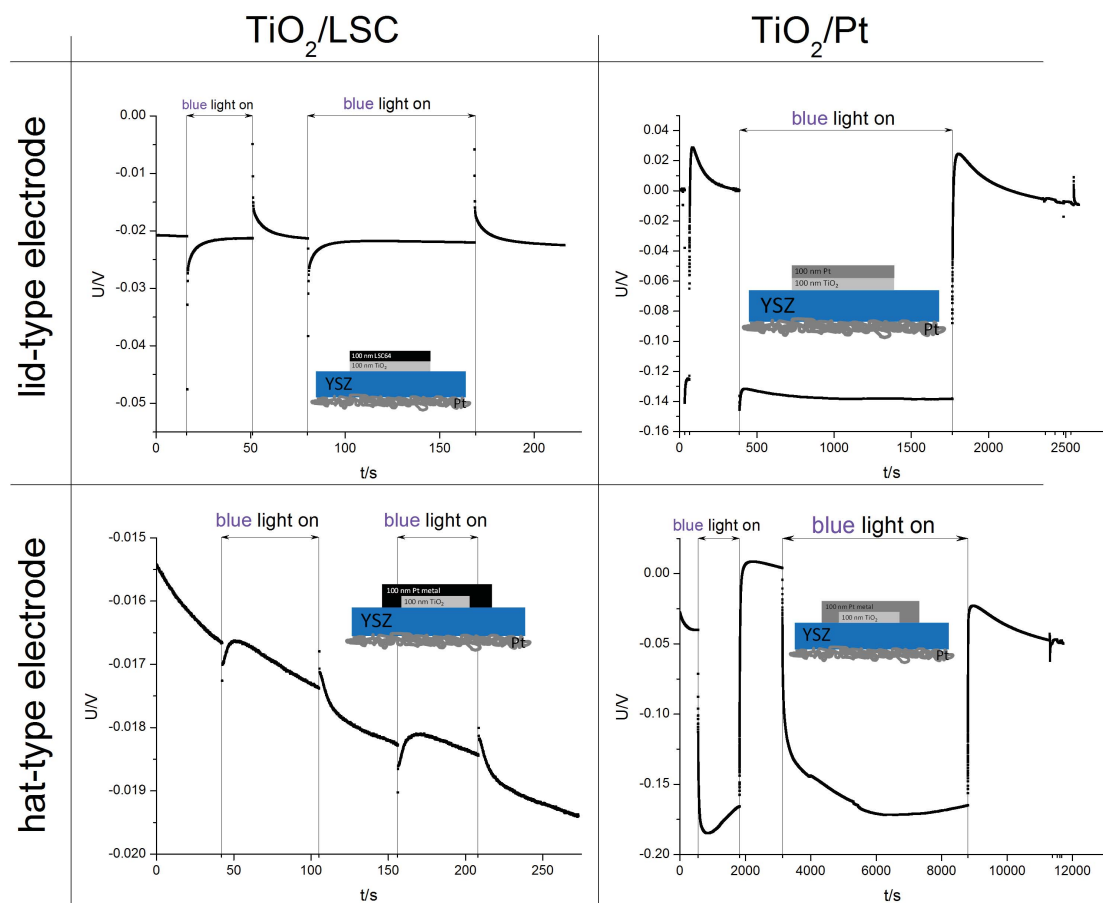


Figure 3.17: Two typical $U(t)$ measurements on lid- and hat-type TiO_2 electrodes with LSC as a current collector material at 400°C set T in air compared to TiO_2/Pt electrodes with the same geometry under the same conditions. Light effects on TiO_2/LSC are very small and decay times are fast compared to the TiO_2/Pt samples.

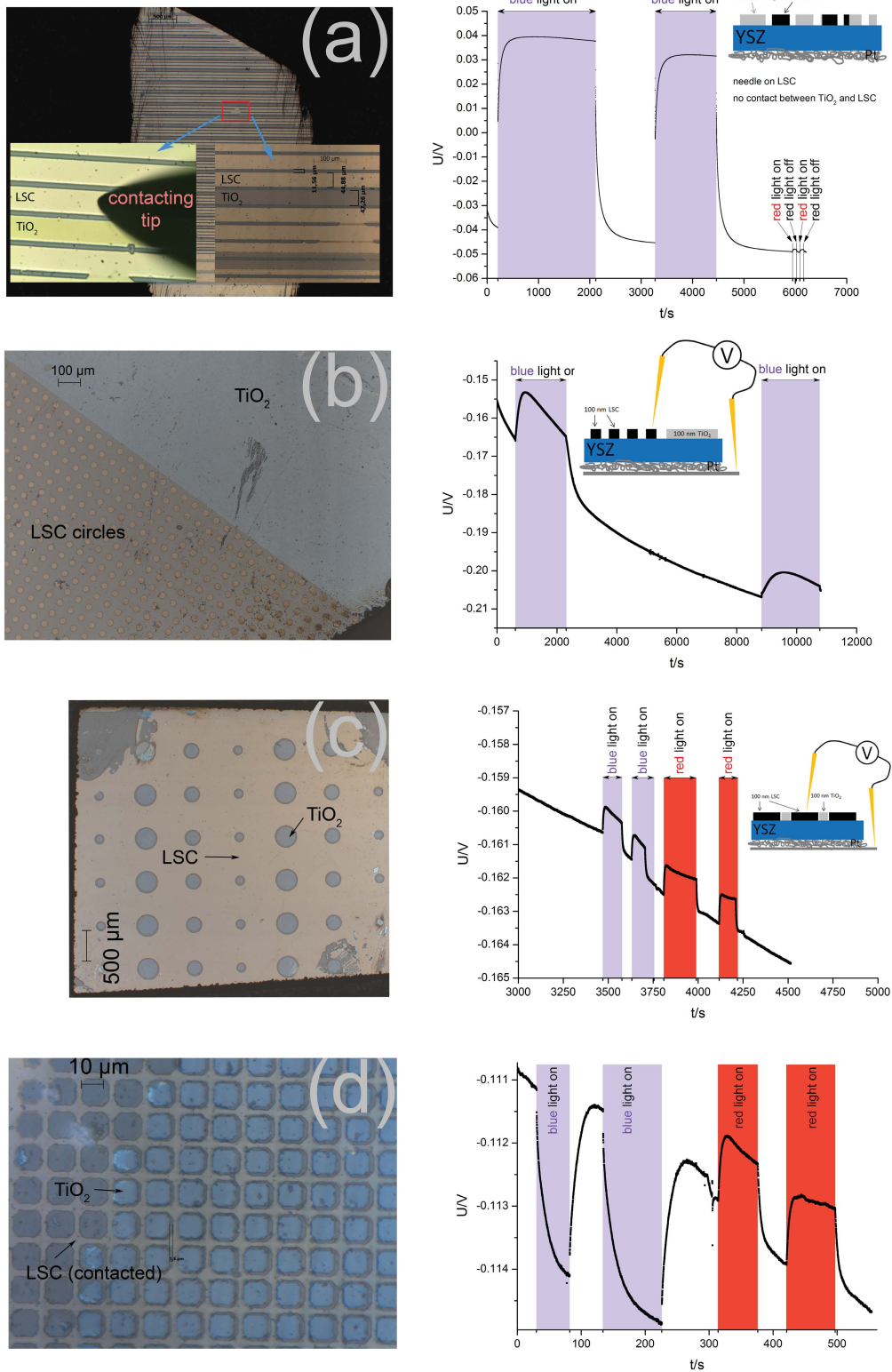


Figure 3.18: Four different sample geometries and measurement results for the investigation of the light effect on electrodes close to titania. Geometry (a) is the only sample that showed an effect upon irradiation with blue light.

(a) depicts the voltage changes between LSC as a working electrode and the porous Pt counter electrode. Clearly a change of approximately 80 mV occurs, although the shape of this response cannot be classified as "typical". $U(t)$ curves during use of blue light were also recorded for the titania strip as a WE vs. CE and for LSC vs. TiO_2 . The titania electrode measured vs. CE behaved typically. When LSC was measured vs. titania also a "typical" response to blue light was recorded. When the steady state voltages (corrected by the offset) during the illumination are added for TiO_2 vs. CE and LSC vs. CE, they are in good agreement with the voltage measured between TiO_2 and LSC. These findings were demonstrated on two different spots on this sample and suggest that LSC acts a voltage probe on YSZ, which is polarized next to TiO_2 . Considering the absence of a metal on TiO_2 in this experiment these findings could be interpreted to imply a photoactivity of the $\text{TiO}_2|\text{YSZ}$ interface.

Sample LSC64-TiO2_002_c, shown in figure 3.18(b), featured LSC circles ($\varnothing = 20 \mu\text{m}$) in various distances from a big ($\approx \text{mm}^2$) titania area, the closest LSC electrode being around $5 \mu\text{m}$ away. No light effect could be measured on this sample for LSC vs. CE.

Sample LSC64-TiO2_003a, presented in panel (c) of figure 3.18, consisted of a titania layer with circular holes (nominal $\varnothing = 350 \mu\text{m}$) into which LSC circles (nominal $\varnothing = 300 \mu\text{m}$) were inserted. The distance titania-LSC was between 25 and $35 \mu\text{m}$. No light effect was observed when LSC was measured vs. CE.

Sample LSC64-TiO2_002b had an LSC grid with stripes of around $2 \mu\text{m}$ width (figure 3.18 (d)). Into the free spaces titania squares were inserted that did not touch the LSC on large parts of the sample. When LSC was contacted as a WE and the voltage was measured as a function of time vs. the Pt counter electrode using blue light no effect could be noticed.

To sum up, the effect of LSC being polarized when in proximity to titania could only be measured on one sample, but two times. The results of measurements of LSC, titania and counter electrode vs. each other are consistent and indeed suggest a polarization of LSC during illumination without being in contact with TiO_2 and even though the material itself prove to be not photoactive. This "distance effect" could not be reproduced on samples with similar LSC- TiO_2 distances but other geometries.

Oxygen partial pressure

The oxygen partial pressure dependence of two voltage values in a typical $U(t)$ curve (see figure 3.13) was investigated on four samples at 500°C set temperature: The voltage offset U_{dark} and the voltage change compared to U_{dark} remaining directly after switching off blue light, U_{batt} .

Three different $p(\text{O}_2)$ were used (see also section 2.2): Ambient air (0.21 bar), $\approx 1 \times 10^{-5}$ bar (10 ppm O_2 impurities in N_2) and $\approx 1 \times 10^{-30}$ bar ($\text{H}_2/\text{H}_2\text{O}$ mixture¹).

The resulting values for U_{dark} and U_{batt} at these three $p(\text{O}_2)$ are presented graphically in figure 3.19. Generally the values vary strongly in air and N_2 but not in reducing atmosphere, where both U_{dark} and U_{batt} almost vanish. Due to the untypical behaviour of samples Pt 009 and Pt 001 only two data points are available in air.

¹2.5% H_2 (in Arcal 10 gas mixture) were assumed to be in equilibrium with the vapour pressure of water at room temperature (22°C , gas washing bottle; $\approx 26.5 \text{ mbar}$ [135]). Using data from NIST [136–138] the equilibrium partial pressure at the estimated measurement temperature of 450°C was calculated to be 1.17×10^{-30} bar.

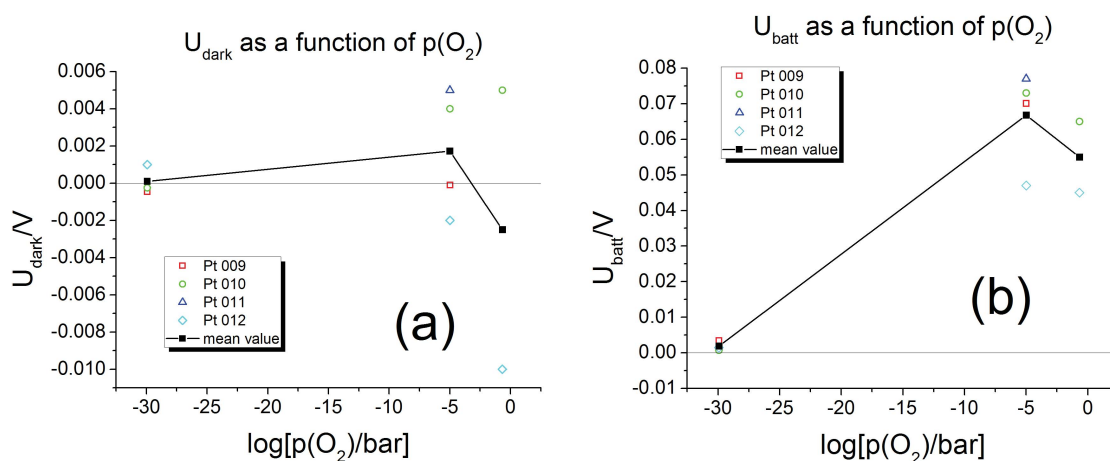


Figure 3.19: Dependence of U_{dark} (a) and U_{batt} (b) on $p(\text{O}_2)$ for samples YSZ_TiO2-Pt_Ana2-550.009...012.

Table 3.10: Useful data for titania samples YSZ_TiO2-Pt_Ana2-550.009...012 and YSZ_TiO2-Pt_Ana2-550.004.

	Pt 010	Pt 012	Pt 009	Pt 010	Pt 011	Pt 012	Pt 009	P 010	Pt 004
$T_{\text{set}}/^\circ\text{C}$	500	500	500	500	500	500	400	400	400
$p(\text{O}_2)/\text{bar}$	0.21	0.21	1×10^{-5}	1×10^{-5}	1×10^{-5}	1×10^{-5}	0.21	0.21	0.21
$U_{\text{dark}}/\text{mV}$	5	-10	-0.1	4	5	-2	-75	-40	-50
U_{PV}/mV	-50	-80	-48	-74	-110	-93	-147	-150	-185
$U_{\text{batt}}/\text{mV}$	65	45	70	73	77	47	115	85	140
U_{ss}/mV	-2	-30	19	13	-19	-41	-67	-80	-95
$U_{\text{batt}} - U_{\text{ss}}/\text{mV}$	67	75	51	60	96	88	182	165	235
$-(U_{\text{PV}} - U_{\text{ss}})/\text{mV}$	48	50	67	87	91	52	80	70	90

The voltage offset is very small in air and N_2 as well, compared to the values at 400°C set T in air, presented in subsection 3.3.1 (5...80 mV). It can be positive or negative. Both voltages U_{batt} and U_{dark} show a maximum in N_2 . However, the maximum of U_{dark} needs further investigation because it only results from taking the mean value of the two points measured in air, which are far apart.

Summary of useful data and comparison

Table 3.10 gives an overview of interesting voltage values and differences that can be read from a typical $U(t)$ curve (see figure 3.13). The samples included are YSZ_TiO2-Pt_Ana2-550.009...012 and sample YSZ_TiO2-Pt_Ana2-550.004, for which the preparation conditions were optimized. The oxidation programme was 2 h at 550°C in air. Data are given for measurements in air and N_2 . Again, measurements on samples YSZ_TiO2-Pt_Ana2-550.009 and ...011 in air had to be excluded because they were untypical. The most interesting comparisons within this data set involve samples YSZ_TiO2-Pt_Ana2-550.009...012 in N_2 because four data sets are available. The results are summarized below.

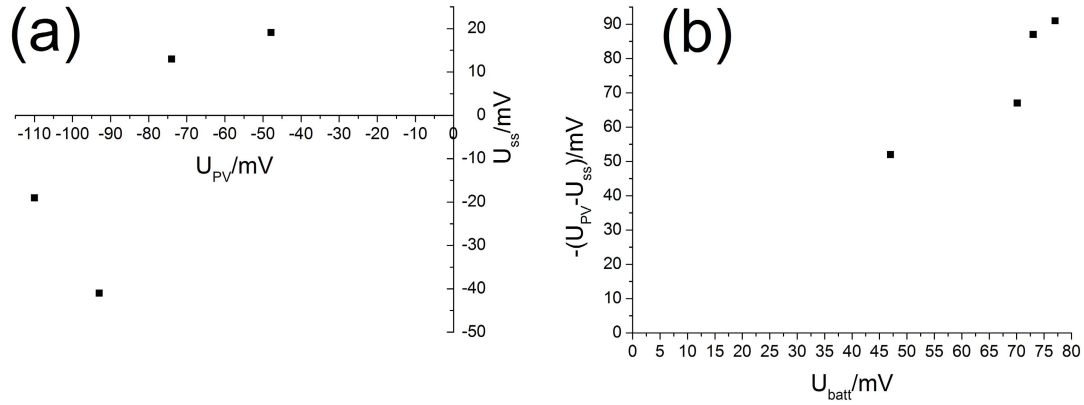


Figure 3.20: Plots generated from data in table 3.10 (samples YSZ_TiO2-Pt_Ana2-550_009...012 and YSZ_TiO2-Pt_Ana2-550_004, Pt current collector). (a): U_{SS} increases with increasing U_{PV} , one data point does not match. (b): $-(U_{PV} - U_{SS})$ increases with increasing U_{batt} .

- There is a considerable variation of U_{PV} (approximately a factor of two), whereas U_{batt} is almost the same for three of the four samples. This indicates that these two values are largely independent from each other.
- The voltage U_{SS} varied in sign, meaning that sometimes it was greater than U_{dark} , sometimes smaller. When plotting U_{SS} as a function of U_{PV} it is revealed that U_{SS} increases with increasing U_{PV} , except for one data point (see figure 3.20 (a)).
- The value $-(U_{PV} - U_{SS})$, which is a measure for the difference between the final point of the fast initial jump and the plateau, increases with increasing U_{batt} (figure 3.20 (b)). However, this value does not depend on U_{PV} .

Voltages measured at 500°C set T were generally smaller than the ones measured at 400°C set T .

3.3.2 Strontium titanate

Voltage measurements as a function of time were performed on three STO samples: two had an STO single crystalline working electrode (STO_001: Pt current collector, STO_002b: Au current collector) and a YSZ thin film electrolyte (see subsection 2.1.1), one had a weakly Fe-doped STO thin film electrode and a Pt current collector on a YSZ single crystal (sample YSZ_STF0.4_001). For STO_001 and STO_002b the oxygen partial pressure (air, N_2 , H_2/H_2O) and the temperature (400°C, 500°C, 600°C set temperature) were varied, YSZ_STF0.4_001 was only tested in air at 400°C set temperature.

Equilibration time

As for TiO_2 the equilibration time was estimated for STO samples. Chemical diffusion coefficients D and surface exchange coefficients k are available for weakly Fe-doped STO single crystals (0.03...0.29 mol% Fe) [93, 139]. It was found that below about 477°C the surface reaction is rate-determining, while the diffusion-controlled regime

is above this temperature [92]. With the k value at 500°C^2 being $1 \times 10^{-6} \text{ cm s}^{-1}$ and an STO thickness L of 0.5 mm the formula $t = L/k$ gives approximately 0.58 days for t . According to the rule of thumb mentioned in subsection 3.3.1 ($\approx 10 \cdot t$ until equilibrium is reached) this gives about 6 days. Considering that the real measurement temperatures are around 350°C and 450°C for 400°C and 500°C set temperature, respectively, it is clear that these periods of time are unfeasible for measurements of several samples under several conditions. Therefore, samples were only equilibrated overnight. At 600°C set temperature ($\approx 550^\circ\text{C}$ real temperature), however, the bulk diffusion process is rate-limiting. Taking the D value from [139] at about 500°C and using $L = \sqrt{Dt}$ the resulting time t is only around 10 min. Measurements at 600°C set temperature can thus be considered to be performed on an equilibrated sample.

Sample STO_001: Pt current collector

All $U(t)$ curves are typical. Curve shapes in reducing atmosphere differ from those in air or N_2 . Examples at 500°C set temperature are shown in figure 3.21. Given the

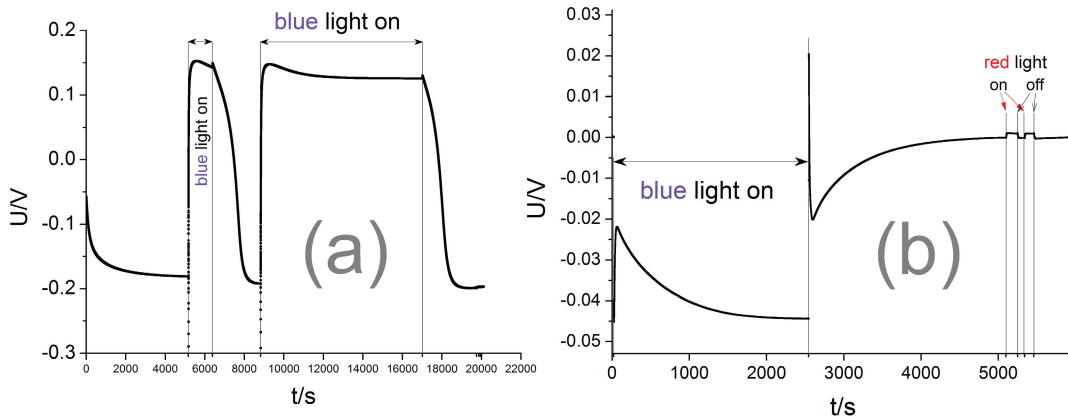


Figure 3.21: Two typical STO measurements (sample STO_001, Pt current collector) at 400°C set T (a) in air and (b) under reducing atmosphere (right).

similarly shaped curves at high and low temperature the measurements at 400°C and 500°C set T are considered at least qualitatively reasonable results despite the samples being not in equilibrium with the surrounding atmosphere.

The results of all measurements are given in compressed form in figures 3.22 and 3.23. Both U_{dark} and U_{batt} are considerably smaller in reducing than in oxidising atmosphere and show a maximum absolute value in N_2 . U_{batt} only vanishes at 600°C , it can be measured at 400°C and 500°C set temperature. The absolute values of both voltages decrease with increasing temperature.

²By looking at the k value at the high temperature of 500°C , which is already slightly above the surface-controlled regime, we get an estimation that favours a short equilibration time because surface exchange is assumed to be faster at higher T

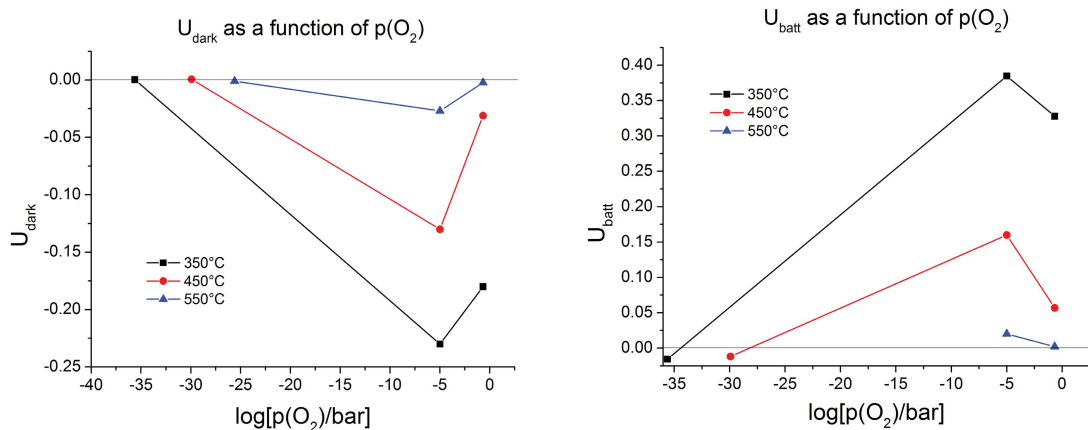


Figure 3.22: U_{dark} (left) and U_{batt} as a function of $p(\text{O}_2)$ for sample STO_001 (Pt current collector).

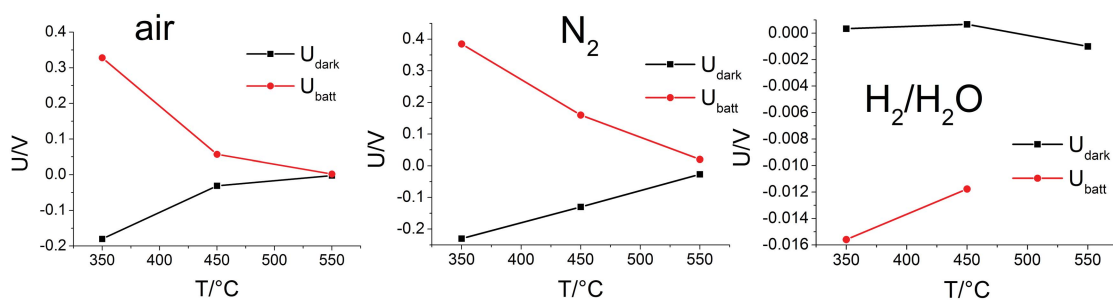


Figure 3.23: U_{dark} and U_{batt} as a function of temperature for STO_001 (Pt current collector) (approximate real T is indicated in the diagrams).

Sample STO_002b: Au current collector

Measurements in N_2 and air were typical. Despite showing a strong response to blue light at $400^\circ C$ set T the measurement in H_2/H_2O has to be described, as all measurements in this atmosphere, as untypical. Two examples for $U(t)$ curves are shown in figure 3.24. The dependence of U_{dark} and U_{batt} at $400^\circ C$, $500^\circ C$ and $600^\circ C$ set T are

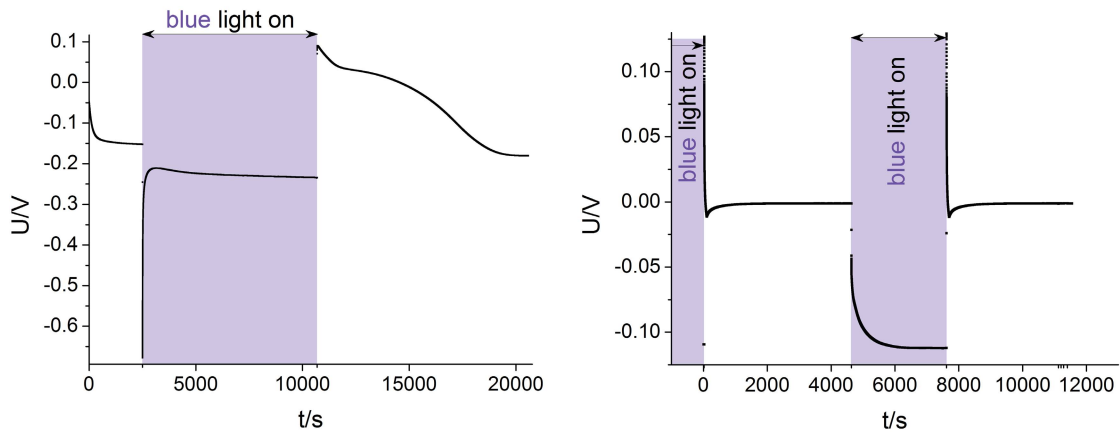


Figure 3.24: Two typical measurements on STO_002b (Au current collector) at $400^\circ C$ set T in air (left) and under reducing atmosphere (right).

depicted in figure 3.25, the dependence on temperature at a certain $p(O_2)$ is plotted in figure 3.26. At $600^\circ C$ no reasonable values for U_{dark} and U_{batt} could be read from

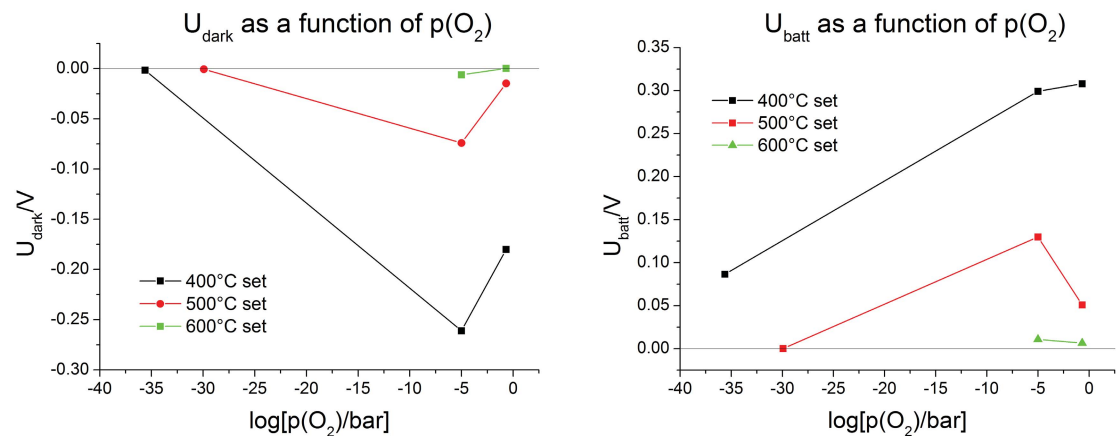


Figure 3.25: U_{dark} (left) and U_{batt} as a function of $p(O_2)$ for STO.002b (Au current collector).

the data. The voltage offset has its maximum in N_2 at $400^\circ C$ and $500^\circ C$ set temperature. The "battery voltage" has a maximum in N_2 at $500^\circ C$, and in air at $400^\circ C$ set temperature.

Both voltages decreased with increasing temperature in all atmospheres investigated.

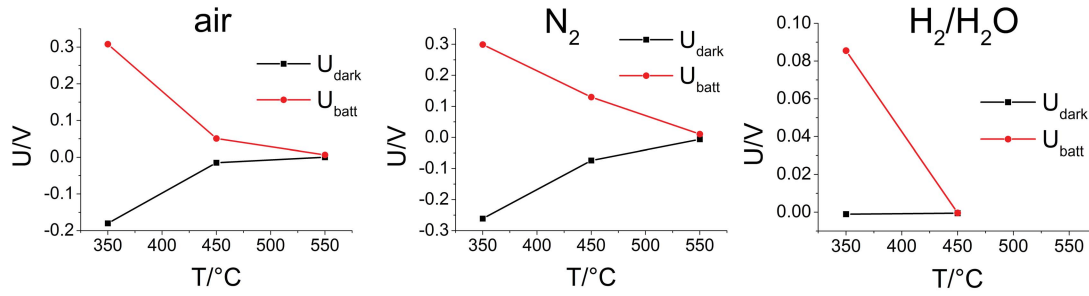


Figure 3.26: U_{dark} and U_{batt} as a function of temperature for STO_002b (Au current collector).

Sample YSZ_STF0.4_001

$U(t)$ curves were recorded on this sample at 400°C, 500°C and 600°C set T , in air. They are shown in figure 3.27. The effects observed are typical but rather small. The voltage evolves into a steady state much more quickly than on most of all the samples treated so far.

Summary of useful data and comparison

This subsection is the analogue to the last part of subsection 3.3.1 for titania and shows data for samples STO_001 (Pt grid) and STO_002b (Au grid) for 400°C and 500°C set T in air and N_2 .

Table 3.11: Useful data for STO samples.

	STO_001	STO_001	STO_001	STO_001	STO_002b	STO_002b	STO_002b	STO_002b
current collector	Pt	Pt	Pt	Pt	Au	Au	Au	Au
$T_{\text{set}}/^\circ\text{C}$	400	500	400	500	400	500	400	500
$p(\text{O}_2)/\text{bar}$	0.21	0.21	1×10^{-5}	1×10^{-5}	0.21	0.21	1×10^{-5}	1×10^{-5}
$U_{\text{dark}}/\text{mV}$	-180	-31	-230	-130	-180	15	-261	-74
U_{PV}/mV	-109	-1	-137	0	-563	-164	-529	-346
U_{batt}	320	57	385	160	313	51	298	121
U_{ss}/mV	306	56	370	159	-58	13	-299	-176
$U_{\text{batt}} - U_{\text{ss}}/\text{mV}$	14	1	15	1	371	64	-597	-297
$-(U_{\text{PV}} - U_{\text{ss}})/\text{mV}$	415	57	507	159	505	151	827	467

Measurements in $\text{H}_2/\text{H}_2\text{O}$ on STO_002b were all untypical, while they were not on STO_001. The results of the most interesting comparisons are listed below:

- U_{dark} was similar for STO_001 and STO_002b at 400°C set T in air and N_2 .
- U_{batt} was similar for STO_001 and STO_002b at 400°C set T in air and at 500°C set T in air and N_2 .
- In particular, the voltage U_{batt} in air is almost the same for both samples (different current collector materials), despite a massively different U_{PV} .

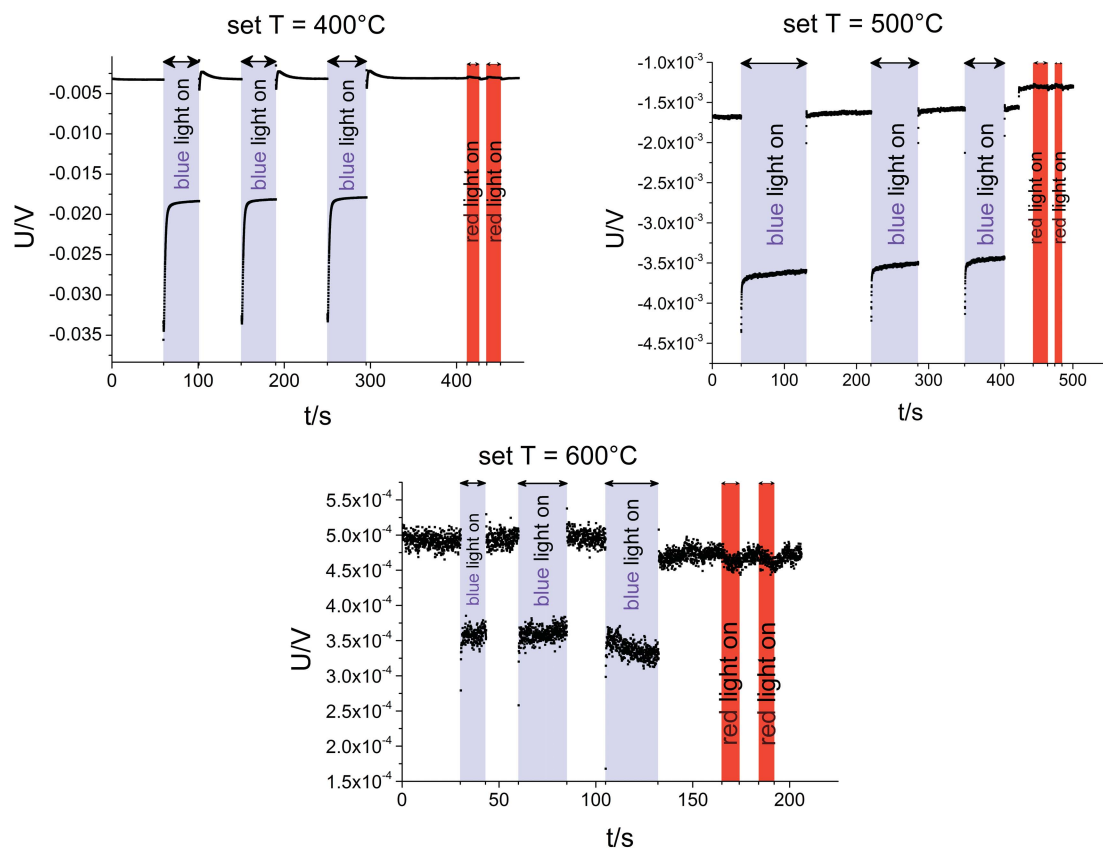


Figure 3.27: $U(t)$ measurements on sample YSZ_STF0.4_001 ($\text{SrTi}_{0.996}\text{Ti}_{0.004}\text{O}_{3-\delta}$ thin film electrode on YSZ) at different temperatures in air. A small but typical effect upon irradiation with blue light is visible.

- The fast jumps in voltage when the light is switched on or off, U_{PV} and $-(U_{PV} - U_{ss})$, are much bigger when the Au current collector was used (STO_002b).
- The voltage measured during illumination with blue light, U_{ss} , is smaller than U_{dark} on STO_002b but greater than U_{dark} on STO_001.

The absolute values of all voltages decrease with increasing temperature.

3.3.3 Comparison of STO samples (s.c. WE) with TiO₂ samples

By comparing STO and TiO₂ samples we get further general information about the interaction of light with MIECs. The measurements on the two materials only have one point in common without restriction: All voltages decrease with increasing temperature on all samples. For other comparisons we have to take a closer look:

- Under the same conditions the voltage offset U_{dark} is smaller for titania samples.
- On the titania samples Au as a current collector material seemed to enhance the offset voltage. This was not observed on the STO samples.
- On the titania samples U_{batt} was smaller than on STO at 400°C set T in air and at 500°C set T in N₂. At 500°C in N₂, however, the results for U_{batt} were comparable.
- Under certain conditions on both samples U_{batt} is similar for samples with varying U_{PV} (either randomly or induced by different current collector materials).
- In H₂/H₂O U_{batt} was practically zero for the titania samples, which was not always the case for the STO samples.

3.4 Systematic impedance measurements

3.4.1 Titanium dioxide

Impedance spectra without illumination

Typical impedance spectra of samples with TiO₂-WE having a nominal film thickness of 100 nm measured in air are shown in figure 3.28. Spectra on samples with three different geometries (see table 3.6) are displayed. The left column of figure 3.28 shows a spectrum measured on a sample with circular microelectrodes and a grid-shaped current collector. Measurements on pyramid-type WEs (Pt circle ($\varnothing = 200 \mu\text{m}$) on top of a TiO₂ circle ($\varnothing = 300 \mu\text{m}$)) are shown in the middle column of this figure. The right column depicts data collected on Pt microelectrodes ($\varnothing = 300 \mu\text{m}$) for comparison.

The spectra show a high-frequency semi-circle, one or two mid-frequency features and the onset of a low-frequency semi-circle. This description applies to spectra measured on samples with geometries no. 2 (lid), 3 (hat), 4 (pyramid) and 6 (micro-circle with grid), as well as on pure Pt circles. The preparation conditions varied (2 h/900°C for geometries 2, 3 and 4, vs. 2 h/550°C for geometry 6) and also the equilibration times were different, but qualitatively these features can be distinguished on all types of samples. The shape of the mid- and low-frequency features vary with geometry: On a circular microelectrode with grid (figure 3.28 (a)) there is a pronounced hump followed

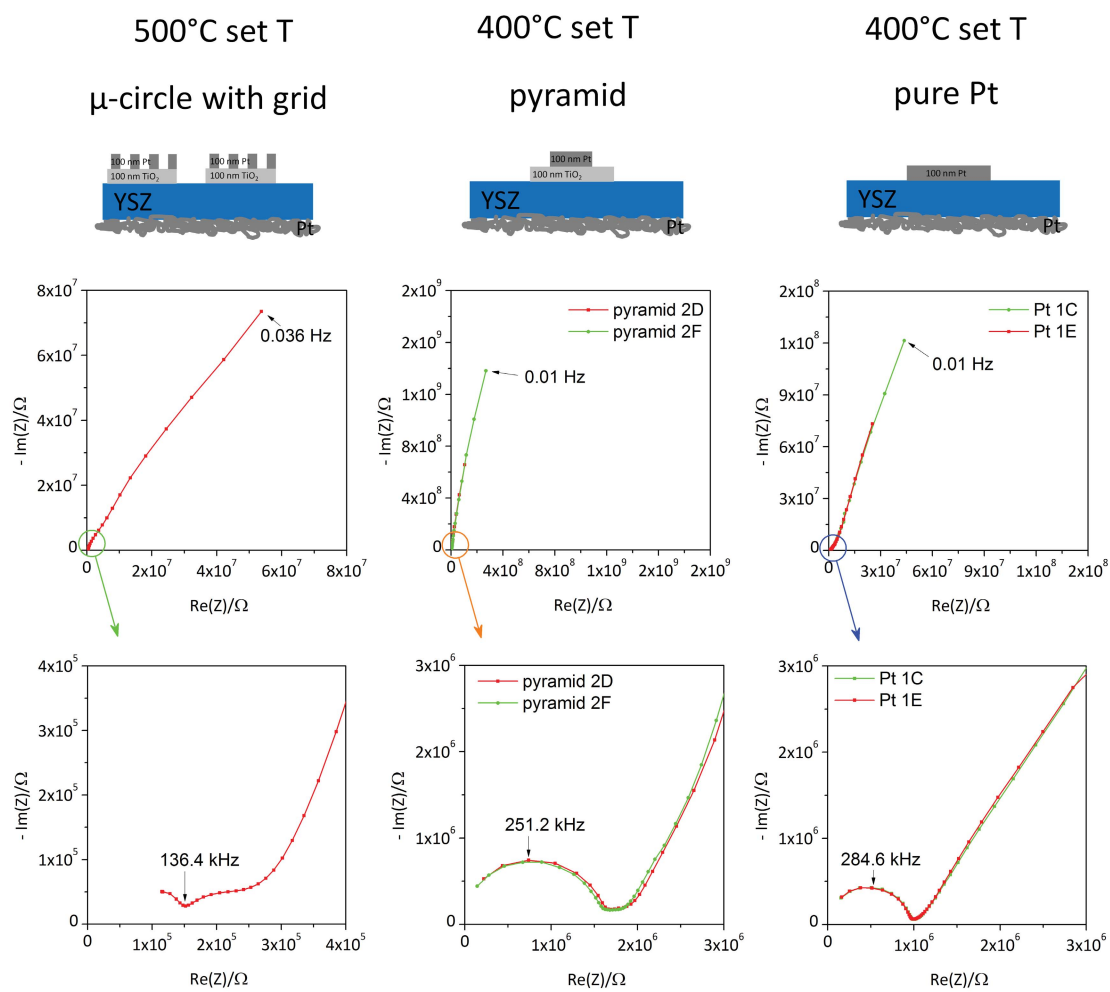


Figure 3.28: Typical impedance spectra of samples with a titania thin film working electrode in air compared to Pt electrodes. Left column: micro-circles with grid, middle column: pyramid-type electrodes, right column: Pt electrodes. For the Pt and pyramid-type electrodes two spectra, measured on two different electrodes, are shown. The bottom row shows the same measurements as the spectra in the middle row, but zooms in on the high-frequency region.

by a shoulder. On a pyramid-type electrode (figure 3.28 (b)) there is no hump but almost a straight line between the high frequency semi-circle and the other features at lower frequency. The mid-frequency shoulder is visible, though. The Pt spectrum is shaped as known from literature [134] with only one mid-frequency feature, which is a small shoulder.

High-frequency semicircle Usually, this semi-circle is attributed to the spreading resistance, R_{spr} , in the YSZ substrate [140, 141]. It can be calculated according to

$$R_{spr} = \frac{1}{2d_{me}}\sigma_{YSZ} \quad (3.4)$$

with d_{me} being the micro-electrode diameter and σ_{YSZ} the conductivity of the YSZ substrate [142]. A fit with an R||CPE (CPE... constant phase element) equivalent circuit and use of formula 3.4 with the known electrode diameter yields the YSZ conductivity.

While determining the active area relevant for the YSZ feature in the spectrum is straightforward for lid- and hat-type electrodes (the complete area; see figure 3.6 on page 58, geometries 2 and 3) it is more difficult for the pyramid-type Pt/TiO₂ electrodes. The lateral conductivity in the electrode is crucial for the size of the active area and therefore influences the parameters extracted from the fit. If the conductivity is too small the outer parts of the electrode will not be affected by potential changes during the EIS measurement and the parts of the YSZ lying underneath cannot be polarized, leading to an apparently lower YSZ conductivity. The Pt layer forming the top of the pyramid is laterally highly conductive. The lateral conductivity of the TiO₂ layer can be estimated from defect chemical calculations based on [78] and [85] presented in subsection 1.1.4 and also from impedance measurements as is shown in the following.

According to equation 3.4 the electrode diameter can be calculated if the conductivity and the resistance are known. The conductivity of the substrates used was determined in [143, pp. 48,68,89], the resistance was measured here. In order to obtain the conductivity from [143] the temperature is needed. It can be estimated from EIS measurements on Pt microelectrodes for which the active diameter is known (the whole electrode area). This was done on two different samples, the results are given in tables 3.12 and 3.13, in the top parts. The calculated temperatures of around 360°C are reasonable values for 400°C set temperature.

The mean temperature calculated from several measurements was inserted into equation 3.4 for the pyramid-type electrodes and the electrode diameter was computed. The results are shown in the bottom parts of tables 3.12 and 3.13. All active electrode diameters obtained for the pyramid-type electrodes are below 200 µm, which was the minimum active diameter assumed. Therefore, it is concluded that this type of electrodes does not show enough lateral conductivity in the titania layer to polarize a YSZ area bigger than 200 µm in diameter. The deviation of the calculated diameter values from the ideal value of 200 µm is attributed to variations in temperature which is very plausible because thermal contact to the furnace can vary between measurements. It is worth mentioning that oxygen ion conductivity in the titania or Pt layers is not necessary to polarize the YSZ substrate. Even with a completely ion-blocking electrode the YSZ semi-circle can be measured.

To further support the assumption of only the Pt part of a pyramid-type electrode being active the resistance for a current flowing from the Pt circle to the outer edge of the

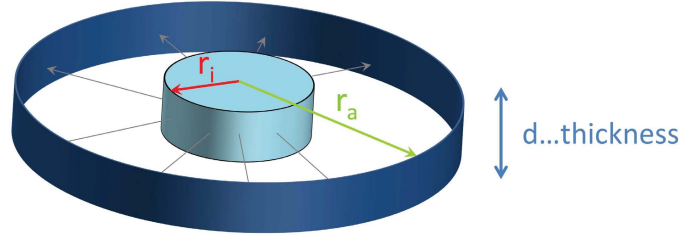


Figure 3.29: Sketch of the simplified geometry used to determine the lateral resistance in a pyramid-type electrode. The current is assumed to flow radially (along the arrows) from the inner cylinder (light blue) to the ring coloured dark blue.

titania circle was estimated. The conductivity σ was calculated from the model based on [78] and [85] (see subsection 1.1.4) for 360°C and air (21% oxygen at 1 bar). The geometry factor was calculated using a simplification: The volume in TiO_2 beneath the Pt circle was assumed to have no resistance, then current only flows laterally (see figure 3.29).

In the general formula

$$dR = \frac{1}{\sigma} \cdot \frac{dr}{A} \quad (3.5)$$

the area A is the "shirt cuff"-like surface coloured blue in figure 3.29 which depends on the radius r and is calculated according to

$$A = 2r\pi \cdot d \quad (3.6)$$

with d denoting the thickness of the titania layer. Integration from the radius of the Pt circle (r_i , 100 μm) to the radius of the titania circle (r_a , 150 μm) gives the resistance for a current flowing from the "inner shirt cuff" to the "outer shirt cuff":

$$\int_0^R dR = \int_{r_i}^{r_a} \frac{1}{\sigma} \cdot \frac{dr}{2r\pi \cdot d} = \frac{1}{\sigma 2\pi d} \int_{r_i}^{r_a} \frac{1}{r} dr = \frac{1}{\sigma 2\pi d} (\ln r) \Big|_{r_i}^{r_a} \quad (3.7)$$

$$R = \frac{1}{\sigma 2\pi d} \left(\ln \frac{r_a}{r_i} \right) \quad (3.8)$$

Inserting the numbers yields a resistance of $4.6 \times 10^{11} \Omega$, which is practically insulating. Even if the "outer shirt cuff" were at a distance of only $\frac{1}{2} \mu\text{m}$ from the assumed well-conducting zone beneath the Pt circle ($r_a = 0.5 \mu\text{m}$) the resistance would still be $5.6 \times 10^9 \Omega$.

The lateral resistance even increases when the simplification is omitted and the inner zone is allowed to be resistive. This resistance can be estimated assuming a cylindrical current path beneath the Pt circle,

$$R = \frac{1}{\sigma} \frac{d}{r_i^2 \pi}, \quad (3.9)$$

and has a value of around $2 \times 10^6 \Omega$, which is also considerable. Therefore, neglecting lateral current in the titania circle is a reasonable assumption.

Table 3.12: Estimations of temperature and active electrode diameter of electrodes on sample YSZ_Ti-Pt-Kreise_005. Top part of the table: Calculation of T from R_1 on Pt electrodes. Bottom part: Calculated T was used to estimate active electrode diameter on pyramid-type electrodes (details see text).

electrode name	R_1/Ω	conductivity/ $S\text{cm}^{-1}$	electrode diameter/ μm (given)	$T/^\circ\text{C}$ (calculated)
Pt 1C	7.25×10^5	2.3×10^{-5}	300	364.0
Pt 1C alt. meas.	9.71×10^5	1.71×10^{-5}	300	354.8
Pt 1E	9.61×10^5	1.73×10^{-4}	300	355.1
mean temperature = 359.4°C				
electrode name	R_1/Ω	conductivity/ $S\text{cm}^{-1}$	electrode diameter/ μm (calculated)	$T/^\circ\text{C}$ (mean value from above)
Tof 2D	1.65×10^6	1.99×10^{-5}	152.3	359.4
Tof 2F	1.58×10^6	1.99×10^{-5}	159.5	359.4

Table 3.13: Estimations of temperature and active electrode diameter of electrodes on sample YSZ_Ti-Pt-Kreise_006. Top part of the table: Calculation of T from R_1 on Pt electrodes. Bottom part: Calculated T was used to estimate active electrode diameter on pyramid-type electrodes (details see text).

electrode name	R_1/Ω	conductivity/ $S\text{cm}^{-1}$	electrode diameter/ μm (given)	$T/^\circ\text{C}$ (calculated)
Pt 2E	8.97×10^5	1.86×10^{-5}	300	357.3
Pt 2F	8.49×10^5	1.96×10^{-5}	300	358.0
mean temperature = 358.1°C				
electrode name	R_1/Ω	conductivity/ $S\text{cm}^{-1}$	electrode diameter/ μm (calculated)	$T/^\circ\text{C}$ (mean value from above)
Tof 3A	1.58×10^6	1.91×10^{-5}	166.1	358.1
Tof 3B	1.32×10^6	1.91×10^{-5}	197.9	358.1

Table 3.14: Comparison of the extrapolated R_{DC} for various types of Pt(/TiO₂) samples.

electrode type	T_{real} °C	extrapolated R_{DC}/Ω	R_{DC}/Ω (corrected if necessary) for comparison
Pt ref. [134]	350		1×10^9
Pt ref. [134]	450		4×10^8
Pt this study	350	1×10^9	2.25×10^9
hat	350	1×10^9	2.25×10^9
lid	350		$2.5 \dots 5 \times 10^9$
pyramid	350		1.5×10^{10}
μ -circles with grid	450	6×10^8	1.2×10^9

Mid-frequency feature In the mid-frequency range one or two features appeared. A slight shoulder next to the onset of the low-frequency arc could be observed on all samples. The hump-shaped feature, which appears at higher frequencies than the shoulder, is most pronounced on circular micro-electrodes with current collector grid. It can be identified on pyramid-shaped electrodes as well, but it is certainly smaller. On hat-type electrodes and Pt electrodes this feature did not occur. This suggests that it is connected to the TiO₂ layer. The hat-type electrodes are a mixture between Pt electrodes and TiO₂/Pt electrodes since they have a zone where Pt touches YSZ. It can also be concluded that this phenomenon depends on the electrode geometry. Giving further interpretations about its origin is beyond the scope of this work.

Low-frequency arc The low-frequency arc is usually assigned to the oxygen exchange reaction on the electrode surface [140, 141, 144–146]. The consistency between spectra measured on different samples and geometries within this group of samples and compared to literature was assessed by fitting the beginning of the low frequency arc with an R||CPE element and extrapolating it to the intercept with the abscissa (R_{DC}). Apart from circular Pt electrodes ($\varnothing = 300 \mu\text{m}$) the following Pt/TiO₂ electrode types (cf. table 3.6) were included in the analysis: pyramid-type electrodes, hat-type electrodes (outer $\varnothing = 300 \mu\text{m}$, inner $\varnothing = 200 \mu\text{m}$), lid-type electrodes ($\varnothing = 200 \mu\text{m}$) and circles ($\varnothing = 300 \mu\text{m}$) with current collector grid. Only the last type of electrodes was measured at 500°C set T , the rest was investigated at 400°C set T . Literature data was taken from figure 10 (a) of reference [134].

The fit quality can be judged from figure 3.30. It is acceptable for pyramid-type Pt/TiO₂ and Pt electrodes. The low-frequency arc of hat- and lid-type electrodes as well as circular microelectrodes with Pt grid cannot be described with an R||CPE element very well. This indicates that the surface exchange process might be complex and geometry-dependent. Nevertheless this extrapolation is enough for the rough comparison that this subsection aims at since it would require further investigations to find a meaningful equivalent circuit for the samples under consideration, which would take us beyond the aims of this study.

A comparison of the extrapolated R_{DC} values measured in this study (see table 3.14) reveals that Pt and hat-type electrodes have a very similar R_{DC} . The lid-type electrodes were smaller in diameter but can be compared to Pt and hat-type electrodes if this size difference is taken into account. Since in the investigated temperature regime a current

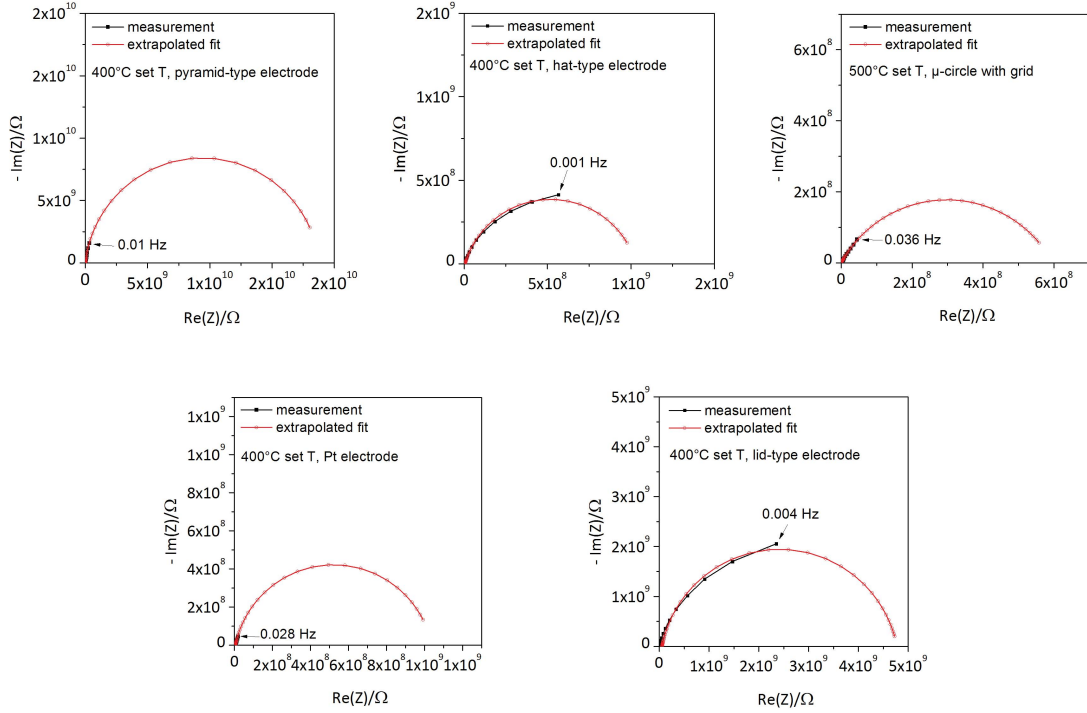


Figure 3.30: Examples for extrapolated fits of the low-frequency arc of different Pt/TiO₂ sample types. All measurements were carried out in air.

path through the electrode bulk is predominant [134] R_{DC} for hat-type and Pt electrodes was multiplied by a factor of

$$\frac{\text{Area (hat)}}{\text{Area (lid)}} = \frac{150^2 \pi}{100^2 \pi} = 2.25, \quad (3.10)$$

which results in an R_{DC} value of about $2.25 \times 10^9 \Omega$, agreeing very well with values for lid-type electrodes ($\approx 2.5 \dots 5 \times 10^9 \Omega$). As was shown above, the active electrode area on pyramid-type electrodes is $200 \mu\text{m}$ and therefore did not have to be corrected. The value is about $1.5 \times 10^{10} \Omega$ which is higher by a factor of ≈ 7 compared to the other electrode types, but within the order of magnitude. It suggests that this geometry has an influence on the rate-determining step in the oxygen exchange reaction.

The R_{DC} value for a Pt electrode taken from [134] at 350°C is approximately $1 \times 10^9 \Omega$ for a microelectrode with a diameter of $200 \mu\text{m}$ and is in good agreement with the value of $2.25 \times 10^9 \Omega$ measured in this study.

Assessing the agreement between the extrapolated R_{DC} on TiO₂ microelectrodes with Pt grid (500°C) and pure Pt microelectrodes measured in [134] (where it was $\approx 4 \times 10^8 \Omega$) requires another correction. In the light of the conductivity considerations from above, it must be assumed that on a sample with Pt grid only the area covered by the grid is active for oxygen exchange. The grid used had stripes with a width of $15 \mu\text{m}$, separated by $35 \mu\text{m}$ of void. This gives a surface coverage of 51% that has to be taken into account. The corrected R_{DC} value is $1.2 \times 10^9 \Omega$, again in good agreement with literature.

The present results at 400°C set T deviate from the literature values by a factor of up to five for the majority of the electrode types, including pure Pt electrodes, or 15 for pyramid-type electrodes. At 500°C the deviation is roughly a factor of three. This acceptable compliance is a strong indication for the absence of major artefacts.

From this comparison, but more importantly, from the comparison between Pt and Pt/TiO₂ electrodes measured in this study, it can be concluded that the titania layer does not inhibit the oxygen exchange reaction greatly despite its low conductivity. However, the inaccurate fit of the low-frequency arc by an R||CPE, which is in contrast to [134], indicates a change in mechanism induced by the insertion of the TiO₂ layer.

Impedance spectra with illumination

Sample series 1 EIS measurements under illumination with red and blue light were carried out on samples with titania layers produced by oxidation of sputtered Ti films at 900°C for 2 h in air. Lid-, hat- and pyramid-type geometries were used. The measurements can be described in three groups. The first group deals with spectra recorded with blue light using the usual EIS setup. As the Novocontrol impedance analyzer short-circuits the sample during measurement, a current flow is possible [134]. If this is the case, the impedance is not probed in the origin of the current-voltage curve of the electrode under investigation but in another point. Then, the impedance can be different if the U - I curve is non-linear. To avoid this, the second group of measurements was performed using a capacitor, inserted into the lead between one of the sensing terminals and the sample in a pseudo-4-point arrangement. This method was described in more detail in [134]. Finally, the third group of measurements consists of miscellaneous investigations that should complete the picture of EIS with light on sample series 1.

The electrodes belonging to group 1 are: five lid-type electrodes on sample YSZ_Ti-Pt-Kreise_004, three hat- and two pyramid-type electrodes on sample YSZ_Ti-Pt-Kreise_005 and two hat- and two pyramid-type electrodes on sample YSZ_Ti-Pt-Kreise_006. On each electrode a measurement without light and with blue light was performed. Measurements with red light were carried out on one sample for at least one type of geometry. An overview of typical results is given in figure 3.31. The findings are similar for all three types of geometries. Red light had almost no effect, except for a small shift in the high-frequency semi-circle. By the same method as in subsection 3.4.1 this can be related to a change in YSZ spreading resistance, most likely caused by a slight change in temperature, which can be estimated to be a few degrees celsius. The same effect is caused by illumination with blue light but additionally, the estimated extrapolation of the low-frequency feature to the abscissa, R_{DC} , decreases by about one to two orders of magnitude. Also, a second low-frequency feature appears with blue light. This new element is hump-shaped rather than semi-circle-like. No change was observed in the mid-frequency part of the spectrum.

The measurements assigned to group 2 were performed on the same samples and electrodes as the ones in the group above, but not on all of them. The electrodes probed were two hat-type and two pyramid-type electrodes on sample YSZ_Ti-Pt-Kreise_005 as well as on sample YSZ_Ti-Pt-Kreise_006. It was already shown in the above measurements that red light has no significant effect. The capacitors blocking the DC current

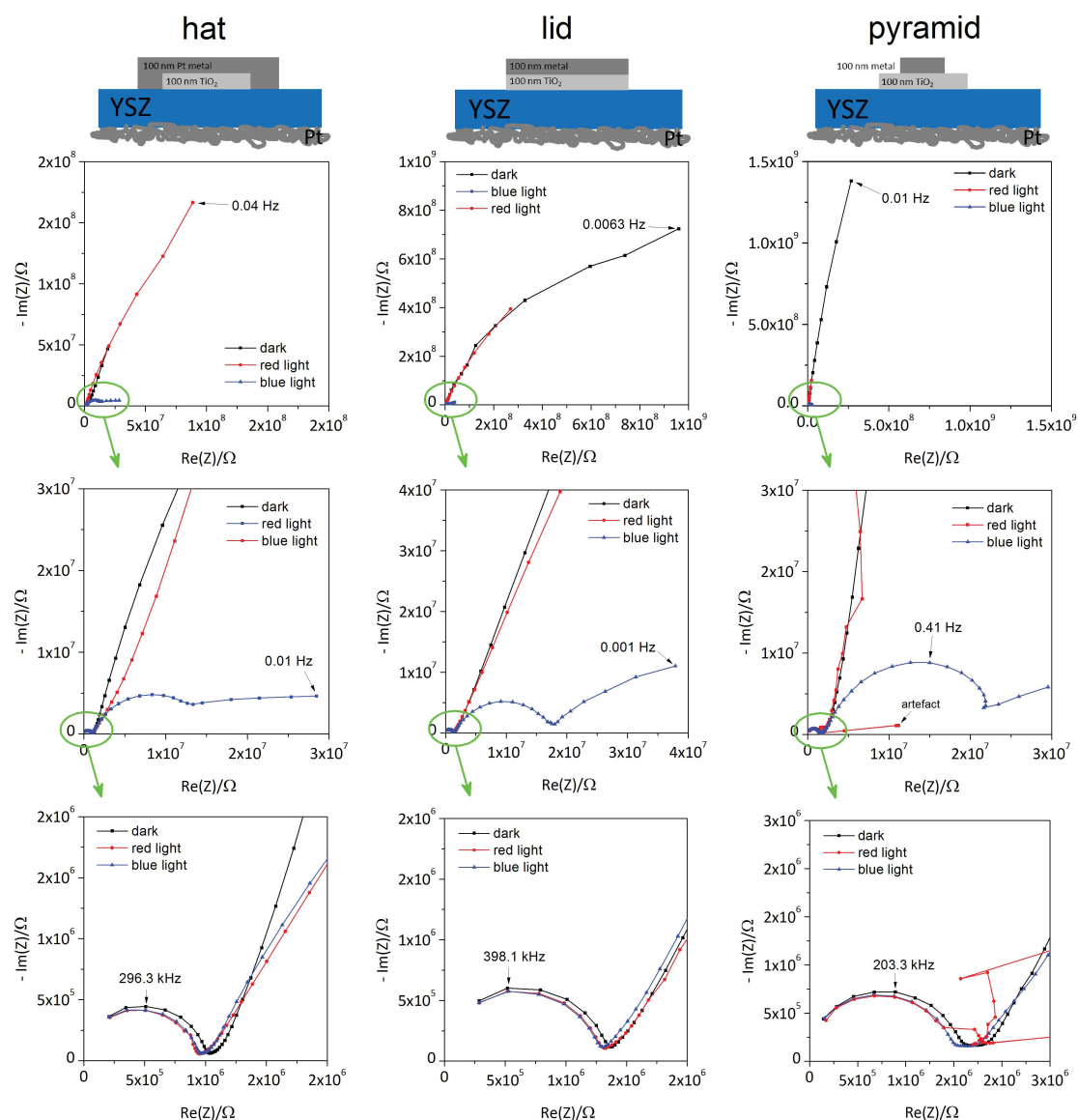


Figure 3.31: Typical EIS measurements (group 1, no DC-blocking capacitor) with blue, red and without light, carried out at 400°C set T in air. The cell was short-circuited by the impedance analyzer during the measurement, leading to a current flow when blue light was turned on. Every column contains the same data: An overview (first row) and two zooms to higher frequencies (second and third row).

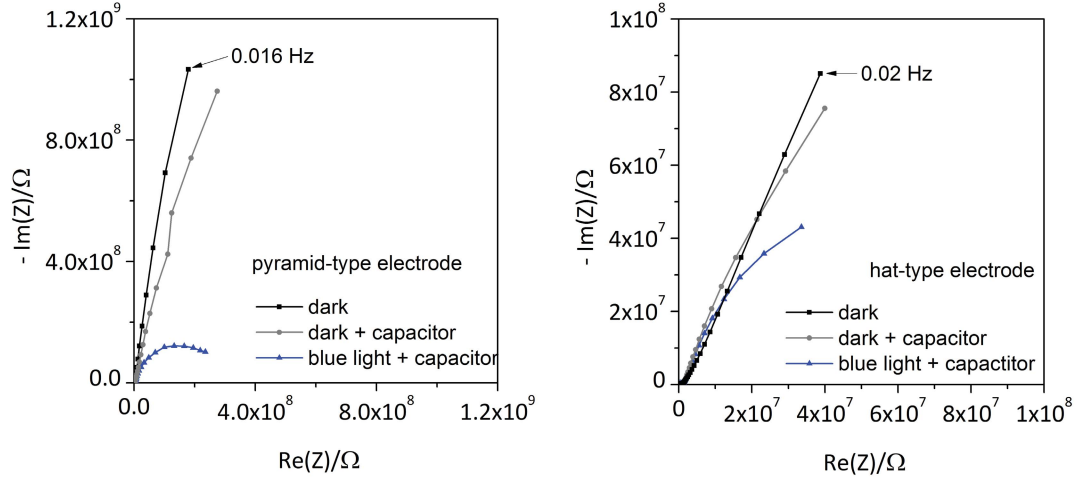


Figure 3.32: Typical EIS measurements (group 2: DC-blocking capacitor) with blue, red and without light, performed at 400°C set T in air. With blue light and the DC-blocking capacitor an effect is visible, but smaller than without the capacitor (group 1 samples, figure 3.31).

were charged by completing the circuit that connects sample, impedance analyzer and capacitor (Novocontrol Alpha A with POT/GAL interface in "connect" mode). The sample acted as a voltage source providing voltage U_0 that charged the capacitor up to a certain degree U/U_0 , where U is the voltage at the capacitor at time t . The ratio $U/U_0 = 99\%$ was chosen to be sufficiently high. The time necessary to charge the capacitor with capacitance C and the sample acting as a resistor with resistance R (known from the extrapolated EIS measurement) was calculated from the $U(t)$ dependence during charging a capacitor

$$U = U_0 \left[1 - \exp\left(-\frac{t}{RC}\right) \right] \Rightarrow t = -RC \ln\left(1 - \frac{U}{U_0}\right). \quad (3.11)$$

Since the capacitor represents a high pass filter the cutoff frequency f_c had to be determined using

$$f_c = \frac{1}{2\pi RC}. \quad (3.12)$$

The selected C values of 10 nF or 100 nF gave a cutoff frequency in the 1-10 mHz range and a charging time of around 10 min. The effect of the capacitor on a measurement without light was tested at least once for each sample and was judged to be insignificant, see figure 3.32. This figure also shows the effect of blue light on the impedance spectrum, which was similar for all electrodes. R_{DC} was again estimated by extrapolation and was found to be $\frac{1}{2}$ to a bit more than 1 order of magnitude lower than without illumination. In the other parts of the spectrum the changes were similar to the measurements without capacitor.

To check if the capacitor had the desired DC-blocking effect the inhibition of direct current flow was brought about by another means as well: A voltage equal in absolute value but opposite in sign to the measured photovoltage was applied during a measurement with blue light. This test was carried out on one electrode only but yielded the

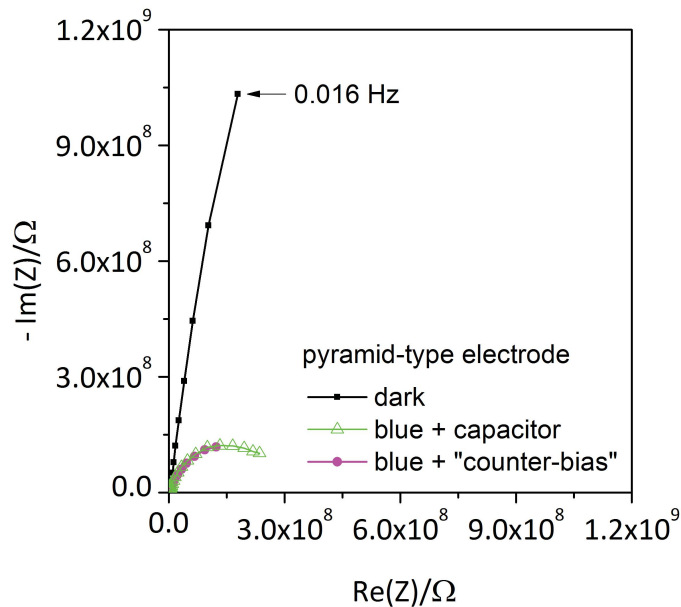


Figure 3.33: Impedance spectra of a pyramid-type electrode (400°C set T in air) without light (steepest arc), with blue light and DC-blocking capacitor as well as with blue light and "counter-bias" (identical - smaller arcs).

expected result: Impedance spectra with capacitor and with "counter-bias" are identical (see figure 3.33). These findings suggest that the current flowing during illumination contributes in conjunction with a non-linear current-voltage curve to the observed decrease in resistance.

Therefore, the effect of bias without light was investigated as well to further support the hypothesis of resistance decrease by bias on a non-linear current-voltage curve. The voltage produced by the cell during illumination with blue light was known from $U(t)$ measurements and so a bias voltage with the same value and sign could be applied to the electrodes during impedance spectroscopy. The electrodes used were two hat-type and two pyramid-type electrodes on sample YSZ_Ti-Pt-Kreise_005 and also on sample YSZ_Ti-Pt-Kreise_006, typical results are shown in figure 3.34. The impedance decreases with bias which supports the assumption of non-linear current-voltage behaviour. Finally two Pt electrodes were measured during illumination with blue and red light, results of both samples are shown in figure 3.35. There is no effect on the low- and mid-frequency features either by red or blue light. As for the other types of electrodes, the high-frequency semi-circle decreases slightly in diameter, most probably due to heating by light.

Three pyramid- and three hat-type electrodes on two samples were inspected under the optical microscope before and after each type of measurement (light, bias...). On four of them none of the measurements changed the surface visibly except for the measurement with blue light and without the capacitor (see figure 3.36). After the measurement it looked rough. On two samples no optical change was observed. There was no pre-

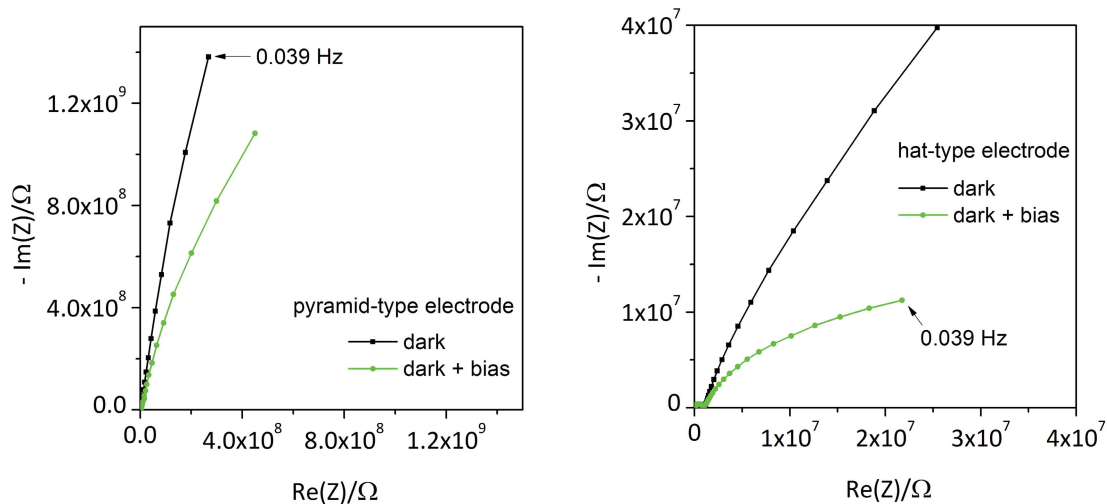


Figure 3.34: Typical EIS measurements with and without bias, measured at 400°C in air.

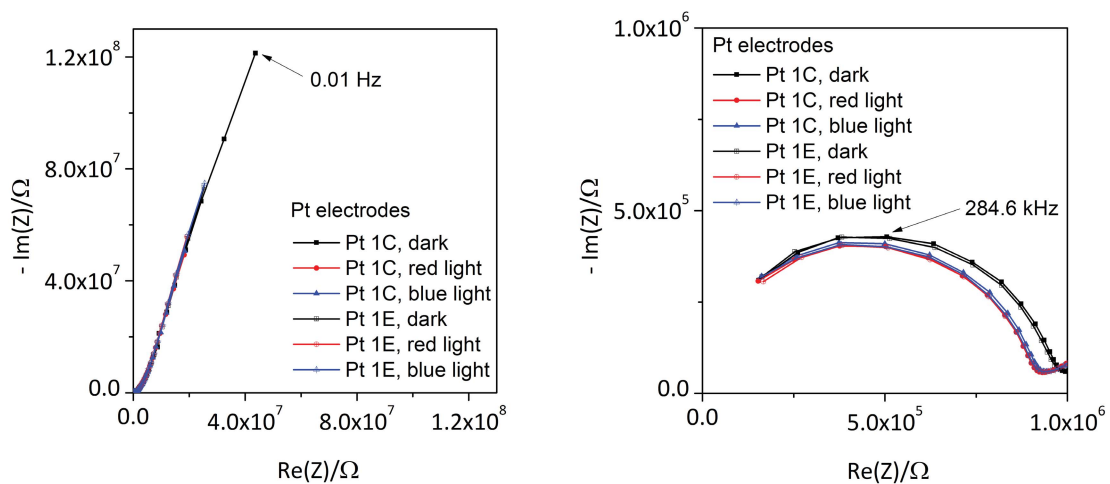


Figure 3.35: No significant light effect on Pt electrodes (400°C, air). Data from two different Pt electrodes on sample YSZ_Ti-Pt-Kreise_005 are shown, each in darkness as well as under red and blue light (in both diagrams). The right panel is a zoom on the high-frequency part. The small change in the high-frequency feature is attributed to heating by a few °C.

sample YSZ_Ti-Pt-Kreise_006, electrode ToF 3A (pyramid-type)

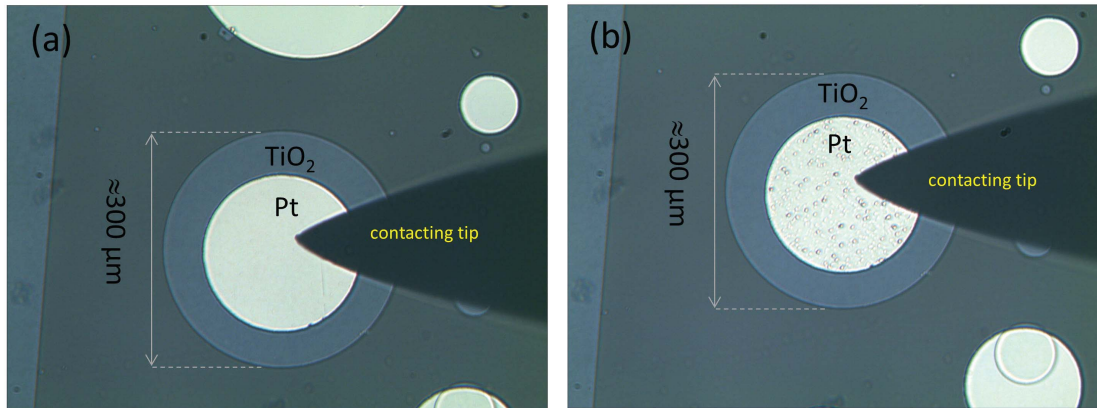


Figure 3.36: (a): Pyramid-type microelectrode before measurement with blue light under short-circuit conditions. The surface looks smooth. (b): The same electrode after the measurement. The surface looks rough.

ferred geometry for the appearance of this effect. The reason for the surface becoming rough after measuring with blue light could be an anodic current that causes bubble formation upon excorporation of oxygen. This phenomenon was studied in detail in [147]. The direction of the current implies that in the electrode process electrons have to be transferred from oxide ions to the cable. This is in agreement with the sign of the voltage usually measured during illumination with blue light: It was negative (with terminal + on the voltmeter connected to the electrode, see figures 3.14, 3.16, 3.17), indicating that electrons want to leave the electrode and go into the outer circuit. As shown in [147] the formation and cracking of bubbles leads to an increase in triple phase boundary length and hence to an increase in current, provided the preferred reaction path is via the triple phase boundary. So not only a kinetic light effect and a non-linear current-voltage curve but also this geometric phenomenon have to be considered as a contribution to the decreased impedance in the measurements with blue light under short-circuit conditions.

While this conclusion is consistent in itself and in agreement with literature roughening was also observed on some electrodes that were not measured at all. Explaining this phenomenon, however, would result in speculation.

Sample series 2 This series of samples contains the already mentioned samples Pt 009 to Pt 012 (circular microelectrodes with Pt current collector grid, 500°C set T). Measurements were performed in air, N_2 and H_2/H_2O . Measurements both with DC-current-blocking capacitor and without were carried out.

In air measurements on only two of the four samples could be evaluated because of noise. Another reason to exclude a sample from analysis was strong disagreement between dark measurements with and without capacitor. On both remaining samples a slight decrease in impedance was observed upon illumination with blue light, regardless of the capacitor's presence (see figure 3.37). In N_2 an effect with blue light only occurred on one sample out of four, so it has to be classified as untypical and no reaction to light is the conclusion.

In H_2/H_2O one sample had to be excluded because there was a difference between

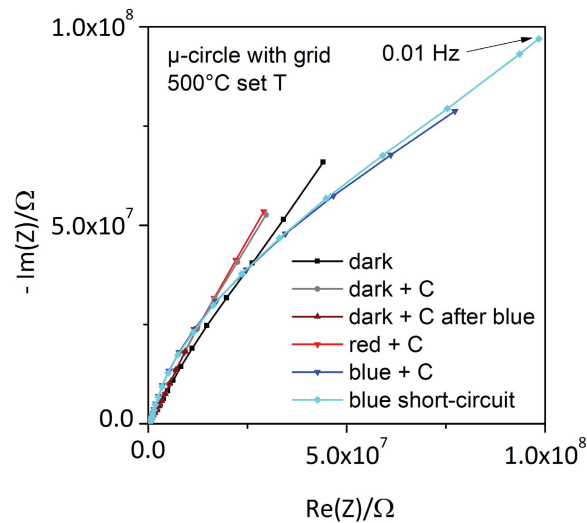


Figure 3.37: EIS measurements on sample Pt 010 (micro-circle with Pt grid, 500°C set T , air) with and without light. A slight change can be observed with blue light, no matter if the capacitor C was used or not (blue and light blue curves).

measurements with and without capacitor. The other samples showed no effect.

3.4.2 Strontium titanate

EIS measurements were done on both samples with a thick, single crystalline WE and thin film YSZ electrolyte (STO_001 with Pt, STO_002b with Au current collector grid).

Impedance spectra without illumination

Figure 3.38 shows an impedance spectrum measured on sample STO_001 after it had been subject to 6 h of heat treatment at 450°C set T followed by firing at 700°C in the measurement heating stage and subsequent dwelling back at 450°C set T in order to bring it into a state near equilibrium with the surrounding air. Three features can be identified: A high-frequency semi-circle, a small mid-frequency shoulder and the onset of a big low-frequency feature. As will be shown in the following subsection it was most interesting to study the time evolution of impedance spectra after the blue light had been switched on. This was only possible on an impedance analyzer with high measurement speed (HP 4192A), where one measurement only took about 20 s or less. This machine, however, can only measure frequencies in the range of 13 MHz to 5 Hz. Under these conditions only the high-frequency feature can be recorded and so the interpretation of all impedance spectra focusses on the high-frequency semi-circle. A typical impedance spectrum measured on STO_002b (with the HP 4192A Impedance Analyzer and therefore no mid- and low-frequency data) is shown in figure 3.39. One semi-circle is clearly visible.

The high-frequency arc can be fitted with an $R||CPE$ equivalent circuit very well on both samples (figure 3.40). To assign this feature to a material or process the capacitance was

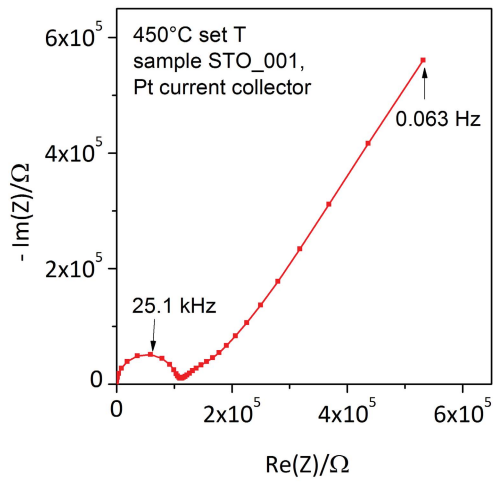


Figure 3.38: EIS measurement on sample STO.001 (Pt current collector) after heat treatment leading to better equilibration.

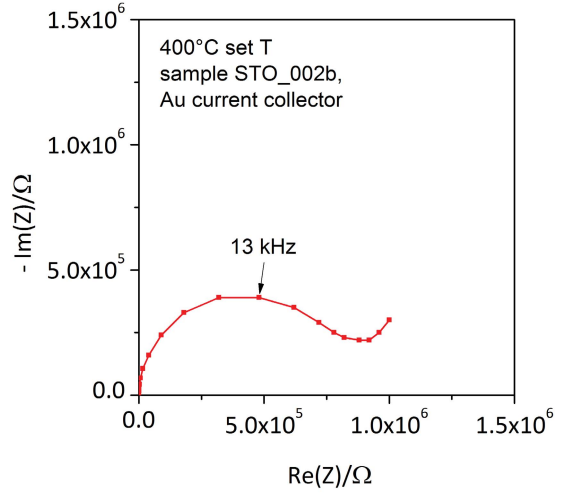


Figure 3.39: EIS measurement on sample STO_002b (Au current collector).

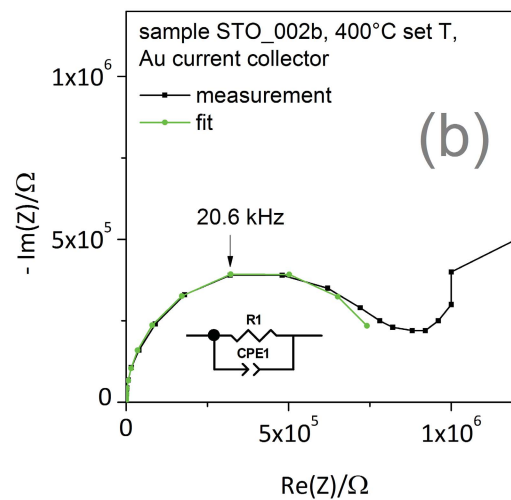
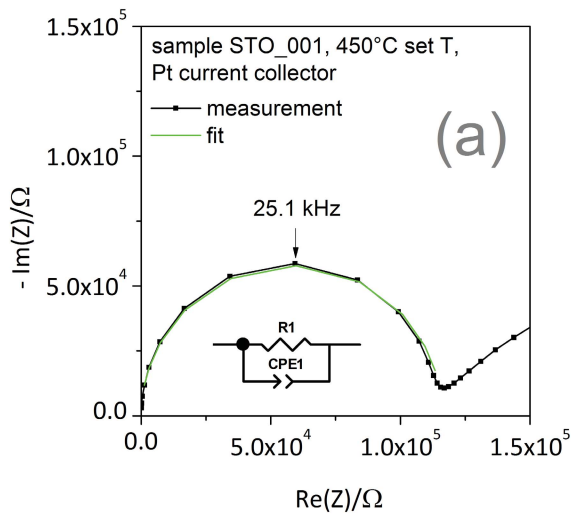


Figure 3.40: Impedance spectra (high-frequency part) measured on samples (a) STO.001 and (b) STO.002b including a fitted curve (R||CPE).

calculated from the fit parameters R , n and Q of the R||CPE circuit using the formula given in [148]:

$$C = \left(R^{1-n} \cdot Q \right)^{\frac{1}{n}}. \quad (3.13)$$

Results were approximately 5×10^{-11} F (STO_001, 450°C set T , air) and $8 \times 10^{-12} \dots 1.2 \times 10^{-11}$ F (STO_002b, at different T and $p(\text{O}_2)$). For comparison, literature values were computed assuming a parallel plate capacitor with STO as a dielectric:

$$C = \epsilon_0 \epsilon_r \frac{A}{d}. \quad (3.14)$$

The area A was the electrode area determined from optical microscope images by measurement in Zeiss' Axio Vision software or using Adobe Photoshop CS3. The relative dielectric constant ϵ_r was taken from [149]. ϵ_0 and d denote the electric field constant and the thickness of the sample, respectively. The obtained literature values were in the same order of magnitude as the measured ones: 1.1×10^{-10} F for STO_001 and 1.8×10^{-11} F for STO_002b.

From systematically recorded impedance spectra on STO_002b (400°C, 500°C and 600°C set T in air, N_2 and $\text{H}_2/\text{H}_2\text{O}$) more information about the high-frequency semi-circle can be obtained. Despite the fit quality being generally very good it was often necessary to exclude the first three or four data points at the highest frequency from the fit in order to obtain a good result. Ignoring the first few points is necessary because the HP 4192A Impedance Analyzer gives unreliable results at frequencies above 1 MHz [150].

The measured data were often close to an ideal capacitance (n often close to 1) which is expected for a homogeneous single crystalline material since the CPE usually represents a distribution of capacitance [148]. In some fits, however, n was even below 0.8, and it is not entirely clear why this should represent the same single crystalline material as the other, almost ideal capacitances. One reason for a non-ideal capacitance could be the inhomogeneous distribution of V_{O} during illumination, before a steady state is reached. Another reason could be a second process whose impedance feature overlaps with the high-frequency arc under consideration.

The measurement of the capacitance as a function of temperature (figure 3.41) gives further clues about its origin being dielectric or chemical. It decreases with increasing temperature, a typical behaviour for a dielectric capacitance (e.g. [151]) as opposed to a chemical capacitance which is dominated by the temperature behaviour of the charge carrier concentrations [152]. If the values are extrapolated to the measurement temperature of the literature value the agreement is even better.

In addition to the capacitance the conductivity associated with the high-frequency semi-circle was evaluated as a function of T and $p(\text{O}_2)$. The results for the temperature dependence are given in figure 3.42 as an Arrhenius plot. Apart from the band-band excitation and the surface exchange reaction the model given in literature includes also a trapping equilibrium:



Therefore, to perform any calculation the dopant concentration had to be chosen. It was assumed that the STO single crystal is p-doped by impurities and in equilibrium with the surrounding atmosphere at 550°C (see subsection 3.3.2, p. 69). Therefore, a value for the Fe dopant content was chosen that results in a calculated conductivity corresponding to the measured one at this temperature. Then, the measured data and

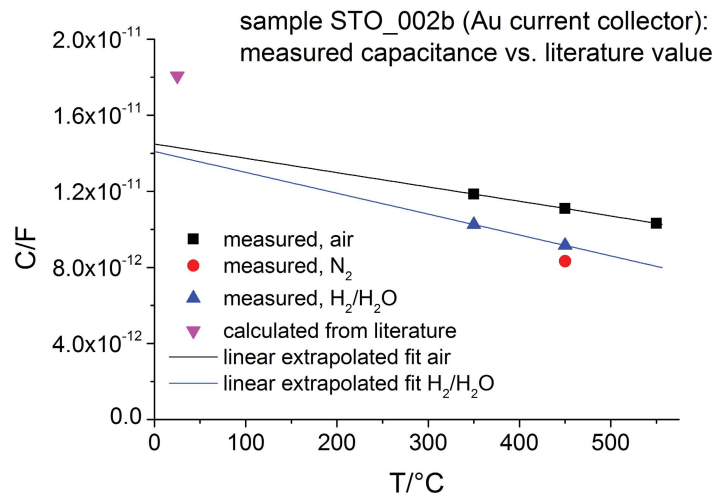


Figure 3.41: The capacitance C measured on sample STO_002b (Au current collector) as a function of temperature T , compared to a value calculated using ϵ_r from literature [149]. Three points are missing because no fit was possible due to noise. The agreement is good and gets even better when C is extrapolated to room temperature, where the ϵ_r from literature was measured.

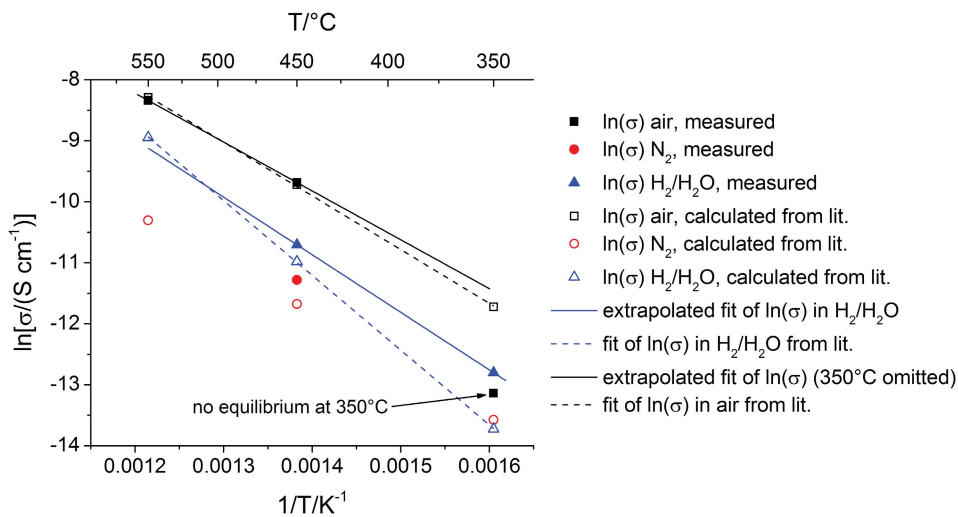


Figure 3.42: Arrhenius plot of conductivity extracted from the high-frequency semi-circle measured on sample STO_002b (Au current collector; full symbols) compared to data calculated from [92] (open symbols). A dopant concentration equivalent to 5×10^{17} Fe cm⁻³ was assumed. The deviation of the measured conductivity at 350 °C compared to the value calculated from literature suggests that no equilibrium could be reached at this temperature.

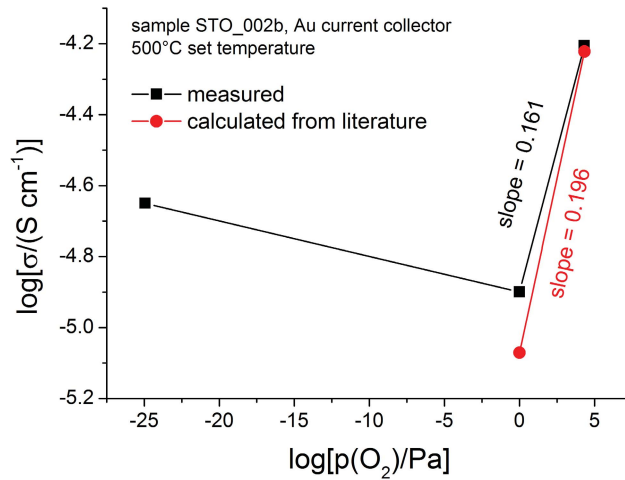


Figure 3.43: Dependence of conductivity on $p(\text{O}_2)$ measured on sample STO_002b (Au current collector). The values between $p(\text{O}_2) = 0.21$ Pa (air) and $p(\text{O}_2) = 1$ Pa (N_2) were joined by a straight line to evaluate the slope.

those from literature are of course identical for 550°C in air in figure 3.42. At 450°C in air the agreement of the conductivity data is still excellent. At 350°C the agreement is still overall acceptable, the values are not even half an order of magnitude apart (mind the ln on the y-axis). However, it is appropriate to exclude this point when calculating the slope for the data in air. Then, it is very close to the literature values. If the point at 350°C were included, this would alter the slope drastically and it would not be as comparable to the literature value as without this point. In $\text{H}_2/\text{H}_2\text{O}$ atmosphere only two points could be extracted by fitting the impedance data. The absolute values and also the slope agree very well with literature. However, the data point at 350°C is further away from the calculated value. In N_2 fitting the impedance data was only possible for one point, which is close to the calculated conductivity. It is interesting that the points at the lowest temperature, 350°C, seem to deviate the most from literature data. This could be due to the very sluggish equilibration kinetics at this low temperature (see subsection 3.3.2). At 550°C in air, however, the sample can be considered in equilibrium in these experiments. It is therefore justified to exclude the data point at 350°C from the calculation of the slope and to estimate the dopant concentration by using the data at 550°C.

The $p(\text{O}_2)$ dependence of conductivity is presented in figure 3.43. An evaluation was possible by comparing the slopes of measured and literature data between air and N_2 because in this partial pressure regime the conductivity is an almost linear function of $p(\text{O}_2)$. To do this, the two points at $p(\text{O}_2) = 0.21$ Pa and $p(\text{O}_2) = 1$ Pa were joined by a straight line. The literature value for the slope is close to $\frac{1}{5}$, the measured one is about 0.16, which is close to $\frac{1}{6}$. This difference could be simply caused by measurement errors, but also by different defect chemical reactions, which are determined by the unknown impurity dopant.

To sum up, the numerical values and also the temperature dependence of the capacitances extracted from the high-frequency semi-circle of the impedance spectra sug-

gest that the dielectric capacitance of STO was measured. The absolute values and the temperature dependence of the conductivity evaluated from the fitted impedance data agree very well with the total conductivity calculated from the model by Denk *et al.* [92], assuming an impurity dopant level of $5 \times 10^{17} \text{ cm}^{-3}$ and poor equilibration at 350°C. In contrast to this, the partial pressure dependence of the conductivity shows a slight deviation from the expected value (about $\frac{1}{6}$ instead of $\frac{1}{5}$). Nevertheless, the investigated high-frequency semi-circle can be assigned to the STO bulk with high probability.

Impedance spectra with illumination

Impedance measurements probing the influence of light were performed on both samples STO_001 (Pt current collector) and STO_002b (Au current collector). The analysis focussed only on the high-frequency arc. All impedance measurements were carried out without a DC-blocking capacitor.

On STO_001 the response of the impedance to light was investigated at 400°C set temperature in air with low time resolution (Novocontrol Alpha-A Impedance Analyzer with ZG-2 interface), on STO_002b it was measured in air, N₂ and H₂/H₂O at 400°C, 500°C and 600°C set temperature with high time resolution (HP 4192A Impedance Analyzer).

The results for STO_001 are shown in figure 3.44, panel (a) gives an overview. The large curve with the clearly visible semi-circle was measured without, the small curve barely discernible with blue light. The first enlargement (panel (b)) shows the high-frequency arc and its time evolution after first switching on red and then blue light. Red light causes almost no change, the feature only becomes a little smaller. Upon illumination with blue light, however, the semi-circle starts to decrease in diameter. For better visibility a second magnification is shown in panel (c). Since the semi-circle changes its size continuously, it can cause a loop in the measurement. After turning off the blue light it starts to increase in diameter and reaches a value near its starting point after a few measurements.

On STO_002b similar measurements, but with higher time resolution, are shown in figure 3.45. The effect of blue light is similar: When switched on, the high-frequency semi-circle starts to shrink, after switching off its diameter increases again.

This time dependence was investigated more closely by varying temperature and oxygen partial pressure. The STO impedance spectra were fitted with an R||CPE equivalent circuit and R_{STO} was then plotted as a function of time t when light was switched on and off. The resulting $R_{\text{STO}}(t)$ curves are plotted in figure 3.46.

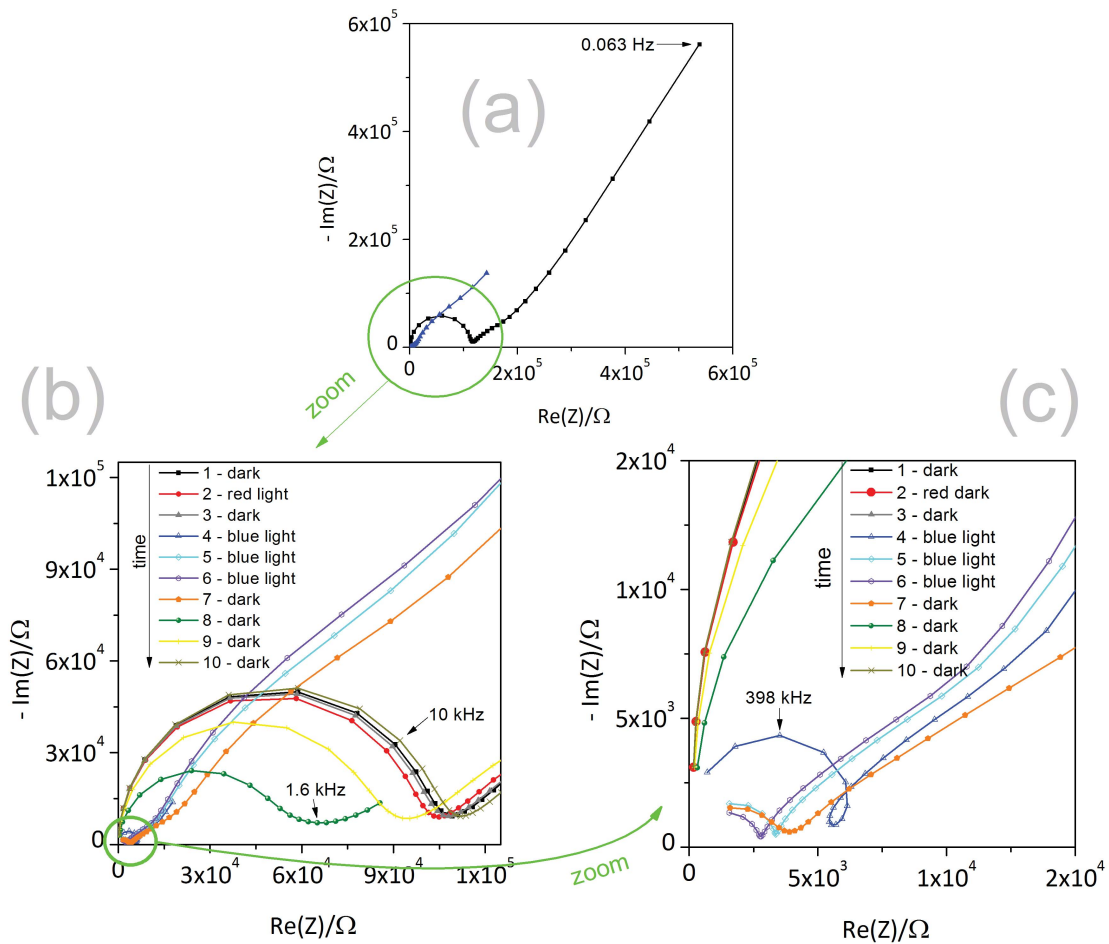


Figure 3.44: Impedance measurements on sample STO.002b (Au current collector) without and with blue light. (a): Overview. With blue light the impedance drops drastically. (b): Zoom to STO-semicircle without light. The numbers in the legend indicate the order in which measurements were carried out. With blue light the semicircle shrinks, after switching off it only re-grows slowly. (c): Zoom to STO semi-circle under illumination with blue light: When blue light is switched on the impedance decreases rapidly. Due to the comparatively slow measurement (\approx minutes) a loop appears in the spectrum. After switching off blue light the impedance increases towards its original value.

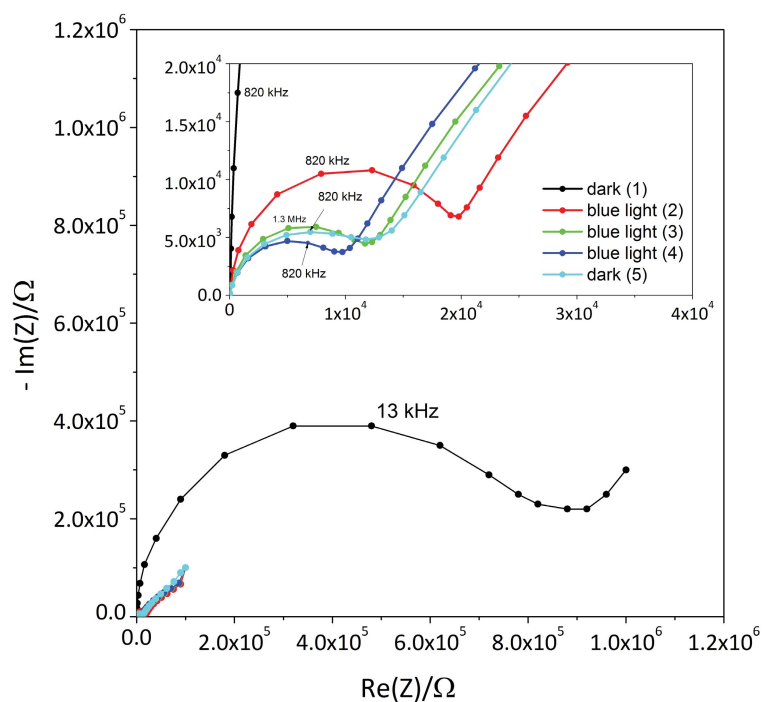


Figure 3.45: Impedance measurements on sample STO_002b (Au current collector) without and with blue light. Big graph: Under illumination the impedance decreases by about two orders of magnitude (see insert). Insert: The numbers indicate the order in which the measurements were performed. After switching off blue light the impedance increases only slowly, whereas it drops sharply upon switching on.

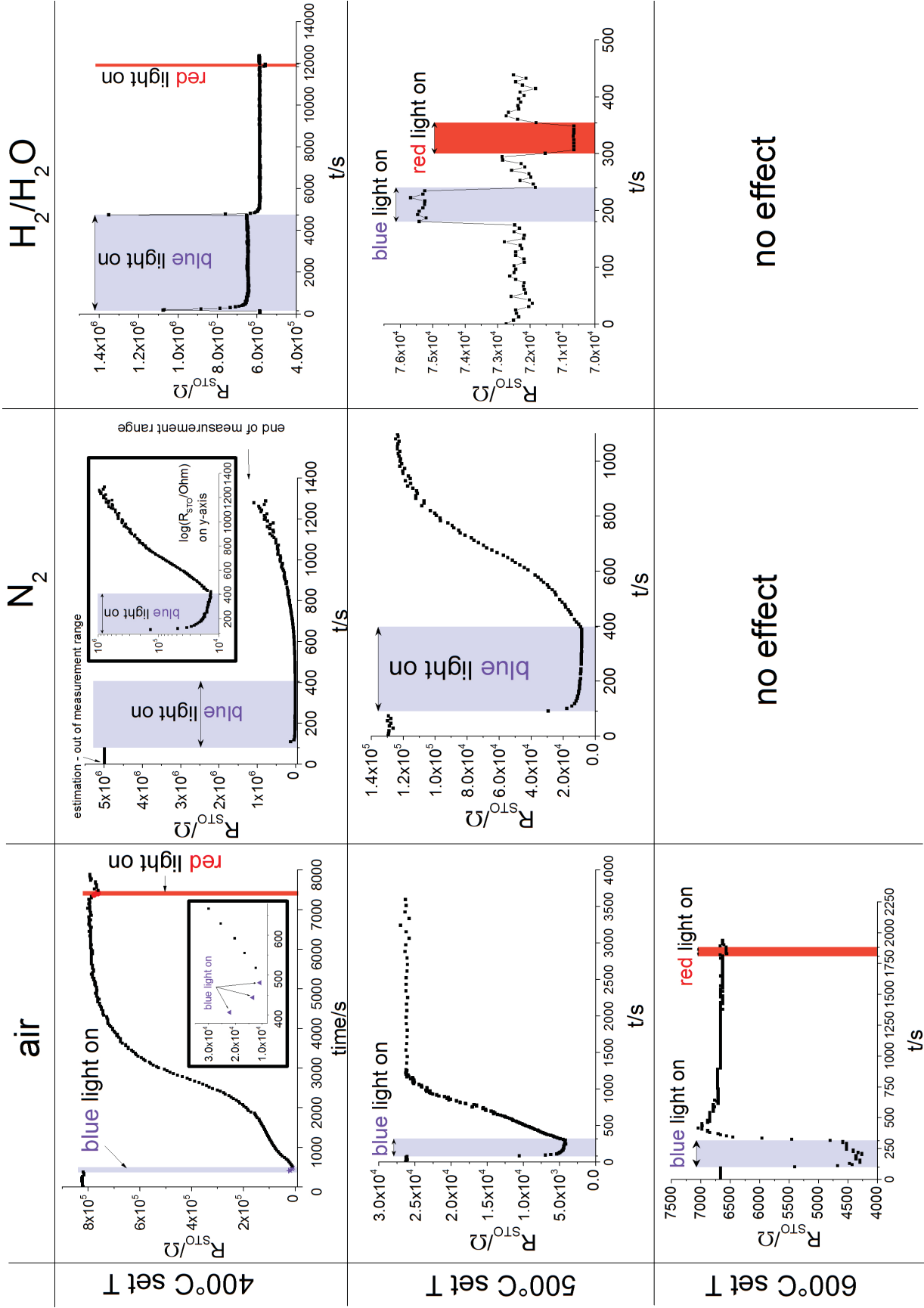


Figure 3.46: $R_{STO}(t)$ curves measured on STO_002b (Au current collector) at different T and $p(O_2)$.

The time evolution of R_{STO} is similar for all measurement in air and in N_2 . When blue light is switched on it drops sharply and quickly reaches a minimum value which is almost constant during illumination. When the light is switched off R_{STO} starts to increase again, but the change is slower than upon switching on. The difference between resistance with and without blue light is about two orders of magnitude at 400°C set T and decreases with temperature. In reducing atmosphere the resistance does not decrease, but instead it increases. This effect, however, is small compared to the changes in air and N_2 . In N_2 and $\text{H}_2/\text{H}_2\text{O}$ at 600°C set T no difference between measurements without, with red or with blue light was observed.

The change in capacitance upon illumination was evaluated by comparing the value without light and the capacitance extracted from the first impedance spectrum measured during illumination. The results are compared in figure 3.47 and show only slight changes which are decided to be insignificant.

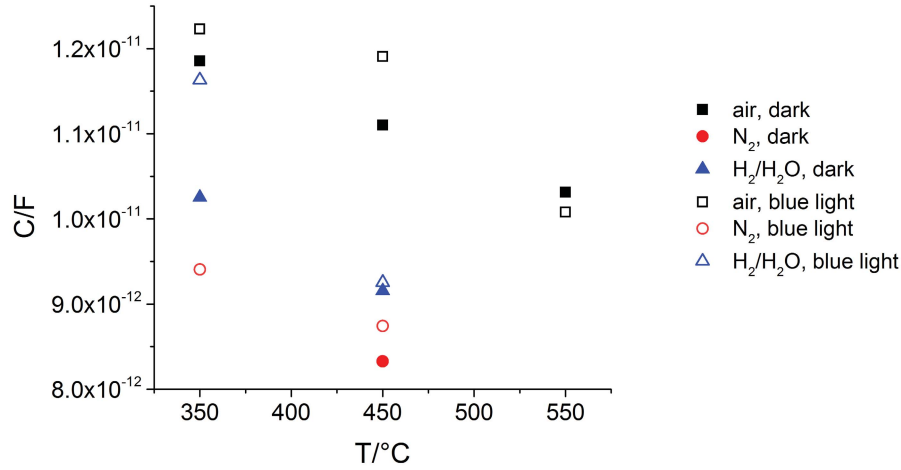


Figure 3.47: Comparison of STO bulk capacitance with and without blue light, measured on sample STO_002b (Au current collector). Almost no change is observed.

3.5 Summarized interpretation

3.5.1 Summary of voltage and impedance measurements

Voltage measurements were divided in (by definition) typical and untypical ones. A typical $U(t)$ curve often had a non-zero voltage offset called U_{dark} . Upon switching on blue light it was characterized by a fast jump to more negative voltage values (U_{PV}), followed by a period where the voltage exhibited increasingly positive values. The voltage U_{PV} is defined as the difference of the peak voltage to U_{dark} . Subsequently, it evolved into a plateau (U_{ss}). Again, U_{ss} is the difference of the steady-state value to U_{dark} . The difference between U_{PV} and U_{ss} is $-(U_{\text{PV}} - U_{\text{ss}})$. When the light was switched off a fast jump to more positive values than U_{dark} resulted. This peak was termed U_{batt} , and is the difference of the highest voltage value to U_{dark} . The distance

to the plateau value is $U_{\text{batt}} - U_{\text{ss}}$. Finally U_{batt} faded away until it reached the initial value, U_{dark} .

On TiO_2 samples the typical effect appeared preferentially on pyramid-type and micro-circle with grid electrodes but this phenomenon was not further elucidated. The equilibration state of the samples was estimated from high temperature data which bears certain risks but is an appropriate means to gain a first hint. According to these estimations the samples measured at 500°C set T are in equilibrium after firing overnight, whereas the ones measured at 400°C are not. However, measurements over longer periods of time suggested that the shape of the light effect was often similar at different equilibration states. An influence of the current collector material on U_{dark} and also the photoeffect was found. Also, the position of the current collector altered the photoreponse. On samples YSZ-TiO₂-Pt_Ana2-550_009 ... 012 in N_2 U_{PV} varied but U_{batt} was approximately constant. It was found that U_{ss} correlated with U_{PV} . The decrease in absolute value of the measured voltage after the sharp peak ($= (U_{\text{PV}} - U_{\text{ss}})$) correlated with U_{batt} but not with U_{PV} . The most straightforward conclusion from experiments on $p(\text{O}_2)$ dependence was that under reducing conditions both U_{dark} and any photoeffects were negligibly small.

Voltage-time curves on STO with Pt current collector were all described as typical, while on STO with Au current collector untypical $U(t)$ curves in $\text{H}_2/\text{H}_2\text{O}$ were observed. The Au current collector apparently lead to higher jumps upon switching on the light but did not change U_{dark} much. Rather, U_{dark} and also U_{batt} were similar on those two samples under most conditions.

On TiO_2 samples impedance measurements with blue light under short circuit conditions lead to a decreased impedance of the feature presumably connected to the electrode reaction. An additional feature appeared in the spectrum, but not when a DC-current-blocking capacitor was used. Also, the impedance decrease was smaller than under short circuit conditions. Electrodes short-circuited during the measurement often changed their appearance from smooth to rough after the measurement. This could be explained by the formation of bubbles during an anodic current flow, but interestingly the rough looks were also noticed on electrodes that were not measured at all.

Impedance spectroscopy on STO samples focussed on time-resolved analysis of the first semi-circle's impedance, which was assigned to the STO bulk. A systematic analysis was carried out on the sample with Au current collector. In air and N_2 the $R_{\text{STO}}(t)$ curve can be described as follows: When blue light was turned on the diameter of the semi-circle decreased quickly and became almost constant. After turning off the light it started to increase very slowly, eventually reaching its original value. In $\text{H}_2/\text{H}_2\text{O}$, however, the effect was not only much smaller but the impedance increased upon irradiation with blue light.

3.5.2 Interpretation

The voltage offset

TiO₂ samples Given the asymmetrically heated setup substantial temperature gradients can arise [153] causing a thermovoltage. This issue was addressed by [144] for a cell with Pt microelectrodes on a YSZ single crystalline electrolyte. It was shown that the measured thermovoltage between a Pt microelectrode and the counter electrode in-

creased with increasing heater temperature, which is the expected behaviour. At 700°C set T it was approximately 30 mV. Considering the lower set temperature in the present study the temperature gradient will also be smaller. Since the largest temperature gradient occurs across the YSZ single crystal and metals usually have smaller Seebeck coefficients than semiconductors, the most relevant Seebeck coefficient is the one connected to YSZ. As this parameter is almost independent of temperature [154] a voltage offset smaller than 30 mV is expected, but values beyond 250 mV were measured in extreme cases. Additionally, U_{dark} decreases with set T . It is therefore concluded that a thermovoltage as described by [144] must be expected but cannot be the only contribution to U_{dark} . Given the dependence of U_{dark} on the current collector metal, its origin could be an effect connected to the interface metal|TiO₂. This assumption is supported by the considerable variation of U_{dark} between samples, which could be due to different space charge layers as a consequence of variations in sample preparation.

SrTiO₃ samples Also for STO samples a similar temperature gradient as for YSZ samples is expected, given the same measurement setup and thickness of the single crystalline substrate. Since more reliable defect data are available for STO and equilibration issues seem to be critical only at 400°C set T the Seebeck coefficient can be estimated from defect chemical data. Only contributions from electrons and holes were taken into account, any ionic effects were neglected. This is possible because the ionic conductivity is low at the partial pressure points considered. The contributions to the Seebeck coefficient by electrons and holes, $S_{e'}$ and $S_{h\cdot}$, respectively, were calculated according to [54, p. 469]:

$$S_{e'} = - \left(\frac{k}{e} \right) \ln \left(\frac{n_0}{[e']} \right) \quad (3.16)$$

$$S_{h\cdot} = + \left(\frac{k}{e} \right) \ln \left(\frac{n_0}{[h\cdot]} \right) \quad (3.17)$$

In this equations n_0 is the number of sites available for defects to be located at, in this case it was taken to be the number of Ti sites per cm⁻³. An additional additive constant considering vibrational entropy [54, p. 469] was omitted because trends in thermovoltage rather than absolute values are used in the comparison. $S_{e'}$ and $S_{h\cdot}$ were combined to give the total Seebeck coefficient, S , following Nowotny *et al.* [155]:

$$S = \frac{\sigma_{e'} S_{e'} + \sigma_{h\cdot} S_{h\cdot}}{\sigma_{\text{ges}}} \quad (3.18)$$

Using the data calculated from the defect model already mentioned [92] the total Seebeck coefficients for three partial pressure points (air, N₂ and H₂/H₂O) were computed. A plot of S as a function of $p(\text{O}_2)$ is shown in figure 3.48. It is clearly seen that the dependence on temperature and partial pressure does not explain the measured thermovoltages. Due to the temperature gradient increasing with set T the Seebeck coefficient would have to decrease considerably in order to give a decreasing, almost zero U_{dark} at 600°C set T . This is not the case. Also a very small value for S should be expected if the very small U_{dark} observed in reducing atmosphere were a thermovoltage only. Instead, the calculated S adopts large negative values in H₂/H₂O. These estimations do not exclude a contribution from thermovoltage in U_{dark} but suggest that it is not the

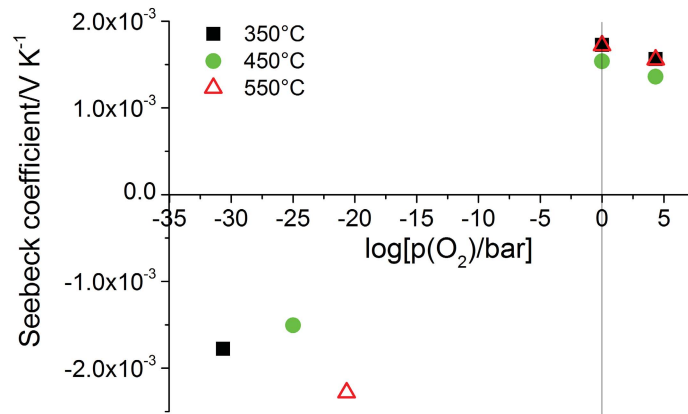


Figure 3.48: The Seebeck coefficient S for STO as a function of oxygen partial pressure (calculation see text).

only one. Despite the dependence of U_{dark} on the current collector metal not being as pronounced as for the TiO_2 samples, possibly the metal|STO interface is involved here as well. Conversely, the dependence of U_{dark} on $p(\text{O}_2)$ is more pronounced on STO.

Two additional phenomena contributing to U_{dark} are conceivable: (a) Very sluggish equilibration of the WE at low temperatures, leading to a mixed potential and (b) a thermoelectric generator driven by a lateral temperature gradient. Concept (b) is explained in [156] and adapted to the situation in the present work in figure 3.49. The cold contact tip not only creates a temperature gradient from the furnace to the contact point but also a lateral gradient. The current collector and the WE materials act as the two components of a thermocouple. The current collector is contacted by the needle, the WE material is contacted *via* YSZ and the CE and so a thermovoltage can be measured. This system would explain the dependence of U_{dark} on the current collector material as well as on the temperature. When T rises, the electric field between current collector and WE becomes smaller since the thermally activated diffusion current against the direction of the field increases. Therefore, this contribution to U_{dark} eventually vanishes because the thermocouple is short-circuited internally.

Voltage and impedance response to light

Voltage response: The first, quick jump (U_{PV}) The results of $U(t)$ measurements showed a dependence of U_{PV} on the current collector material and was in the 10...100 μs range (described in the following, see tables 3.15, 3.16). This fast response and dependence on the metal indicates a connection to the metal|WE interface, which is a Schottky barrier that can act as a solar cell. Let's therefore assume this part of the voltage response is a photovoltage. As the voltage change has to be measured between WE and CE the separation of charge carriers excited by light, which occurs only locally at the Schottky barrier, must change the electrostatic potential at the CE with respect to

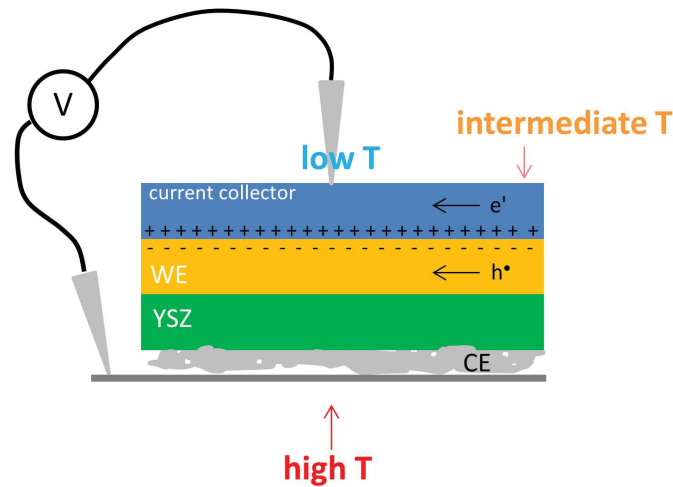


Figure 3.49: A lateral thermoelectric generator as a hypothesis to explain a large part of U_{dark} .

the WE. The spreading of this potential occurs by movement of charged particles, but without electrochemical production of substance, so it can be called a charging current. By pushing a charge into a certain direction (separation in the electric field at the Schottky barrier) all the other charges with the same sign are repulsed and move a little bit. As this current spreads across the cell (WE, electrolyte, CE) it experiences a resistance which influences the time evolution of the PV voltage.

This time evolution will be estimated in the following. First, the cell has to be described by a rough equivalent circuit model (figure 3.50). The junction acting as a PV cell is

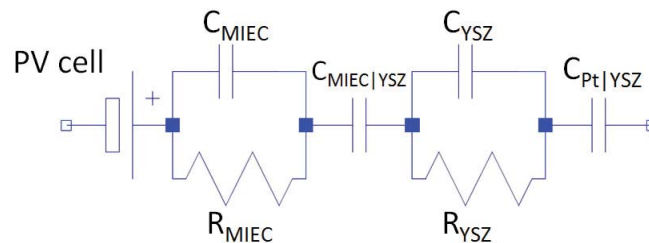


Figure 3.50: Equivalent circuit used to describe the voltage evolution upon switching on blue light.

simply represented by a voltage source. The MIEC and the electrolyte are interpreted as $R||C$ elements. At the interfaces MIEC|YSZ and Pt|YSZ there are double layer capacitances.

For the STO samples this model is simplified by making the following assumptions:

- The dielectric capacitances of STO and YSZ, C_{STO} and C_{YSZ} , are very small, smaller than the interface capacitances. Since they are in parallel to the resistors they are instantly charged (assuming a voltage source with no internal resistance). Then the current only passes through the resistors R_{STO} and R_{YSZ} .

This assumption is plausible because C_{STO} was shown to be in the range of 1×10^{-11} F (figure 3.47), and C_{YSZ} can be calculated to be about 1×10^{-9} F (rela-

tive dielectric constant $\epsilon_r = 27$ [157]), whereas $C_{\text{Pt|YSZ}}$ can be expected to be in the range of 1×10^{-5} F [144]. Also the interface capacitance $C_{\text{STO|YSZ}}$ can be expected to be larger than the dielectric capacitances due to the small thickness of a space charge layer (nm range) compared to the thickness of STO and YSZ (μm range).

- The ohmic resistance in YSZ, R_{YSZ} is negligible because the YSZ layer is very thin. It was estimated to be approximately 200Ω using data from [143].

The resulting simplified circuit model for an STO cell is shown in figure 3.51. It only

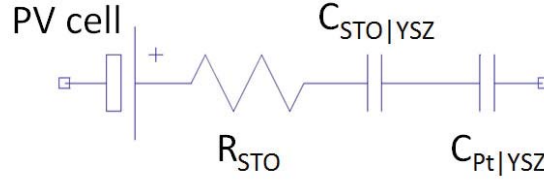


Figure 3.51: Simplified equivalent circuit used to describe the voltage evolution upon switching on blue light in an STO cell.

consists of the STO resistance in series with the two double layer capacitances. The capacitance $C_{\text{STO|YSZ}}$ can be estimated by assuming a depletion of charge carriers at the STO|YSZ interface (Schottky model). The real nature of this interface is unknown but making this assumption we can at least roughly estimate a value for $C_{\text{STO|YSZ}}$ by inserting the depletion layer width W into the formula for a parallel plate capacitor. Furthermore, we assume that the space charge layer in YSZ is negligibly short due to its high concentration of charge carriers and only a one-sided space charge layer has to be considered. Its width was calculated using the formula for W given in [158, p. 89],

$$W = \sqrt{\frac{2\epsilon U_{\text{bi}}}{zeN_{\text{B}}}}, \quad (3.19)$$

where ϵ , U_{bi} , z , e and N_{B} represent the dielectric constant of STO ($= \epsilon_0 \cdot \epsilon_r(\text{STO})$), the built-in potential, the charge number of the dopant, the elementary charge and the dopant concentration, respectively. Typical space charge potentials U_{bi} are between 500 mV (for grain boundaries in STO [88], for example, but also for a Ge pn-junction [158, p. 87]) and 1,2 V (for a GaAs pn-junction [158, p. 87]). Insertion of $U_{\text{bi}} = 500$ mV and the dopant concentration of $5 \times 10^{17} \text{ cm}^{-3}$ (with $z = 1$) already assumed in subsection 3.4.2 yields a depletion layer width of approximately 200 nm and it follows for sample STO_002b that $C_{\text{STO|YSZ}} \approx 5 \times 10^{-8}$ F. Since in this model only the dopant content is considered and not the concentrations of the free charge carriers $C_{\text{STO|YSZ}}$ is independent of oxygen partial pressure. To compare the theoretical time behaviour with the experiments we can calculate a theoretical time constant $\tau_{\text{th}} = R_{\text{STO}} \cdot C_{\text{tot}}$ using the STO resistance measured by EIS or calculated from the defect model [92] (dark, in N_2 ; too high to measure). The τ_{th} values were compared with the measured time behaviour. Both the time development after switching on blue light and switching it off was evaluated. Even though the time evolution was not exponential a time constant τ_{meas} was estimated by searching the data point which was nearest to the point where the voltage had decreased to a fraction of $1/n_{\text{Euler}}$ of the total voltage jump (with n_{Euler}

Table 3.15: Sample STO_002b (Au current collector): Comparison of calculated time constants for the voltage evolution as a function of time during switching on and off blue light and those estimated from measurements. Set T was 400°C.

	air		N ₂	
	switching on	switching off	switching on	switching off
W/nm		192		
$C_{\text{STO} \text{YSZ}}/\text{F}$		4.72×10^{-8}		
$C_{\text{Pt} \text{YSZ}}/\text{F}$		1.54×10^{-6}		
C_{tot}/F		4.57×10^{-8}		
R_{STO}/Ω	8×10^5	9.57×10^3	1.28×10^6	1.38×10^4
$\tau_{\text{th}}/\text{s}$	0.037	4.4×10^{-4}	0.059	6.3×10^{-4}
$\tau_{\text{meas}}/\text{s}$	0.062	0.078	0.062	0.234

being Euler's number) and evaluating the time elapsed since switching on or off blue light. This was done for measurements on sample STO_002b (Au current collector grid) in air as well as N₂ at 400°C set T . For sample STO_001 (Pt current collector grid) and other conditions the voltage evolution as a function of time was too fast to be resolved. The results are summarized in table 3.15. The theoretical and measured values for τ are in good agreement when switching on the light, not when switching it off. In particular, the time constants are similar for air and N₂ which is reflected in the model by W being independent of $p(\text{O}_2)$. The different theoretical time constants when switching off blue light indicate a more complex situation than assumed by this simple model.

In the case of samples with a titania WE the circuit model in figure 3.52 results after simplification of the general model (figure 3.50) by analogous arguments as above, but in this case neither of the two resistances R_{TiO_2} or R_{YSZ} can be neglected. The resistance

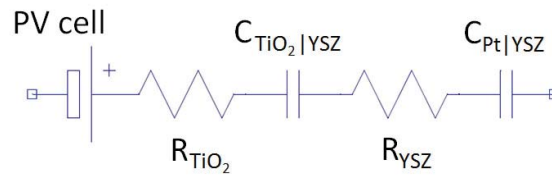


Figure 3.52: Equivalent circuit used to describe the voltage evolution upon switching on blue light in a TiO₂ cell.

was calculated using the spreading resistance formula (equation 3.4, page 77) and data measured in [143] rather than taking the measured R_{spr} values. This was done because the samples used for this comparison had a current collector grid on the weakly conductive titania layer and so the active surface area is unknown (see subsection 3.4.1, p. 77 ff.). The vertical resistance in the titania layer was estimated from the defect chemical data already mentioned [78, 85]. The capacitance value for $C_{\text{Pt}|\text{YSZ}}$ was calculated using the same literature data as above [144]. For the capacitance $C_{\text{TiO}_2|\text{YSZ}}$ the same capacitance per unit area as for $C_{\text{Pt}|\text{YSZ}}$ was assumed as a first approximation.

Table 3.16: Comparison of calculated time constants for the voltage evolution as a function of time during switching on and off blue light and those estimated from measurements. 500°C set T , air.

	Pt 010				Pt 011			
	on 1	on 2	off 1	off 2	on 1	on 2	off 1	off 2
$C_{\text{TiO}_2 \text{YSZ}}/\text{F}$				3.53×10^{-8}				
$C_{\text{Pt} \text{YSZ}}/\text{F}$				2.5×10^{-5}				
C_{tot}/F				3.53×10^{-8}				
R_{TiO_2}/Ω				7×10^4				
R_{spr}/Ω				6.96×10^4				
$\tau_{\text{th}}/\text{s}$				5×10^{-3}				
$\tau_{\text{meas}}/\text{s}$	0.34	0.30	0.24	0.25	0.23	0.25	0.25	0.25

The resulting τ_{th} were compared to the experimental behaviour, which was, in the same way as above, quantified with a time constant τ_{meas} in spite of the fact that the $U(t)$ curve was not an exponential function. Measurements were carried out on microelectrodes with $\varnothing = 300 \mu\text{m}$ and a Pt current collector grid. An overview of the results is given in table 3.16. The calculated time constant is about two orders of magnitude smaller than the measured one. This is a clear disagreement, not least because the estimation favours a large time constant with $C_{\text{TiO}_2|\text{YSZ}}$ being calculated from the same capacitance per area as $C_{\text{Pt}|\text{YSZ}}$. In reality, $C_{\text{TiO}_2|\text{YSZ}}$ is smaller because the space charge layer is larger at the $\text{TiO}_2|\text{YSZ}$ than at the $\text{Pt}|\text{YSZ}$ interface, which is due to the small number of charge carriers in TiO_2 . This comparison shows that the electrochemical processes are even more complex than in STO and can not be described by the proposed model.

Voltage response: Battery voltage and steady state Following the relatively fast jump, the voltage decreases in absolute value and becomes more or less constant. Since it was found in literature that light may only affect the oxygen incorporation kinetics of MIECs (see subsection 1.1.6) an oxygen incorporation driven by light from a rather equilibrated state is conceivable. Only one reaction direction of the dynamic equilibrium would be changed and so net incorporation could be reached under light. Assuming this, the voltage response in this part of the typical curve could stem from an altered defect state in the MIEC, formally a different oxygen partial pressure in the material. This has two consequences: First, the PV voltage is altered. The changed defect concentrations influence the space charge at the Schottky barrier and as a consequence also U_{PV} changes. Second, the new defect state in STO also causes a Nernst voltage across the electrochemical cell. The altering of the PV voltage happens faster because the Schottky interface is at the surface of the STO crystal, so the incorporated oxygen only has to diffuse a short way to create an effect. In contrast to this, the Nernst voltage has to be transmitted *via* the $\text{STO}|\text{YSZ}$ interface. The oxygen takes longer to diffuse there and so the response of U_{batt} is slower.

Both these effects can be imagined to occur simultaneously. U_{PV} , U_{batt} and the resulting sum voltage are depicted in the schematic $U(t)$ curve in figure 3.53. The PV contri-

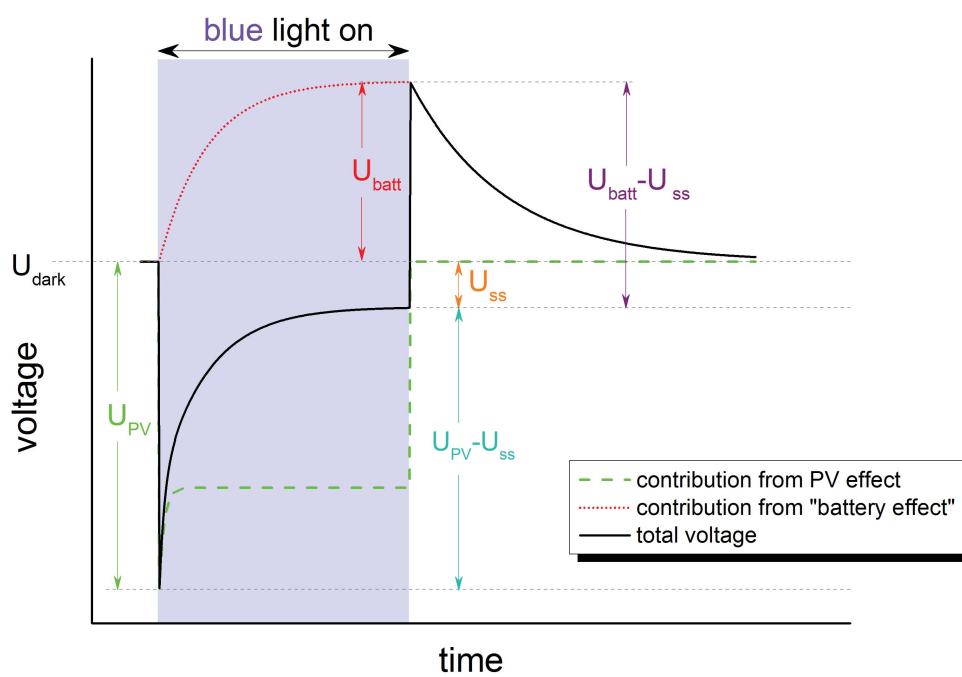


Figure 3.53: Scheme of a typical $U(t)$ curve, showing the contributions of a photovoltaic and stoichiometric light effect ("battery effect").

bution is represented by a green, hatched line: After the fast change upon switching on blue light its absolute value decreases as a consequence of altered defect concentrations in the MIEC. The red, dotted line represents the "Nernst" contribution to the total voltage, which is also a result of oxygen exchange with the atmosphere during illumination. The black, full line is the sum of the above contributions. Eventually, a constant value, U_{ss} , is reached.

Upon switching off the light the PV voltage is gone almost instantly (see analysis above). The stoichiometry change brought about by light is also reversed by excorporation of oxygen. Since the decrease of the photovoltaic contribution can still be assumed to be very fast compared to the chemical changes the highest peak that follows switching off blue light is termed U_{batt} .

By varying the different contributions of photovoltaics and the degree of oxygen incorporation with blue light even the $U(t)$ curves so far classified as "untypical" could be explained.

Voltage response: Comparison with measurement on STO without YSZ Voltage-time measurements were also carried out on an STO single crystal (without electrolyte) by [122]. The measurement geometry and results are sketched in figure 3.54. When blue light is turned on the voltage jumps to a negative value very quickly, then increases again and evolves into a plateau. This part of the $U(t)$ curve is similar to the ones measured in this work but are interpreted in a slightly different way. The first jump is also assigned to a PV voltage, produced at the Schottky contact between Pt grid and STO. Furthermore, oxygen incorporation into STO during illumination with blue light is assumed as well, which alters the PV voltage. However, since there is no electrolyte, no Nernst voltage can build up. The MIEC can be imagined to be short-circuited internally by electronic conduction. So, upon switching off the light, no battery voltage remains and the voltage returns to its initial value, even though the crystal still has different stoichiometry. Comparing the $U(t)$ curve in figure 3.54 with the measurement on

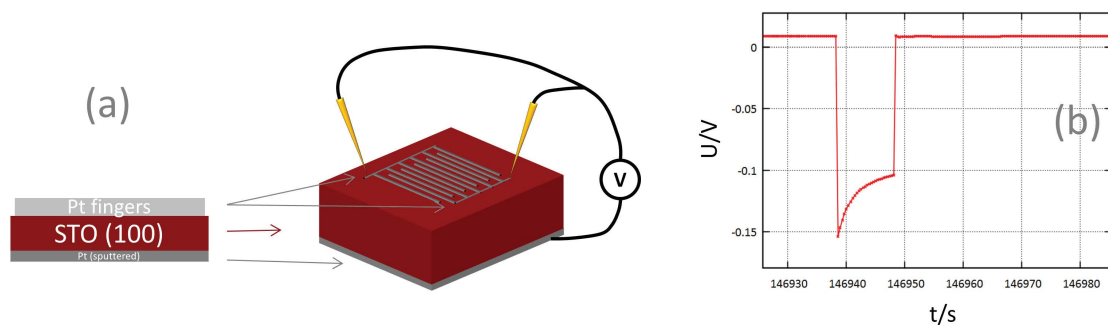


Figure 3.54: $U(t)$ measurement on STO single crystal (without YSZ) by [122]. (a): Sketch of sample and measurement setup. The sample is an STO single crystal with Pt electrodes only, no electrolyte was used. (b): Typical $U(t)$ curve measured on this type of sample.

STO.001 under the same conditions (400°C set T , air; see figure 3.21, page 70) reveals a more pronounced jump when blue light is switched on (U_{PV}) on the sample measured by [122] (≈ -160 mV as opposed to -109 mV on STO.001). Another, difference is dis-

covered when U_{ss} are compared. While on STO_001 $U_{ss} \approx U_{batt} \approx 306$ mV, meaning that during illumination the photovoltaic contribution was practically erased, on the sample from [122] the PV voltage remaining in the steady state was -110 mV vs. U_{dark} . In the latter case, since the PV part is the only voltage present, it has not vanished at all. One difference in the experimental conditions that could account for these quantitative disagreements could be the light intensity. In [122] a wave guide was used to increase the light intensity, whereas in the present study no waveguide was used. In order to fully elucidate the differences in these two systems more measurements under identical conditions would be needed.

EIS measurements on titania samples: Kinetic light effect In EIS measurements on TiO_2 it was shown that the electrode resistance decreases during illumination with blue light. This is a second kind of light effect since it concerns both directions of the oxygen surface exchange, not only one, as discussed above. In $U(t)$ measurements this acceleration of kinetics with blue light should also be visible: The evolution into the plateau is assumed to be faster than the time behaviour when the light is switched off. This effect was observed in some measurements (see e.g. figure 3.14 (a), page 57) but data are not sufficient to allow a reliable analysis.

EIS measurements on STO sample: Overview of $R_{STO}(t)$ curves Impedance measurements on STO have to be interpreted differently since the analysed feature does not describe the oxygen exchange reaction but the STO bulk (conductivity and capacitance). The rather fast jump in R_{STO} when switching on blue light could be associated with photoconductivity (see figure 3.46, page 96). For a conductivity change to be measurable it has to occur throughout large parts of the bulk, so the mean free path of electronic charge carriers must be assumed long.

Following the change due to photoconductivity the conductivity changes slightly owing to oxygen incorporation. When blue light is turned off the resistance value only returns to its initial value very slowly. This can be explained by oxygen incorporated during illumination being exorporated sluggishly. The altered defect equilibrium leads to higher conductivity as can be seen from a Brouwer diagram of a MIEC in the p-conducting regime. Incorporation of oxygen needs electrons to form oxide ions, thereby creating electron holes and enhancing hole conductivity. In the Brouwer diagram the illuminated compound could be described by a shift towards higher $p(O_2)$.

Another effect may influence the STO conductivity during illumination: While under open-circuit conditions the built-in PV cell could not polarize the mixed conducting STO, during the EIS measurement, when current is allowed to flow (through the impedance analyzer), stoichiometry polarization in STO will be the consequence, just as if an external voltage source was used. This charging of the chemical capacitance by the photovoltage should also have an influence on the conductivity and its time evolution.

EIS measurements on STO sample: diffusion of oxygen under illumination The incorporation of oxygen into the oxide and also its distribution into the bulk of the single crystal must take place during the time when blue light is switched on, which was for example 100 s in the experiment at $400^\circ C$ in air (figure 3.46, page 96, top left). During this time enough oxygen has to be incorporated to effect a stoichiometry change

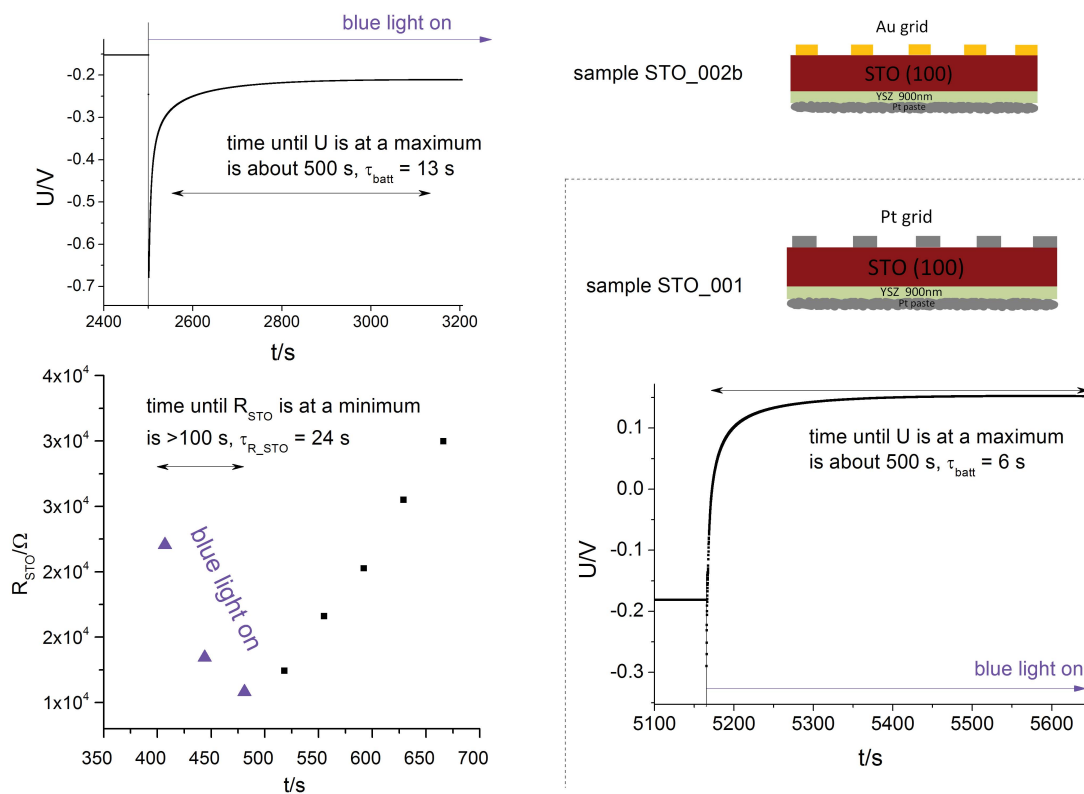


Figure 3.55: Comparison of behaviour of U and R_{STO} as a function of time (400°C set T in air). The time from switching on blue light until the battery voltage is built up significantly is evaluated. This time is compared to an analogous time for R_{STO} . Data under several T and $p(\text{O}_2)$ combinations are given in table 3.17.

which is visible as a Nernst voltage and also as a change in R_{STO} which is not caused by photoconductivity but by the stoichiometry change and therefore re-increases only sluggishly after turning off blue light. Therefore, the time scales for the build-up of U_{batt} in a $U(t)$ curve and the decrease of R_{STO} in the time-resolved EIS measurement must be the same. The results of this check are summarized in table 3.17.

The time to build up U_{batt} was read from a $U(t)$ curve in two different ways. First, the time from switching on blue light until the voltage became constant or started to change direction was evaluated (t_{batt}). Second, a time constant, τ_{batt} was estimated (procedure as described before in this chapter). Both ways are just rough estimations. Figure 3.55 illustrates this for measurements at 400°C set T in air. Both t_{batt} and τ_{batt} are given in the top part of table 3.17. Also for the time behaviour of R_{STO} two characteristic values were estimated: The time needed for R_{STO} to become almost constant in a series of EIS measurements, which is denoted by $t_{R_{\text{STO}}}$, and the corresponding time constant, $\tau_{R_{\text{STO}}}$. They are given in the bottom part of the table. Both values are very rough estimations because of various experimental limitations: The time resolution is only approx. 10 s (minimum time between two impedance spectra), a steady state for R_{STO} was not always reached and R_{STO} (dark) could not always be measured (out of range). The values for t_{batt} correspond very well to $t_{R_{\text{STO}}}$. The values for τ_{batt} differ from each other at the most by a factor of five. Among the $\tau_{R_{\text{STO}}}$ values the one at 500°C in air is small com-

Table 3.17: Comparison of time needed to build up U_{batt} (t_{batt} , τ_{batt}) and to decrease R_{STO} significantly ($t_{R_{\text{STO}}}$, $\tau_{R_{\text{STO}}}$). They are comparable which supports the theory of the two phenomena having the same cause.

voltage measurements					
sample	current collector material	$T_{\text{set}}/^{\circ}\text{C}$	$p(\text{O}_2)$	t_{batt}/s	$\tau_{\text{batt}}/\text{s}$
STO_001	Pt	400	air	500	6
STO_001	Pt	500	air	500	20
STO_001	Pt	400	N_2	500	10
STO_001	Pt	500	N_2	600	4
STO_002b	Au	400	air	600	13
STO_002b	Au	500	air	50	4
STO_002b	Au	400	N_2	400	18
STO_002b	Au	500	N_2	500	16

EIS measurements					
sample	current collector material	$T_{\text{set}}/^{\circ}\text{C}$	$p(\text{O}_2)$	$t_{R_{\text{STO}}}/\text{s}$	$\tau_{R_{\text{STO}}}/\text{s}$
STO_002b	Au	400	air	100	24
STO_002b	Au	500	air	54	8
STO_002b	Au	400	N_2	200	70
STO_002b	Au	500	N_2	150	13

pared to the others. Nevertheless, τ_{batt} and $\tau_{R_{\text{STO}}}$ are comparable. Furthermore, when comparing them at the same conditions (T , $p(\text{O}_2)$, sample), they are in very good agreement which further supports the assumed model.

The time needed for oxygen to diffuse into the STO bulk can also be estimated from literature data. Since there is no data for undoped STO single crystals available and assuming that the nominally undoped crystals used are p-doped by impurities, defect data for weakly Fe-doped STO [92] was used, as several times before in this study. For this system a chemical diffusion coefficient for oxygen was published [93]. It was pointed out that trapping of holes at the Fe^{3+} ions leads to a diffusion coefficient which is several orders of magnitude smaller than without trapping (see figure 3.56). Reading the values from this diagram at 350°C we find values of about $10^{-7.3} \approx 5 \times 10^{-8} \text{ cm}^2\text{s}^{-1}$ and $1 \times 10^{-4} \text{ cm}^2\text{s}^{-1}$ with and without trapping, respectively. To estimate the time needed to fill the STO bulk with a new concentration of oxygen the rule of thumb for the diffusion length L , $L = \sqrt{Dt}$, with D and t being the chemical diffusion coefficient and the time, respectively, is rearranged into $t = \frac{L^2}{D}$ and yields about $5 \times 10^4 \text{ s}$ with trapping and approximately 25 s without trapping. This time constant agrees rather well with τ_{batt} and $\tau_{R_{\text{STO}}}$ (table 3.17). After five to ten times this time constant most of the stoichiometry change should have taken place and hence this value is in good agreement with t_{batt} and $t_{R_{\text{STO}}}$. The irrelevance of trapping could be explained by the large number of electrons and holes created by illumination with blue light. Considering that oxygen vacancies and electrons must both move to cause ambipolar diffusion of oxygen the increased number of electrons can be responsible for the acceleration of oxygen distribution in the STO bulk. This hypothesis fits very well into the overall picture of that light causes fast incorporation of oxygen into STO.

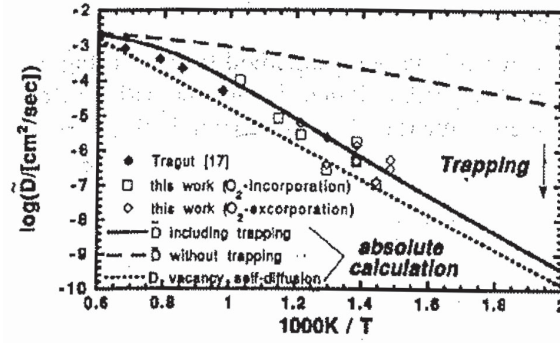


Figure 3.56: Figure 8 from [93] showing an Arrhenius plot of the chemical diffusion coefficient of oxygen in weakly Fe-doped STO. The measured data can only be explained when trapping of holes at the Fe^{3+} atoms is taken into account. Without trapping the diffusion coefficient is expected to be several orders of magnitude larger.

It must be noted, however, that nominally undoped STO single crystals were used, so the actual dopant elements are unknown and trapping could be absent altogether. Then, the oxygen diffusion would be fast anyway.

EIS measurements on STO sample: R_{STO} after switching off blue light The hypothesis of oxygen being incorporated quickly during illumination and excorporated slowly afterwards implies that the chemical capacitance of STO is charged and discharged in this cycle. Therefore, it should be possible to link the time needed to excorporate oxygen to the chemical capacitance calculated from defect data. So, a time constant for the R_{STO} curve after switching off blue light was estimated for measurements of STO.002b at approximately 350°C , 450°C and 550°C (corresponding to 400°C , 500°C and 600°C set T , respectively) in air and for 450°C in N_2 . These measurements were plotted in subsubsection 3.4.2 in figure 3.46, page 96. Since the curve did not show exponential behaviour the time constant $\tau_{R_{\text{STO}}, \text{light off, meas}}$ was estimated as described above for τ_{meas} .

When we assume that during the impedance measurement (HP 4192 A impedance analyzer) the sample is short-circuited the oxygen will be released *via* the counter electrode, while a current flows in the outer circuit. This path has much lower resistance than excorporation at the surface, which is hindered by the slow exchange reaction. Then, the relevant resistance is the oxygen vacancy resistance in STO, $R_{\text{STO}, V_{\text{O}}^{\cdot}}$. During illumination $R_{\text{STO}, V_{\text{O}}^{\cdot}}$ decreases (compared to darkness) because as oxygen is incorporated oxygen vacancies vanish. After illumination $R_{\text{STO}, V_{\text{O}}^{\cdot}}$ starts to increase again. The time evolution can therefore be expected to be complex because $R_{\text{STO}, V_{\text{O}}^{\cdot}}$ changes constantly. Furthermore, $R_{\text{STO}, V_{\text{O}}^{\cdot}}$ is unknown under illumination. The theoretical time constant was therefore calculated using $R_{\text{STO}, V_{\text{O}}^{\cdot}}$ in equilibrium (darkness), which can be computed from literature data. So, the formula used for the theoretical time constant $\tau_{R_{\text{STO}}, \text{light off, th}}$ is:

$$\tau_{R_{\text{STO}}, \text{light off, th}} = R_{\text{STO}, V_{\text{O}}^{\cdot}} \cdot C_{\text{chem}}. \quad (3.20)$$

Since $R_{\text{STO}, V_{\text{O}}^{\cdot}}$ is underestimated by this procedure the real value for $\tau_{R_{\text{STO}}, \text{light off, th}}$ is expected to be higher. The chemical capacitance C_{chem} and $R_{\text{STO}, V_{\text{O}}^{\cdot}}$ were once again calculated from defect concentrations for weakly Fe-doped STO [92] ($[\text{Fe}] = 5 \times 10^{17} \text{ cm}^{-3}$). The formula for C_{chem} was taken from [152], trapping of holes was taken into account

Table 3.18: Measured and calculated time constants for the increase of R_{STO} after switching off blue light. Temperatures are values estimated from the set T , which is $\approx 50^\circ\text{C}$ higher.

conditions	$\tau_{R_{\text{STO}}, \text{light off, th}} / \text{s}$	$\tau_{R_{\text{STO}}, \text{light off, meas}} / \text{s}$
350°C, air	57	2738
450°C, air	40	612
550°C, air	31	45
450°C, N_2	2	342

by inserting the trapping factor $\chi_{\text{h}\cdot}$ [53, p. 327]:

$$C_{\text{chem}} = \frac{e^2}{kT} V \left(\frac{\chi_{\text{h}\cdot}}{z_{\text{h}\cdot}^2 [\text{h}\cdot]} + \frac{1}{z_{\text{V}\cdot\text{O}}^2 [\text{V}\cdot\text{O}]} \right)^{-1} \quad (3.21)$$

where z is the charge number of the respective species (=1 for holes and 2 for oxygen vacancies) and V represents the volume of the sample. The trapping factor is given by

$$\chi_{\text{h}\cdot} = \frac{(1 + K_{\text{trap}} [\text{h}\cdot])^2}{(1 + K_{\text{trap}} [\text{h}\cdot])^2 + [D] K_{\text{trap}}} \quad (3.22)$$

where $[D]$ denotes the total dopant content and K_{trap} is the mass action constant for the trapping equilibrium



Table 3.18 shows the results for the measured and calculated time constants. The difference in calculation and experiment is mostly about one to two orders of magnitude. Considering that the theoretical time constant was underestimated by taking the value for $R_{\text{STO}, \text{V}\cdot\text{O}}$ in darkness the disagreement can at least partially be explained. It is however possible that additional processes, which are not considered in this estimation, are important.

EIS measurements on STO sample: $R_{\text{STO}}(t)$ under reducing conditions Under reducing conditions R_{STO} in the steady state was observed to increase during illumination with blue light. The charging of C_{chem} by U_{PV} is consistent with this phenomenon. Also under reducing conditions the PV voltage was negative. A measured negative voltage means that electrons accumulate in the current collector and holes go to the MIEC electrode. Under reducing conditions the majority charge carriers are electrons and enriching the STO bulk with holes by oxygen incorporation leads to an increase in resistance due to recombination between electrons and holes. Under oxidising atmosphere the same direction of charge separation leads to a decrease in resistance because the majority charge carriers are holes.

4 Conclusions

Single crystalline strontium titanate and TiO_2 thin films were investigated as electrodes in high-temperature solid state photoelectrochemical cells. Effects were most pronounced and reproducible in air and N_2 atmosphere at temperatures between approximately 350°C and 450°C , so measurements focussed on these conditions.

Voltage-time curves were recorded while blue and red light was switched on and off. Blue light caused a voltage change of up to several hundred mV, depending on material and geometry, while red light only lead to small effects (several mV) which were attributed to heating by the incident irradiation. The shapes of $U(t)$ curves were diverse but could be separated into typical and untypical ones. The characteristics of typical behaviour were the same for both SrTiO_3 and TiO_2 electrodes.

Impedance measurements showed an effect of blue light on the electrode kinetics of titania electrodes. On SrTiO_3 electrodes the bulk resistance of STO decreased by up to two orders of magnitude during illumination with blue light and took several 1000 s (350°C , air) to regain its initial value.

The phenomena were analysed in the light of light-induced defect chemical changes in the electrode materials. It was found that at least two separate phenomena occur upon irradiation with blue light: A photovoltaic and a defect chemical effect. The time evolution of the PV voltage when blue light was switched on (10...100 μs) could partly be explained by the spreading of the electrostatic potential through the cell considering the capacitances and resistances involved.

Defect chemical change was suggested to occur by incorporation of oxygen driven by blue light. The light-induced stoichiometry change had at least three consequences. First, it influenced the PV voltage by altering the space charge potential at the junction responsible. Second, it created a Nernst voltage (battery voltage) across the electrochemical cell. Third, it enhanced hole conductivity (in STO). When PV and battery voltages were added typical $U(t)$ curves could be modelled qualitatively.

From the combination of $U(t)$ curves and time-resolved measurements of the SrTiO_3 bulk conductivity by EIS it was concluded that the incorporation and distribution of oxygen in the bulk of the material is rather fast when blue light is turned on. This is also in agreement with the very few literature data on this topic. For instance, it took only several 100 s to reach the plateau of a conductivity or voltage change when light was switched on. In contrast to this, excorporation was slow. It typically occurred on a timescale of several 1000 s. This model was also supported by the kinetic light effect observed on titania electrodes.

Hence, in the present study novel effects of light on defect-related properties such as conductivity and Nernst voltage of a solid state photoelectrochemical cell could be identified and characterized.

Acknowledgements

I would like to thank Prof. Fleig for the possibility to realize this thesis in his group, his support throughout the years and the many discussions. After realizing that a "quick word" could require eating and drinking beforehand my brain performed a lot better.

Furthermore, I would like to thank all colleagues for discussions, helpful advice and their support in general: Alex H., Alex S., Ghislain Michel, Peter, Plüsch, Edvinas, Markus, Maximilian, Julia, Andi, Sandra, Plausch, Stefanie, Tobi, Matthias, Michael, Lukas, Andrés, David, Gerhard and Gerald H..

Also, I would like to thank "The Force", Udo, Kurt, Eva, Joanna and Daniela, for help with administrative, IT and gas issues and for spreading relaxedness through the whole group.

For helpful advice and discussions on light issues I would especially like to thank the members of the circle of light: Alex O., Prof. Ponweiser, Prof. Summhammer, Prof. Fleig (once again), Georg, Bernhard, Hamed and Gerald G..

I especially appreciate Bernhard's advice on shielding topics and his ability to fix programming and device communication issues very quickly ("difficult - a few seconds; impossible - a few minutes" [quote to be found by the reader]), as well as his constant strive for better lamps and automated measurements, which greatly helped me. I would also like to thank Georg and Hamed for their support in mechanical engineering issues.

Furthermore, I would like to thank Werner Artner and Elisabeth Eitenberger for recording XRDs and SEM micrographs, respectively. In particular, I am grateful for Werner's enthusiasm to record yet one more diffractogram with barely any reflections and his help with data evaluation.

I would also like to thank Philipp Hans for helpful discussions on X-ray diffractometry.

Finally, I would like to thank my family and friends for their constant support.

Bibliography

- [1] BR-Alpha Alpha Centauri episode 84 - "Sind die Naturgesetze zufällig?", <https://www.youtube.com/watch?v=80oEoPqY8jI> (accessed 28/08/2015).
- [2] Studienplan für das Doktoratsstudium der Naturwissenschaften/Sozial- und Wirtschaftswissenschaften/Technischen Wissenschaften an der TU Wien., http://www.tuwien.ac.at/fileadmin/t/studabt/downloads/Studienplaene/Aktuelle_Curricula_2013/Studienplan_Doktoratsstudium_Fassung_01-10-2013.pdf (accessed 07/09/2015).
- [3] Chalmers, A., *What is this thing called science?*, 4th edition; Open University Press: 2013.
- [4] Ostwald, W., *Elektrochemie - Ihre Geschichte und Lehre*; Verlag von Veit und Comp.: Leipzig, 1896.
- [5] <http://www.merriam-webster.com/dictionary/culture> (accessed 14/09/2015).
- [6] <http://www.duden.de/rechtschreibung/Kultur> (accessed 14/09/2015).
- [7] Herrmann, A. In *Neue Deutsche Biographie 8, Onlinefassung*, 1969, pp 713–714, <http://www.deutsche-biographie.de/pnd11855008X.html> (accessed 14/10/2015).
- [8] Hecht, J. Short history of laser development. *Optical Engineering* **2010**, *49*, 091002–091002/23.
- [9] Bockris, J. O. In *Comprehensive Treatise of Electrochemistry*, Bockris, J. O., Conway, B. E., Yeager, E., White, R. E., Eds.; Plenum Press: New York, London, 1981; Chapter 1.
- [10] McKone, J. R.; Lewis, N. S.; Gray, H. B. Will Solar-Driven Water-Splitting Devices See the Light of Day? *Chemistry of Materials* **2014**, *26*, 407–414.
- [11] Babu, K. S. C.; Srivastava, O. N.; Rao, G. V. S. Photoelectrochemical solar cells: Present status. *Current science* **1994**, *66*, 715–729.
- [12] Teets, T. S.; Nocera, D. G. Photocatalytic hydrogen production. *Chemical Communications* **2011**, *47*, 9268–9274.
- [13] Walter, M. G.; Warren, E. L.; McKone, J. R.; Boettcher, S. W.; Mi, Q.; Santori, E. A.; Lewis, N. S. Solar Water Splitting Cells. *Chemical Reviews* **2010**, *110*, 6446–6473.
- [14] Gratzel, M. Photoelectrochemical cells. *Nature* **2001**, *414*, 338–344.
- [15] Fujishima, A.; Honda, K. Electrochemical Photolysis of Water at a Semiconductor Electrode. *Nature* **1972**, *238*, 37–38.
- [16] Sheppard, L. R.; Nowotny, J. Materials for photoelectrochemical energy conversion. *Advances in Applied Ceramics* **2007**, *106*, 9–20.

- [17] Kung, H. H.; Jarrett, H. S.; Sleight, A. W.; Ferretti, A. Semiconducting oxide anodes in photoassisted electrolysis of water. *Journal of Applied Physics* **1977**, *48*, 2463–2469.
- [18] Nobe, K.; Bauerle, G. L.; Braun, M. Photoelectrolysis. *Journal of Applied Electrochemistry* **1977**, *7*, 379–382.
- [19] Dholam, R.; Patel, N.; Adami, M.; Miotello, A. Physically and chemically synthesized TiO₂ composite thin films for hydrogen production by photocatalytic water splitting. *International Journal of Hydrogen Energy* **2008**, *33*, 6896–6903.
- [20] Watanabe, T.; Fujishima, A.; Honda, K.-i. Photoelectrochemical Reactions at SrTiO₃ Single Crystal Electrode. *Bulletin of the Chemical Society of Japan* **1976**, *49*, 355–358.
- [21] Bora, D. K.; Braun, A.; Constable, E. C. "In rust we trust". Hematite - the prospective inorganic backbone for artificial photosynthesis. *Energy & Environmental Science* **2013**, *6*, 407–425.
- [22] Braun, A.; Sivula, K.; Bora, D. K.; Zhu, J.; Zhang, L.; Gratzel, M.; Guo, J.; Constable, E. C. Direct Observation of Two Electron Holes in a Hematite Photoanode during Photoelectrochemical Water Splitting. *The Journal of Physical Chemistry C* **2012**, *116*, 16870–16875.
- [23] Sivula, K.; Le Formal, F.; Gratzel, M. Solar Water Splitting Progress Using Hematite (α -Fe₂O₃) Photoelectrodes. *ChemSusChem* **2011**, *4*, 432–449.
- [24] Allam, N. K.; Alamgir, F.; El-Sayed, M. A. Enhanced Photoassisted Water Electrolysis Using Vertically Oriented Anodically Fabricated Ti-Nb-Zr-O Mixed Oxide Nanotube Arrays. *ACS Nano* **2010**, *4*, 5819–5826.
- [25] Reece, S. Y.; Hamel, J. A.; Sung, K.; Jarvi, T. D.; Esswein, A. J.; Pijpers, J. J. H.; Nocera, D. G. Wireless Solar Water Splitting Using Silicon-Based Semiconductors and Earth-Abundant Catalysts. *Science* **2011**, *334*, 645–648.
- [26] Young, E. R.; Costi, R.; Paydavosi, S.; Nocera, D. G.; Bulovic, V. Photo-assisted water oxidation with cobalt-based catalyst formed from thin-film cobalt metal on silicon photoanodes. *Energy & Environmental Science* **2011**, *4*, 2058–2061.
- [27] Luo, J.; Im, J.-H.; Mayer, M. T.; Schreier, M.; Nazeeruddin, M. K.; Park, N.-G.; Tilley, S. D.; Fan, H. J.; Gratzel, M. Water photolysis at 12.3 percent efficiency via perovskite photovoltaics and Earth-abundant catalysts. *Science* **2014**, *345*, 1593–1596.
- [28] Danko, D. B.; Sylenko, P. M.; Shlapak, A. M.; Khyzhun, O. Y.; Shcherbakova, L. G.; Ershova, O. G.; Solonin, Y. M. Photoelectrochemical cell for water decomposition with a hybrid photoanode and a metal-hydride cathode. *Solar Energy Materials and Solar Cells* **2013**, *114*, 172–178.
- [29] O'Regan, B.; Gratzel, M. A low-cost, high-efficiency solar cell based on dye-sensitized colloidal TiO₂ films. *Nature* **1991**, *353*, 737–740.
- [30] Faccio, R.; Fernandez-Werner, L.; Pardo, H.; Mombro, A. W. Current Trends in Materials for Dye Sensitized Solar Cells. *Recent Patents on Nanotechnology* **2011**, *5*, 46–61.
- [31] Anta, J. A.; Guillen, E.; Tena-Zaera, R. ZnO-Based Dye-Sensitized Solar Cells. *The Journal of Physical Chemistry C* **2012**, *116*, 11413–11425.

- [32] Bauer, C.; Boschloo, G.; Mukhtar, E.; Hagfeldt, A. Ultrafast studies of electron injection in Ru dye sensitized SnO₂ nanocrystalline thin film. *International Journal of Photoenergy* **2002**, *4*.
- [33] Guo, F.-a.; Li, G.; Zhang, W. Barium Stannate as Semiconductor Working Electrodes for Dye-Sensitized Solar Cells. *International Journal of Photoenergy* **2010**, *2010*, 7.
- [34] Burnside, S.; Moser, J.-E.; Brooks, K.; Grätzel, M.; Cahen, D. Nanocrystalline Mesoporous Strontium Titanate as Photoelectrode Material for Photosensitized Solar Devices: Increasing Photovoltage through Flatband Potential Engineering. *The Journal of Physical Chemistry B* **1999**, *103*, 9328–9332.
- [35] Sayama, K.; Sugihara, H.; Arakawa, H. Photoelectrochemical Properties of a Porous Nb₂O₅ Electrode Sensitized by a Ruthenium Dye. *Chemistry of Materials* **1998**, *10*, 3825–3832.
- [36] Nattestad, A.; Mozer, A. J.; Fischer, M. K. R.; Cheng, Y. B.; Mishra, A.; Bauerle, P.; Bach, U. Highly efficient photocathodes for dye-sensitized tandem solar cells. *Nat Mater* **2010**, *9*, 31–35.
- [37] Chapin, D. M.; Fuller, C. S.; Pearson, G. L. A New Silicon p-n Junction Photocell for Converting Solar Radiation into Electrical Power. *Journal of Applied Physics* **1954**, *25*, 676–677.
- [38] Brown, G. F.; Wu, J. Third generation photovoltaics. *Laser & Photonics Reviews* **2009**, *3*, 394–405.
- [39] Chung, I.; Lee, B.; He, J.; Chang, R. P. H.; Kanatzidis, M. G. All-solid-state dye-sensitized solar cells with high efficiency. *Nature* **2012**, *485*, 486–489.
- [40] Sakamoto, H.; Igarashi, S.; Uchida, M.; Niime, K.; Nagai, M. Highly efficient all solid state dye-sensitized solar cells by the specific interaction of CuI with NCS groups II. Enhancement of the photovoltaic characteristics. *Organic Electronics* **2012**, *13*, 514–518.
- [41] Hsu, C.-Y.; Chen, Y.-C.; Lin, R. Y.-Y.; Ho, K.-C.; Lin, J. T. Solid-state dye-sensitized solar cells based on spirofluorene (spiro-OMeTAD) and arylamines as hole transporting materials. *Physical Chemistry Chemical Physics* **2012**, *14*, 14099–14109.
- [42] Premalal, E. V. A.; Dematage, N.; Kumara, G. R. R. A.; Rajapakse, R. M. G.; Shimomura, M.; Murakami, K.; Konno, A. Preparation of structurally modified, conductivity enhanced-p-CuSCN and its application in dye-sensitized solid-state solar cells. *Journal of Power Sources* **2012**, *203*, 288–296.
- [43] Odobel, F.; Le Pleux, L.; Pellegrin, Y.; Blart, E. New Photovoltaic Devices Based on the Sensitization of p-type Semiconductors: Challenges and Opportunities. *Accounts of Chemical Research* **2010**, *43*, 1063–1071.
- [44] Bouclé, J.; Ackermann, J. Solid-state dye-sensitized and bulk heterojunction solar cells using TiO₂ and ZnO nanostructures: recent progress and new concepts at the borderline. *Polymer International* **2012**, *61*, 355–373.
- [45] Green, M. A.; Ho-Baillie, A.; Snaith, H. J. The emergence of perovskite solar cells. *Nat Photon* **2014**, *8*, 506–514.

- [46] Kojima, A.; Teshima, K.; Shirai, Y.; Miyasaka, T. Organometal Halide Perovskites as Visible-Light Sensitizers for Photovoltaic Cells. *Journal of the American Chemical Society* **2009**, *131*, 6050–6051.
- [47] Lee, M. M.; Teuscher, J.; Miyasaka, T.; Murakami, T. N.; Snaith, H. J. Efficient Hybrid Solar Cells Based on Meso-Superstructured Organometal Halide Perovskites. *Science* **2012**, *338*, 643–647.
- [48] Kim, H.-S.; Lee, C.-R.; Im, J.-H.; Lee, K.-B.; Moehl, T.; Marchioro, A.; Moon, S.-J.; Humphry-Baker, R.; Yum, J.-H.; Moser, J. E.; Grätzel, M.; Park, N.-G. Lead Iodide Perovskite Sensitized All-Solid-State Submicron Thin Film Mesoscopic Solar Cell with Efficiency Exceeding 9%. *Scientific Reports* **2012**, *2*, 591.
- [49] Yoong, L. S.; Chong, F. K.; Dutta, B. K. Development of copper-doped TiO₂ photocatalyst for hydrogen production under visible light. *Energy* **2009**, *34*, 1652–1661.
- [50] Dong, H.; Zeng, G.; Tang, L.; Fan, C.; Zhang, C.; He, X.; He, Y. An overview on limitations of TiO₂-based particles for photocatalytic degradation of organic pollutants and the corresponding countermeasures. *Water Research* **2015**, *79*, 128–146.
- [51] Ishihara, T., *Perovskite Oxide for Solid Oxide Fuel Cells*; Springer: Dordrecht Heidelberg London New York, 2009.
- [52] Singhal, S. C.; Kendall, K., *High Temperature Solid Oxide Fuel Cells: Fundamentals, Design and Applications*; Elsevier: 2003.
- [53] Maier, J., *Physical Chemistry of Ionic Materials: Ions and Electrons in Solids*; John Wiley and Sons, Ltd: 2004.
- [54] Tilly, R. J. D., *Defects in Solids*; John Wiley and Sons: 2008.
- [55] Holleman; Wiberg, *Lehrbuch der Anorganischen Chemie*, 102nd ed.; Walter de Gruyter: 2007.
- [56] Hanaor, D. A. H.; Sorrell, C. C. Review of the anatase to rutile phase transformation. *Journal of Materials Science* **2011**, *46*, 855–874.
- [57] Kofstad, P., *Nonstoichiometry, Diffusion, and Electrical Conductivity in Binary Metal Oxides*; Wiley-Interscience: New York, London, Sidney, Toronto, 1972.
- [58] http://www.alpina-farben.de/uploads/tx_enetalpina/TI_2010_Alpinaweiss_matt.pdf (accessed 19/11/2015).
- [59] <http://bmg.gv.at/cms/home/attachments/0/5/2/CH1403/CMS1391694002077/e-nummern.pdf> (accessed 19/11/2015).
- [60] Osterath, B. Wie Chemie vor Hautkrebs schützt. *Nachrichten aus der Chemie* **2015**, *63*, 894–898.
- [61] Riedel, E., *Anorganische Chemie*, 6th ed.; Walter de Gruyter: Berlin New York, 2004.
- [62] Nowotny, M. K.; Sheppard, L. R.; Bak, T.; Nowotny, J. Defect Chemistry of Titanium Dioxide. Application of Defect Engineering in Processing of TiO₂-Based Photocatalysts. *The Journal of Physical Chemistry C* **2008**, *112*, 5275–5300.
- [63] Bak, T.; Bogdanoff, P.; Fiechter, S.; Nowotny, J. Defect engineering of titanium dioxide: full defect disorder. *Advances in Applied Ceramics* **2012**, *111*, 62–71.

- [64] Bak, T.; Nowotny, J.; Nowotny, M. K. Defect Disorder of Titanium Dioxide. *The Journal of Physical Chemistry B* **2006**, *110*, 21560–21567.
- [65] Bak, T.; Nowotny, J.; Nowotny, M. K.; Sheppard, L. R. Defect engineering of titanium dioxide. *Journal of the Australian Ceramic Society* **2008**, *44*, 63–67.
- [66] Bak, T.; Nowotny, J.; Rekas, M.; Sorrell, C. C. Defect chemistry and semiconducting properties of titanium dioxide: I. Intrinsic electronic equilibrium. *Journal of Physics and Chemistry of Solids* **2003**, *64*, 1043–1056.
- [67] Bak, T.; Nowotny, J.; Rekas, M.; Sorrell, C. C. Defect chemistry and semiconducting properties of titanium dioxide: II. Defect diagrams. *Journal of Physics and Chemistry of Solids* **2003**, *64*, 1057–1067.
- [68] Bak, T.; Nowotny, J.; Rekas, M.; Sorrell, C. C. Defect chemistry and semiconducting properties of titanium dioxide: III. Mobility of electronic charge carriers. *Journal of Physics and Chemistry of Solids* **2003**, *64*, 1069–1087.
- [69] Bak, T.; Nowotny, M. K.; Sheppard, L. R.; Nowotny, J. Charge Transport in Cr-Doped Titanium Dioxide. *The Journal of Physical Chemistry C* **2008**, *112*, 7255–7262.
- [70] Nowotny, J.; Bak, T.; Nowotny, M. K.; Sheppard, L. R. Defect Chemistry and Electrical Properties of Titanium Dioxide. 1. Defect Diagrams. *The Journal of Physical Chemistry C* **2007**, *112*, 590–601.
- [71] Nowotny, J.; Li, W.; Bak, T. Effect of oxygen activity on semiconducting properties of TiO₂ (rutile). *Ionics* **2014**, 1–8.
- [72] Nowotny, M. K.; Bak, T.; Nowotny, J. Electrical Properties and Defect Chemistry of TiO₂ Single Crystal. I. Electrical Conductivity. *The Journal of Physical Chemistry B* **2006**, *110*, 16270–16282.
- [73] Nowotny, M. K.; Bak, T.; Nowotny, J. Electrical Properties and Defect Chemistry of TiO₂ Single Crystal. II. Thermoelectric Power. *The Journal of Physical Chemistry B* **2006**, *110*, 16283–16291.
- [74] Nowotny, M. K.; Bak, T.; Nowotny, J. Electrical Properties and Defect Chemistry of TiO₂ Single Crystal. III. Equilibration Kinetics and Chemical Diffusion. *The Journal of Physical Chemistry B* **2006**, *110*, 16292–16301.
- [75] Nowotny, M. K.; Bak, T.; Nowotny, J. Electrical Properties and Defect Chemistry of TiO₂ Single Crystal. IV. Prolonged Oxidation Kinetics and Chemical Diffusion. *The Journal of Physical Chemistry B* **2006**, *110*, 16302–16308.
- [76] Sheppard, L. R.; Bak, T.; Nowotny, J. Electrical Properties of Niobium-Doped Titanium Dioxide. 1. Defect Disorder. *The Journal of Physical Chemistry B* **2006**, *110*, 22447–22454.
- [77] Sheppard, L. R.; Nowotny, M. K.; Bak, T.; Nowotny, J. Effect of cooling on electrical conductivity of TiO₂. *physica status solidi (b)* **2008**, *245*, 1816–1827.
- [78] Nowotny, J.; Alim, M. A.; Bak, T.; Idris, M. A.; Ionescu, M.; Prince, K.; Sahdan, M. Z.; Sopian, K.; Mat Teridi, M. A.; Sigmund, W. Defect chemistry and defect engineering of TiO₂-based semiconductors for solar energy conversion. *Chemical Society Reviews* **2015**, *44*, 8424–8442.

- [79] Kofstad, P. Note on the defect structure of rutile (TiO_2). *Journal of the Less Common Metals* **1967**, *13*, 635–638.
- [80] In *CRC Handbook of Chemistry and Physics, 90th edition (CD-ROM Version 2010)*, Lide, D. R., Ed., 90th; CRC Press/Taylor and Francis: Boca Raton, FL.
- [81] http://www.nist.gov/pml/data/images/illo_for_2014_PT_1.PNG (accessed 29/12/2015).
- [82] <http://physics.nist.gov/cgi-bin/cuu/Value?na> (accessed 04/02/2016).
- [83] http://physics.nist.gov/cgi-bin/cuu/Value?e%7Csearch_for=elementary+charge (accessed 29/12/2015).
- [84] http://physics.nist.gov/cgi-bin/cuu/Value?tkev%7Csearch_for=Boltzmann (accessed 10/02/2016).
- [85] Lee, D. K.; Yoo, H. I. Unusual oxygen re-equilibration kinetics of $\text{TiO}_{2-\delta}$. *Solid State Ionics* **2006**, *177*, 1–9.
- [86] Knauth, P.; Tuller, H. L. Electrical and defect thermodynamic properties of nanocrystalline titanium dioxide. *Journal of Applied Physics* **1999**, *85*, 897–902.
- [87] Weibel, A.; Bouchet, R.; Knauth, P. Electrical properties and defect chemistry of anatase (TiO_2). *Solid State Ionics* **2006**, *177*, 229–236.
- [88] De Souza, R. A.; Fleig, J.; Merkle, R.; Maier, J. SrTiO_3 : A Model Electroceramic. *Zeitschrift für Metallkunde* **2003**, *94*, 218–225.
- [89] Merkle, R.; Maier, J. How Is Oxygen Incorporated into Oxides? A Comprehensive Kinetic Study of a Simple Solid-State Reaction with SrTiO_3 as a Model Material. *Angewandte Chemie International Edition* **2008**, *47*, 3874–3894.
- [90] Jung, W.; Tuller, H. L. A New Model Describing Solid Oxide Fuel Cell Cathode Kinetics: Model Thin Film $\text{SrTi}_{1-x}\text{Fe}_x\text{O}_{3-\delta}$ Mixed Conducting Oxides—a Case Study. *Advanced Energy Materials* **2011**, *1*, 1184–1191.
- [91] Verbraeken, M. C.; Ramos, T.; Agersted, K.; Ma, Q.; Savaniu, C. D.; Sudireddy, B. R.; Irvine, J. T. S.; Holtappels, P.; Tietz, F. Modified strontium titanates: from defect chemistry to SOFC anodes. *RSC Advances* **2015**, *5*, 1168–1180.
- [92] Denk, I.; Münch, W.; Maier, J. Partial Conductivities in SrTiO_3 : Bulk Polarization Experiments, Oxygen Concentration Cell Measurements, and Defect-Chemical Modeling. *Journal of the American Ceramic Society* **1995**, *78*, 3265–3272.
- [93] Bieger, T.; Maier, J. An Optical In-Situ Method to Study Redox-Kinetics in SrTiO_3 . *Berichte der Bunsengesellschaft für physikalische Chemie* **1993**, *97*, 1098–1104.
- [94] Gundlach, H.-W. Kinetik der Phasengrenzreaktionen zwischen Sauerstoff und anodisch erzeugtem Titandioxid variabler Stöchiometrie., PhD thesis, Technische Universität Clausthal, 1978.
- [95] Gundlach, H. W.; Heusler, K. E. Kinetics of the Incorporation of Oxygen into Non-Stoichiometric Titanium Dioxide Films. *Zeitschrift für Physikalische Chemie* **1980**, *119*, 213–224.
- [96] Merkle, R.; De Souza, R. A.; Maier, J. Optically Tuning the Rate of Stoichiometry Changes: Surface-Controlled Oxygen Incorporation into Oxides under UV Irradiation. *Angewandte Chemie International Edition* **2001**, *40*, 2126–2129.

- [97] Ye, X.; Melas-Kyriazi, J.; Feng, Z. A.; Melosh, N. A.; Chueh, W. C. A semiconductor/mixed ion and electron conductor heterojunction for elevated-temperature water splitting. *Physical Chemistry Chemical Physics* **2013**, *15*, 15459–15469.
- [98] Navickas, E.; Gerstl, M.; Friedbacher, G.; Kubel, F.; Fleig, J. Measurement of the across-plane conductivity of YSZ thin films on silicon. *Solid State Ionics* **2012**, *211*, 58–64.
- [99] Huber, S. Mass and charge transport properties of Fe-doped SrTiO₃ thin films and their dependence on DC voltage., PhD thesis, Vienna University of Technology, 2014, <http://www.ub.tuwien.ac.at/diss/AC11756663.pdf> (accessed 14/09/2015).
- [100] Chowdhury, P.; Barshilia, H. C.; Selvakumar, N.; Deepthi, B.; Rajam, K. S.; Chaudhuri, A. R.; Krupanidhi, S. B. The structural and electrical properties of TiO₂ thin films prepared by thermal oxidation. *Physica B: Condensed Matter* **2008**, *403*, 3718–3723.
- [101] Lin, Z. A.; Lu, W. C.; Wu, C. Y.; Chang, K. S. Facile fabrication and tuning of TiO₂ nanoarchitected morphology using magnetron sputtering and its applications to photocatalysis. *Ceramics International* **2014**, *40*, 15523–15529.
- [102] Wang, Z.; Yao, N.; Hu, X.; Shi, X. Structural and photocatalytic study of titanium dioxide films deposited by DC sputtering. *Materials Science in Semiconductor Processing* **2014**, *21*, 91–97.
- [103] Mukherjee, S. K.; Nebatti, A.; Mohtascham, F.; Schipporeit, S.; Notthoff, C.; Mergel, D. Influence of thickness on the structural properties of radio-frequency and direct-current magnetron sputtered TiO₂ anatase thin films. *Thin Solid Films* **2014**, *558*, 443–448.
- [104] Zheng, J.; Bao, S.; Guo, Y.; Jin, P. TiO₂ films prepared by DC reactive magnetron sputtering at room temperature: Phase control and photocatalytic properties. *Surface and Coatings Technology* **2014**, *240*, 293–300.
- [105] Sarma, B. K.; Pal, A. R.; Bailung, H.; Chutia, J. Effect of post-deposition annealing on the growth of nanocrystalline TiO₂ thin films and elastic anisotropy of rutile phase at different temperatures. *Journal of Alloys and Compounds* **2013**, *577*, 261–268.
- [106] Ting, C.-C.; Chen, S.-Y.; Liu, D.-M. Structural evolution and optical properties of TiO₂ thin films prepared by thermal oxidation of sputtered Ti films. *Journal of Applied Physics* **2000**, *88*, 4628–4633.
- [107] López-Huerta, F.; Cervantes, B.; González, O.; Hernández-Torres, J.; García-González, L.; Vega, R.; Herrera-May, A.; Soto, E. Biocompatibility and Surface Properties of TiO₂ Thin Films Deposited by DC Magnetron Sputtering. *Materials* **2014**, *7*, 4105–4117.
- [108] http://www.vonardenne.biz/VON_ARDENNE/ProdukteMaerkte/RD-and-Pilot-Systems/Vertical-Inline/VISS300S-Sputter-System-for-TCO.html (accessed 17/09/2015).
- [109] NIST Atomic Spectra Database., http://physics.nist.gov/PhysRefData/ASD/lines_form.html (accessed 18/09/2015).

- [110] <http://www.astro.sunysb.edu/fwalter/AST341/qn.html> (accessed 18/09/2015).
- [111] Escobar-Alarcón, L.; Haro-Poniatowski, E.; Camacho-López, M. A.; Fernández-Guasti, M.; Jiménez-Jarquín, J.; Sánchez-Pineda, A. Structural characterization of TiO₂ thin films obtained by pulsed laser deposition. *Applied Surface Science* **1999**, *137*, 38–44.
- [112] Syarif, D. G.; Miyashita, A.; Yamaki, T.; Sumita, T.; Choi, Y.; Itoh, H. Preparation of anatase and rutile thin films by controlling oxygen partial pressure. *Applied Surface Science* **2002**, *193*, 287–292.
- [113] Liu, X.; Yin, J.; Liu, Z. G.; Yin, X. B.; Chen, G. X.; Wang, M. Structural characterization of TiO₂ thin films prepared by pulsed laser deposition on GaAs substrates. *Applied Surface Science* **2001**, *174*, 35–39.
- [114] Rupp, G. M.; Tellez, H.; Druce, J.; Limbeck, A.; Ishihara, T.; Kilner, J.; Fleig, J. Surface chemistry of La_{0.6}Sr_{0.4}CoO_{3-δ} thin films and its impact on the oxygen surface exchange resistance. *Journal of Materials Chemistry A* **2015**, *3*, 22759–22769.
- [115] Carpentier, J.-L.; Lebrun, A.; Perdu, F. Point defects and charge transport in pure and chromium-doped rutile at 1273 K. *Journal of Physics and Chemistry of Solids* **1989**, *50*, 145–151.
- [116] Kato, H.; Kudo, A. Visible-Light-Response and Photocatalytic Activities of TiO₂ and SrTiO₃ Photocatalysts Codoped with Antimony and Chromium. *The Journal of Physical Chemistry B* **2002**, *106*, 5029–5034.
- [117] Ikeda, T.; Nomoto, T.; Eda, K.; Mizutani, Y.; Kato, H.; Kudo, A.; Onishi, H. Photoinduced Dynamics of TiO₂ Doped with Cr and Sb. *The Journal of Physical Chemistry C* **2008**, *112*, 1167–1173.
- [118] Wang, Y.; Shao, X.; Wang, B. Preparation, Characterization and Photocatalytic Activity of Cr-Doped Rutile TiO₂ (110) Single Crystal Thin Films. *Acta Phys. Chim. Sin.* **2013**, *29*, 1363–1369.
- [119] Moraes, V. Herstellung und Charakterisierung von La_xSr_{1-x}CoO_{3-δ}-Kathoden für Festoxidbrennstoffzellen., Bachelor's Thesis, Technische Universität Wien, 2012.
- [120] Hutterer, A. Herstellung und Charakterisierung von (La,Sr)(Co,Fe)O_{3-δ}-Kathoden für Festoxidbrennstoffzellen., Bachelor's Thesis, Technische Universität Wien, 2012.
- [121] Huber, T. Konstruktion einer Vakuum-Mikrokontaktapparatur und Impedanzmessungen an mikrostrukturierten Platin- und Nickelelektroden auf Yttrium stabilisiertem Zirconiumoxid in Wasserstoff Atmosphäre., Diploma Thesis, Vienna University of Technology, 2010, <http://www.ub.tuwien.ac.at/dipl/2010/AC07809690.pdf> (accessed 14/10/2015).
- [122] Rotter, B., PhD thesis in preparation, Vienna University of Technology, 2016.
- [123] Atkins, P.; Paula, J. d., *Physical Chemistry*; Oxford University Press: Great Britain, 2006; Vol. 8.
- [124] Giannakopoulou, T.; Todorova, N.; Giannouri, M.; Yu, J.; Trapalis, C. Optical and photocatalytic properties of composite TiO₂/ZnO thin films. *Catalysis Today* **2014**, *230*, 174–180.

- [125] Asiah, M. N.; Achoi, M. F.; Abdullah, S.; Rusop, M. Titanium Dioxide Thin Films: Effect of Annealed in Oxygen Ambient. *Advanced Materials Research* **2011**, *364*, 12–15.
- [126] Sorar, I.; Pehlivan, E.; Niklasson, G. A.; Granqvist, C. G. Electrochromism of DC magnetron-sputtered TiO₂: Role of film thickness. *Applied Surface Science* **2014**, *318*, 24–27.
- [127] Zhou, B.; Jiang, X.; liu, Z.; Shen, R.; Rogachev, A. V. Preparation and characterization of TiO₂ thin film by thermal oxidation of sputtered Ti film. *Materials Science in Semiconductor Processing* **2013**, *16*, 513–519.
- [128] Martin, N.; Rousselot, C.; Rondot, D.; Palmino, F.; Mercier, R. Microstructure modification of amorphous titanium oxide thin films during annealing treatment. *Thin Solid Films* **1997**, *300*, 113–121.
- [129] <http://www.ledengin.com/files/products/LZ4/LZ4-00U600.pdf> (accessed 06/02/2015).
- [130] Brunauer, G. C.; Rotter, B.; Walch, G.; Esmaili, E.; Opitz, A. K.; Ponweiser, K.; Summhammer, J.; Fleig, J. UV-Light-Driven Oxygen Pumping in a High-Temperature Solid Oxide Photoelectrochemical Cell. *Advanced Functional Materials* **2016**, *26*, 120–128.
- [131] Rothschild, A.; Komem, Y.; Cosandey, F. Low Temperature Reoxidation Mechanism in Nanocrystalline TiO_{2-δ} Thin Films. *Journal of The Electrochemical Society* **2001**, *148*, H85–H89.
- [132] Rothschild, A.; Edelman, F.; Komem, Y.; Cosandey, F. Sensing behavior of TiO₂ thin films exposed to air at low temperatures. *Sensors and Actuators B: Chemical* **2000**, *67*, 282–289.
- [133] Rothschild, A.; Komem, Y.; Cosandey, F. The Impact of Grain Boundary Diffusion on the Low Temperature Reoxidation Mechanism in Nanocrystalline TiO_{2-δ} Films. *Interface Science* **2001**, *9*, 157–162.
- [134] Opitz, A. K.; Lutz, A.; Kubicek, M.; Kubel, F.; Hutter, H.; Fleig, J. Investigation of the oxygen exchange mechanism on Pt—yttria stabilized zirconia at intermediate temperatures: Surface path versus bulk path. *Electrochimica Acta* **2011**, *56*, 9727–9740.
- [135] Lemmon, E. W. In *CRC Handbook of Chemistry and Physics*, 92nd ed., 2011–2012.
- [136] <http://webbook.nist.gov/cgi/cbook.cgi?ID=C1333740&Mask=1#Thermo-Gas> (accessed 11/01/2016).
- [137] <http://webbook.nist.gov/cgi/cbook.cgi?ID=C7782447&Mask=1#Thermo-Gas> (accessed 11/01/2016).
- [138] <http://webbook.nist.gov/cgi/cbook.cgi?ID=C7732185&Mask=1#Thermo-Gas> (accessed 11/01/2016).
- [139] Schlüter, H. J.; Barsoum, M.; Maier, J. Kinetic studies of oxygen incorporation in SrTiO₃ by permeation experiments. *Solid State Ionics* **1997**, *101–103, Part 1*, 509–515.
- [140] Baumann, F. S.; Fleig, J.; Habermeier, H.-U.; Maier, J. Impedance spectroscopic study on well-defined (La,Sr)(Co,Fe)O_{3-δ} model electrodes. *Solid State Ionics* **2006**, *177*, 1071–1081.

- [141] Brichzin, V.; Fleig, J.; Habermeier, H. U.; Cristiani, G.; Maier, J. The geometry dependence of the polarization resistance of Sr-doped LaMnO₃ microelectrodes on yttria-stabilized zirconia. *Solid State Ionics* **2002**, *152-153*, 499–507.
- [142] Holm, R., *Electric Contacts Handbook*, 3rd ed.; Springer-Verlag: Berlin, Göttingen, Heidelberg, 1958.
- [143] Ahamer, C. Auswirkung der Mikrostruktur von Yttrium-stabilisiertem Zirkoniumoxid auf dessen Leitfähigkeit., Diploma Thesis, Technische Universität Wien, 2012, <http://www.ub.tuwien.ac.at/dipl/2012/AC07813690.pdf>.
- [144] Opitz, A. K.; Fleig, J. Investigation of O₂ reduction on Pt/YSZ by means of thin film microelectrodes: The geometry dependence of the electrode impedance. *Solid State Ionics* **2010**, *181*, 684–693.
- [145] Fleig, J.; Baumann, F. S.; Brichzin, V.; Kim, H. R.; Jamnik, J.; Cristiani, G.; Habermeier, H. U.; Maier, J. Thin Film Microelectrodes in SOFC Electrode Research. *Fuel Cells* **2006**, *6*, 284–292.
- [146] Nielsen, J.; Jacobsen, T. Three-phase-boundary dynamics at Pt/YSZ microelectrodes. *Solid State Ionics* **2007**, *178*, 1001–1009.
- [147] Mutoro, E.; Günther, S.; Luerßen, B.; Valov, I.; Janek, J. Electrode activation and degradation: Morphology changes of platinum electrodes on YSZ during electrochemical polarisation. *Solid State Ionics* **2008**, *179*, 1835–1848.
- [148] Fleig, J. The grain boundary impedance of random microstructures: numerical simulations and implications for the analysis of experimental data. *Solid State Ionics* **2002**, *150*, 181–193.
- [149] Frederikse, H. P. R. In *CRC Handbook of Chemistry and Physics, 90th Edition (CD-ROM Version 2010)*, Lide, D. R., Ed.; CRC Press/Taylor and Francis: Boca Raton, 2010.
- [150] Dygas, J. R.; Fafilek, G.; Breiter, M. W. Simulation of beta"-alumina impedance spectra by equivalent circuits. *Key Engineering Materials* **1991**, *59-60*, 257–272.
- [151] <http://www.doitpoms.ac.uk/tlplib/dielectrics/temperature.php> (accessed 16/01/2016).
- [152] Jamnik, J.; Maier, J. Treatment of the Impedance of Mixed Conductors Equivalent Circuit Model and Explicit Approximate Solutions. *Journal of The Electrochemical Society* **1999**, *146*, 4183–4188.
- [153] Huber, T. M.; Opitz, A. K.; Kubicek, M.; Hutter, H.; Fleig, J. Temperature gradients in microelectrode measurements: Relevance and solutions for studies of SOFC electrode materials. *Solid State Ionics* **2014**, *268, Part A*, 82–93.
- [154] Yoo, H.-I.; Hwang, J.-H. Thermoelectric behavior of single crystalline ZrO₂(+8mo Y₂O₃). *Journal of Physics and Chemistry of Solids* **1992**, *53*, 973–981.
- [155] Nowotny, J.; Radecka, M.; Rekas, M. Semiconducting properties of undoped TiO₂. *Journal of Physics and Chemistry of Solids* **1997**, *58*, 927–937.
- [156] Wagner, M., <http://www.iue.tuwien.ac.at/phd/mwagner/node76.html> (accessed 10/02/2016).
- [157] Gerstl, M. Grain Boundaries and Interfaces in Thin Films of Yttria Stabilized Zirconia (YSZ)., Ph.D. Thesis, Technische Universität Wien, 2012.

[158] Sze, S. M., *Physics of Semiconductor Devices*; Wiley-Interscience: 1969.

Gregor Walch

Ernst-Melchior-Gasse 11/2/7

1020 Vienna, Austria

Education

since 02/2013

Doctoral Studies in Technical Chemistry

TU Wien, Vienna, Austria

Solid state electrochemistry and electroceramics lab

Dissertation: "Effect of light on mixed conducting electrodes in high-temperature solid oxide electrochemical cells"

Supervisor: Prof. Jürgen Fleig

Graduation expected in 05/2016

10/2009 – 02/2013

Master of Science in Chemistry

University of Vienna, Austria

- Focus on materials chemistry, electrochemistry as well as food and analytical chemistry

- Master's thesis: "High temperature electrolysis on model-type $\text{La}_{0.6}\text{Sr}_{0.4}\text{FeO}_{3-\delta}$ thin film electrodes"

Supervisor: Prof. Jürgen Fleig, TU Wien

Graduation with distinction

09/2011 – 02/2012

Semester abroad (Erasmus)

Université de Provence, Marseille, France

10/2005 – 10/2009

Bachelor of Science in Chemistry

University of Vienna, Austria

09/1996 – 06/2004

Secondary school

Gymnasium GRG 21 Ödenburger Straße, Vienna, Austria

Focus on languages

Graduation with distinction

Work Experience

11/2010 – 07/2011	Tour guide ebswien sewage treatment plant, Vienna
10/2004 – 09/2005	Paramedic Civil service at Arbeiter-Samariter-Bund and Grünes Kreuz, Vienna
07/2002	Intern Fujifilm photo lab, Vienna

Language Skills

German:	Mother tongue
English:	Level C1, Certificate in Advanced English (June 2003)
French:	Level B2
Italian:	Level A2

Computer Skills

Microsoft Office:	Word, Excel, PowerPoint
Other:	LaTeX, plots with Origin, simple calculations with Maple

Leisure Interests

Playing the electric bass, at the moment in a trio (voc/sax/b)
Climbing
Mountain biking

Publications

Journal papers

Walch, G., Opitz, A., Kogler, S. & Fleig, J. Correlation between hydrogen production rate, current, and electrode overpotential in a solid oxide electrolysis cell with $\text{La}_{0.6}\text{Sr}_{0.4}\text{FeO}_{3-\delta}$ thin-film cathode. *Monatsh. Chem.* **145**, 1055-1061 (2014).

Brunauer, G. C., Rotter, B., Walch, G., Esmaili, E., Opitz, A. K., Ponweiser, K., Summhammer, J. & Fleig, J. UV-Light-Driven Oxygen Pumping in a High-Temperature Solid Oxide Photoelectrochemical Cell. *Adv. Funct. Mater.* **26**, 120-128 (2016).

Poster

Walch, G., Rotter, B., Brunauer, G., Esmaili, E., Opitz, A., Summhammer, J., Ponweiser, K., Fleig, J. "Light-induced stoichiometry changes in oxides at high temperatures"
Poster: 15th European Conference on Solid State Chemistry, Wien, 23.-26.08.2015